공학박사 학위논문

Physicochemical Improvement of Nickel-Alumina Catalysts for Hydrogen Production by Steam Reforming of Liquefied Natural Gas (LNG)

액화천연가스(LNG)의 수증기 개질 반응에 의한 수소 생산용 니켈-알루미나 촉매의 물리화학적 개선

2015년 2월

서울대학교 대학원

화학생물공학부

방 용 주

Abstract

Physicochemical Improvement of Nickel-Alumina Catalysts for Hydrogen Production by Steam Reforming of Liquefied Natural Gas (LNG)

Yongju Bang

School of Chemical and Biological Engineering

The Graduate School

Seoul National University

Hydrogen has attracted much attention as the most promising energy carrier because it is clean and does not emit any pollutants such as NO_x and SO_x during the combustion. High energy density of hydrogen is another advantage of hydrogen utilization. These characteristics of hydrogen lead to a development of several hydrogen-related products such as hydrogen vehicle, combustion engine, and fuel cell. Although splitting of water through photo-catalysis and electrolysis is known as an ultimate method for hydrogen production, low productivity and high cost make it unfavorable for commercial hydrogen production. Instead, several catalytic reforming processes for commercial hydrogen production from hydrocarbons have been

extensively investigated, including steam reforming, partial oxidation, auto-thermal reforming, and dry reforming. Among these reforming processes, steam reforming has been widely employed for hydrogen production due to its high economical advantage. Moreover, liquefied natural gas (LNG), which is abundant and mainly composed of methane, can be used as a primary source for hydrogen production by steam reforming reaction. As LNG pipelines are more widespread in the modern cities, therefore, LNG will become an important hydrogen source for fuel cell system equipped with fuel processing unit.

Nickel-based catalyst has been considered as the most feasible catalyst for steam reforming reactions due to its high intrinsic activity and low price. Conventional steam reforming reaction has been carried out at high reaction temperature (> 800 ^{o}C), high reaction pressure (> 20 bar), and high steam to carbon ratio (steam/carbon > 2) in order to achieve a maximum catalytic performance of nickel-based catalyst. However, such severe reaction conditions are not favorable for on-site hydrogen production due to safety problems. For this reason, developing an efficient steam reforming catalyst with high catalytic activity and durability at moderate reaction conditions is of great importance. It has been reported that well-developed mesoporous structure of nickel-alumina catalyst not only enhanced the dispersion of active nickel site on the alumina support, but also facilitated the heat/mass transfer over the catalyst, resulting in a high catalytic performance. Thus, mesoporous nickel-alumina catalysts have received much attention for improving both catalytic activity and stability in the reforming reactions.

In this work, in order to derive high hydrogen production efficiency in

the catalytic steam reforming of LNG, mesoporous nickel-alumina catalysts were physicochemically modified by various preparation methods, including epoxide-driven sol-gel method, supercritical CO_2 drying method, carbon-templating method, phosphorus addition, evaporation-induced self-assembly method, and chemical immobilization of nickel.

First of all, a mesoporous Ni-Al_2O_3 aerogel catalyst was prepared by a single-step epoxide-driven sol-gel method and a subsequent supercritical CO_2 drying method (NA-ES catalyst). For comparison, a mesoporous Ni-Al_2O_3 aerogel catalyst was also prepared by a single-step alkoxide-based sol-gel method and a subsequent supercritical CO_2 drying method (NA-AS catalyst). Nickel species were highly dispersed in alumina through the formation of nickel aluminate phase in both NA-ES and NA-AS catalysts. However, nickel species in the NA-ES catalyst exhibited high reducibility and high dispersion compared to those in the NA-AS catalyst. In the steam reforming of LNG, NA-ES catalyst exhibited better catalytic performance than NA-AS catalyst in terms of LNG conversion and hydrogen yield.

A series of mesoporous nickel-alumina xerogel catalysts (denoted as CNAX) were prepared by a single-step carbon-templating sol-gel method using different amount of carbon template (X). Textural properties of CNAX catalysts were improved with increasing the amount of carbon template. It was revealed that the interaction between nickel species and alumina in the CNAX catalysts became weakened with increasing the amount of carbon template. Crystallite size of metallic nickel in the reduced CNAX catalysts showed a volcano-shaped trend with respect to the amount of carbon template. In the steam reforming of LNG, CNAX (X = 0, 6, 12, and 18) catalysts

exhibited a stable catalytic performance during the reaction, while CNA24 catalyst showed a significant catalyst deactivation. Initial LNG conversion and initial hydrogen yield increased with decreasing crystallite size of metallic nickel of the catalysts.

A series of nickel catalysts supported on mesoporous phosphorus-modified alumina xerogel (Ni/XPA, X = P/Al molar ratio) were prepared by an epoxide-driven sol-gel method and a subsequent incipient impregnation method. Although the calcined Ni/XPA catalysts retained both nickel oxide phase and nickel aluminate phase, relative distribution of nickel species of the catalysts was different depending on P/Al molar ratio. Crystallite size of metallic nickel increased with increasing P/Al molar ratio in the reduced Ni/XPA catalysts. However, Ni/0.05PA catalyst showed the largest amount of strong hydrogen-binding sites and exhibited the largest amount of adsorbed methane in the H_2-TPD and CH_4-TPD measurements, respectively. Catalytic performance in the steam reforming of LNG over Ni/XPA catalysts showed a volcano-shaped trend with respect to P/Al molar ratio. This result was well correlated with the amount of adsorbed methane calculated from CH_4-TPD measurements.

A mesoporous nickel-phosphorus-alumina aerogel catalyst (NPAA) was prepared by a single-step epoxide-driven sol-gel method and a subsequent supercritical CO_2 drying method. For comparison, a mesoporous nickel-phosphorus-alumina xerogel catalyst (NPAX) was also prepared by a single-step epoxide-driven sol-gel method and a subsequent evaporative drying method. It was found that supercritical CO_2 drying method was effective for enhancing textural properties of NPAA catalyst. It was also observed that the

reduced NPAA catalyst exhibited high nickel dispersion and large amount of methane adsorption compared to the reduced NPAX catalyst. In the steam reforming of LNG, NPAA catalyst with high affinity toward methane showed a better catalytic performance than NPAX catalyst.

An ordered mesoporous nickel-alumina catalyst (denoted as OMNA) was prepared by a single-step evaporation-induced self-assembly method. For comparison, a nickel catalyst supported on ordered mesoporous alumina support (denoted as Ni/OMA) was also prepared by an impregnation method. Although both Ni/OMA and OMNA catalysts retained unidimensionally ordered mesoporous structure, textural properties of the catalysts were significantly affected by the preparation method. Nickel species in the OMNA catalyst exhibited not only high reducibility but also strong resistance toward sintering during the reduction process, compared to those in the Ni/OMA catalyst. In the catalytic tests, OMNA catalyst with small crystallite size of metallic nickel exhibited higher LNG conversion and hydrogen yield than Ni/OMA catalyst. Furthermore, OMNA catalyst was more active in the steam reforming of LNG than non-ordered mesoporous nickel-alumina catalysts prepared by common surfactant-templating methods using cationic, anionic, and non-ionic surfactants.

Chemical immobilization of nickel was also attempted in order to increase nickel dispersion on alumina support. In conventional impregnation, nickel species are significantly aggregated on alumina support. However, nickel species can be finely dispersed on alumina support by chemical immobilization through Coulombic interaction between positively-charged alumina surface and $Ni(EDTA)^{2-}$ complex anion. The catalyst prepared by a

chemical immobilization method (NiE/Al) showed larger nickel dispersion and larger methane adsorption capacity than the catalyst prepared by a conventional impregnation method (Ni/Al). Accordingly, NiE/Al catalyst exhibited better catalytic performance in the steam reforming of LNG than Ni/Al catalyst.

In summary, various physicochemically-improved nickel-alumina catalysts were prepared and they were applied to the hydrogen production by steam reforming of LNG in this study. In order to explain catalytic performance of the prepared catalysts in the steam reforming of LNG, several characterizations such as N_2 adsorption-desorption, XRD, TPR, TEM, H_2-TPD, and CH_4-TPD analyses were carried out. It was concluded that nickel dispersion and reactant affinity of the catalysts played as an important factors determining the catalytic performance in the hydrogen production by steam reforming of LNG.

Keywords: Hydrogen production, Steam reforming of liquefied natural gas (LNG), Nickel catalyst, Epoxide-driven sol-gel method, Carbon-templating, Phosphorus, Xerogel, Aerogel, Evaporation-induced self-assembly, Chemical immobilization

Student Number: 2010-20994

Contents

List of Tables

List of Figures

Chapter 1. Introduction

1.1. Hydrogen production and utilization

Various sustainable and eco-friendly energies have been extensively investigated in order to overcome global environmental issues such as greenhouse gas emissions and air pollution [1-4]. Strong dependence of most industries on fossil fuels also makes it important for us to develop alternative future energies. Present energy supply methods based on oil industries are expected to lose their utility values due to oil limitation and high prices. Furthermore, rapid expansion of industries and economies caused a significant increase of global energy consumption in these days.

In this respect, future research development for renewable and alternative energy should meet the following issues [5]:

- To supply clean and abundant fuels to meet the increasing demands for liquid, gaseous fuels, and electricity (in terms of environment, safety, and availability)
- To increase the efficiency of energy use and electricity production (in terms of economic efficiency, energy conversion, and availability)
- To suppress pollutant emissions and decouple the link between energy utilization and greenhouse gas emissions (in terms of environment, health, and simplicity of process)

The above three issues have been seriously addressed and resolved by several means, such as wind, hydroelectric power, geothermal heat, solar light, nuclear power, vegetable oil, and hydrogen, and so on. Among the various form of energy utilization, hydrogen utilization has been spotlighted as the most promising and efficient energy supply routes. Hydrogen is abundantly available from various sources and has the highest energy content per unit of weight (> 140 kJ/g) than any other known fuels (Table 1.1) [6]. Besides, hydrogen is clean and renewable fuel, because it does not release NO_x, SO_x, and any carbonaceous compounds during the combustion process. It is also well known that hydrogen can be used as an important feedstock for several industrial fields including fuel processor, portable electric device, power plant, ammonia synthesis, and methanol synthesis (Fig. 1.1) [7,8]. Therefore, investigation and optimization of hydrogen production method for stable and efficient hydrogen supply have attracted much attention.

Globally, many countries are carrying various businesses and researches for hydrogen utilization. In Japan, which is one of the most developed countries in the fuel cell technologies, fuel cell development for home or vehicle uses have been extensively conducted and government investments are being focused on these areas. United States is also a major country for hydrogen energy investigations. According to the Department of Energy (DOE) of U.S., four-stage plans for achieving hydrogen economy by 2040 and roadmap of fuel cell commercialization were already established. Additionally, other countries such as Germany and Iceland, are also actively developing hydrogen-related industries and R&D businesses. In Korea, there have also been several research projects planned by government for hydrogen

production, hydrogen storage, hydrogen utilization, development of fuel cell, and development of catalytic system in fuel processor as listed in Table 1.2. Technological level of Korea in terms of hydrogen production efficiency is relatively low compared to that of other countries said above, however, although there are many research projects between academia and industries (competitiveness index for hydrogen production of Korea is about one-ninth of that for U.S.). Thus, extensive and competitive studies of various R&D fields are urgently required in order to commercialize hydrogen production processes and stimulate hydrogen utilizations.

Fuel cell research is the most important hydrogen-related area. Fuel cells generate electricity, water, and heat from reaction between hydrogen and oxygen (chemical energy). Among the distributed energy supply systems, fuel cells can exhibit the highest efficiency as listed in Table 1.3 [9]. Furthermore, they can be not only designed simply but also environmentally clean and noiseless. There are various types of fuel cells, including alkaline fuel cells (AFCs), phosphoric acid fuel cells (PAFCs), solid oxide fuel cells (SOFCs), molten carbonate fuel cells (MCFCs), direct methanol fuel cells (DMFCs), and proton exchange membrane fuel cells (PEMFCs), and so on [10]. PEMFCs are normally cheaper to manufacture and lightweight compact systems compared to other fuel cell types. Besides, they can be operated at relatively low temperature (50-100 ^{o}C) and provide high power density. These characteristics of PEMFCs are suitable for portable and distributed stationary electricity supply system. In this point of view, it can be said that fuel cell vehicles are top candidate of PEMFCs application. However, because hydrogen-rich stream with low CO concentration is required to operate

PEMFCs, fuel processing is necessary as a prerequisite to long-term and stable operation of them. Fuel processing is progressed by several steps, including reforming reaction of various feedstock (such as natural gas, naphtha, and alcohol), water-gas shift reaction (WGS), and preferential oxidation of CO (PROX) (Fig. 1.2) [11]. Reforming reaction can be either of steam reforming, partial oxidation, auto-thermal reforming, and dry reforming. In this reforming stage, it is very important to develop efficient catalytic reforming system for stable and abundant hydrogen production. Accordingly, many researches have been made on this reforming catalysis, especially on steam reforming of methane.

Table 1.1

Energy density and hydrogen to carbon ratio of various fuels

Fuel	Energy density (MJ/kg)	H/C ratio
Hydrogen	142.0	-
Natural gas	55.5	4.0
LPG	50.0	2.5-2.7
Methanol	22.5	4.0
Biogas (from gasifier)	4-14	0.7-2.0
Ethanol	29.7	3.0
Gasoline	45.8	1.6-2.1
Jet fuel	46.3	1.6-2.0
Diesel	45.3	1.8-2.3

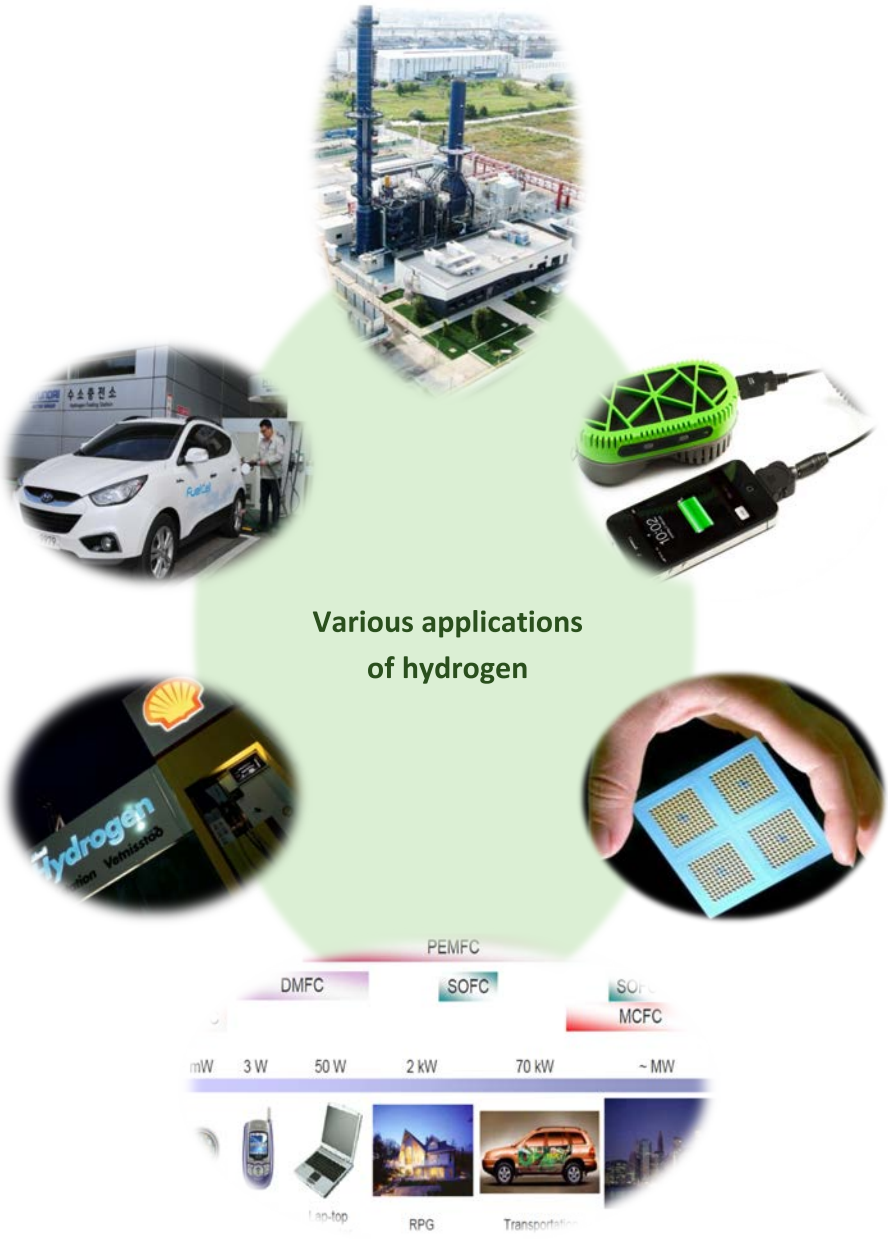

Fig. 1.1. Applications of hydrogen.

Table 1.2

Research projects on hydrogen energy utilization in Korea

Project	Department	Research period
21st century Frontier Project	Ministry of Science & Technology	2003~2013
Hydrogen & Fuel Cell Project	Ministry of Commerce Industry and Energy	2004~
IGCC Project	Ministry of Commerce Industry and Energy	2006~
Nuclear Hydrogen Demonstration Project	Ministry of Science & Technology	2004~2021

Table 1.3

Comparison of several power generating systems

	Capacity range	Efficiency (%)	Capital cost ($/kW)
Diesel engine	500 kW - 50 MW	35	200-350
Turbine generator	500 kW - 5 MW	29-42	450-870
Photovoltaic	1 kW - 1 MW	6-19	6600
Wind turbine	10 kW – 1 MW	25	1000
Fuel cell	200 kW - 2 MW	40-85	1500-3000

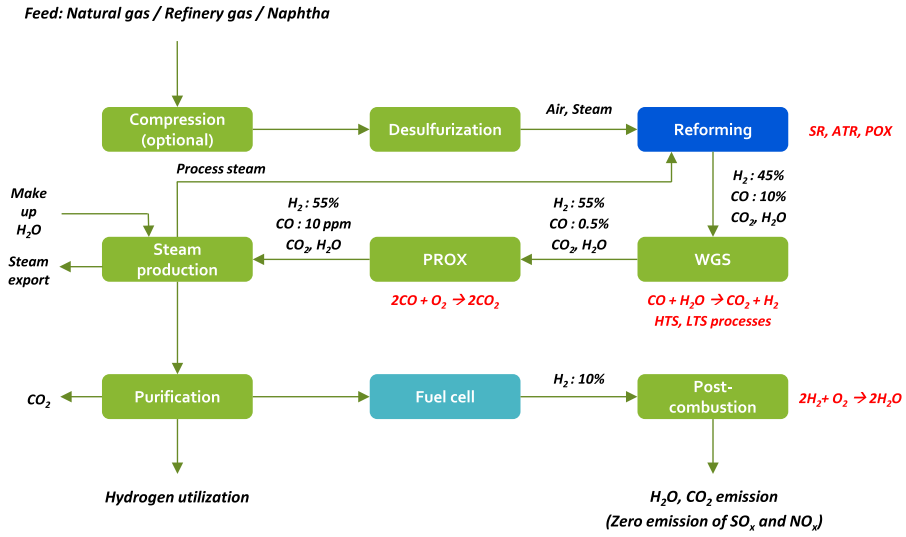

Fig. 1.2. Steps in fuel processing.

1.2. Steam reforming reaction

Hydrogen can be produced using various sources, including fossil fuels such as natural gas (methane), oil, and coal and renewable sources such as biomass and water with energy input from sunlight, wind, hydropower, and nuclear energy. Fossil fuels and biomass can be converted to hydrogen by several technologies such as reforming (hydrocarbons, oils, and alcohols), gasification, and pyrolysis (biomass and coal) [12]. In addition, water molecule, which is converted to hydrogen and oxygen by electrolysis and photo-catalysis, can be also ultimate future hydrogen source. However, except for reforming process, the other hydrogen production methods have been known to be unfavorable for commercialization because of their low economic efficiency until nowadays [13]. Among the reforming processes, in particular, catalytic steam reforming has been widely employed for commercial hydrogen production because of its high efficiency compared to other reforming processes including partial oxidation [14,15], auto-thermal reforming [16,17], and dry reforming [18,19]. Various hydrocarbons and their derivatives, such as methane [20,21], propane [22], butane [23], methanol [24], ethanol [25], acetic acid [26], and glycerol [27], have been utilized as reactants for steam reforming reaction. Liquefied natural gas (LNG), which is mainly composed of methane, is considered as a promising reactant due to its abundance and availability. LNG infrastructure in modern cities may become more widespread in the future, which will make LNG well suited as a hydrogen source for residential and on-board reformers in fuel cell

applications.

Various transition metal catalysts such as Rh [28], Pd [29], Ru [30], Co [31], and Ni [20] have been applied to the steam reforming of methane for hydrogen production. Among these transition metal catalysts, nickel-based catalysts have been widely used in the commercial steam reforming processes due to their high intrinsic activity and low cost [32,33]. Conventional steam reforming of methane (equation 1.1) has been carried out at high reaction temperature (> 800 ^{o}C), high reaction pressure (> 20 bar), and high steam to carbon ratio (steam/carbon > 2) in order to achieve a maximum catalytic performance of nickel-based catalyst [34-37]. In fact, several different reactions such as water-gas shift reaction (WGS; equation 1.2), reverse water-gas shift reaction (RWGS; reverse of equation 1.2), CO disproportionation (Boudouard reaction; equation 1.4), methane decomposition (equation 1.5) reactions are involved in the steam reforming reaction. The current industrial hydrogen production employs additional WGS reaction, preferential oxidation (PROX), and pressure swing adsorption (PSA) to yield high purity of hydrogen (> 99.99%).

$$CH_4 + H_2O \rightarrow CO + 3H_2 \qquad \Delta H^{o}_{298\ K} = +206\ kJ/mol \qquad (1.1)$$

$$CO + H_2O \leftrightarrow CO_2 + H_2 \qquad \Delta H^{o}_{298\ K} = -41\ kJ/mol \qquad (1.2)$$

$$CH_4 + H_2O \rightarrow CO + 3H_2 \qquad \Delta H^{o}_{298\ K} = +206\ kJ/mol \qquad (1.3)$$

$$2CO \rightarrow CO_2 + C \qquad \Delta H^{o}_{298\ K} = -172\ kJ/mol \qquad (1.4)$$

$$CH_4 \rightarrow C + 2H_2 \qquad \Delta H^{o}_{298\ K} = +75\ kJ/mol \qquad (1.5)$$

It is known that nickel-based catalysts are vulnerable to sintering and carbon deposition during the steam reforming reaction, resulting in a catalyst deactivation (Fig. 1.3) [36]. Furthermore, severe reaction conditions of steam reforming are not favorable for on-site hydrogen production due to safety problems. Therefore, developing an efficient nickel-based steam reforming catalyst with high catalytic activity and durability at moderate reaction conditions is of great importance.

Many attempts have been made to prepare highly active nickel-based catalyst with excellent durability during the steam reforming reaction as follows:

- A Ni/Al_2O_3-ZrO_2 xerogel catalyst prepared by a sol-gel method and a subsequent impregnation method was investigated for steam reforming of LNG [33]. Although the catalyst was proven to be highly stable toward catalyst deactivation for 1000 min-reaction, LNG conversion in the steam reforming reaction over the catalyst was only ca. 70%.
- Several nickel catalysts based on perovskite oxides have also attracted much attention due to their strong metal-support interaction and fine nickel dispersion [38,39].
- It was also found that Ni/SiO_2 catalyst prepared by an incipient wetness method showed a high coke resistance under water-deficient condition in the steam reforming of methane [40].
- Ni-Al_2O_3 aerogel catalyst prepared by a sol-gel method followed by a supercritical CO_2 drying was reported to exhibit an excellent catalytic

performance in the steam reforming of LNG [41]. However, there are many drawbacks in the supercritical CO_2 drying method such as difficulty in controlling drying condition and limitation for large-scale catalyst preparation.

- A nickel catalyst supported on γ-Al_2O_3 calcined under N_2O atmosphere is known to have high nickel surface area compared to that calcined under air atmosphere [42].
- Mesoporous alumina xerogel has been employed as a support for nickel catalyst in order to mitigate mass transfer limitation of reactants and to enhance nickel dispersion of the catalyst [43].
- Ceria support is also used for long-term stability of nickel catalyst in the steam reforming of methane due to its excellent redox property [44].
- It has also been reported that nickel-alumina catalyst prepared by a homogeneous precipitation method using surfactant was stable for long-term steam reforming reaction [45].
- Majewski et al. have reported that a nickel-silica catalyst with core-shell structure, which showed high coke resistance and stability, was effective for steam reforming of methane [46].
- A nickel catalyst supported on pyrochlore $Ce_2Zr_2O_x$ exhibited a stable catalytic activity in the steam reforming of methane due to the excellent oxygen storage capacity of $Ce_2Zr_2O_x$ solid solution [47].
- Addition of second metal such as Ca [48], Mo [49], and Mg [50] to the nickel-alumina catalyst has also been attempted to improve the catalytic activity and stability of nickel-based catalyst. When large amount of

second metal was added into nickel-based catalyst, however, decrease of catalytic reforming activity was inevitable due to the blocking of active sites [49,50].

- Addition of potassium and calcium into nickel-alumina catalyst was effective for enhancing gasification of surface carbon species [50].
- It has been reported that lanthanum effectively enhanced the physicochemical properties and catalytic performance of Ni-Al_2O_3 aerogel catalyst compared to other second metals [51].
- Furthermore, it has been reported that Ni-Mg-O catalyst shows higher activity and stability in the steam reforming of methane than a commercial reforming catalyst under reaction condition of low steam to carbon ratio [52].
- Synergistic effect of Mg and Cu addition into nickel catalyst was also investigated [53].
- Nickel catalyst supported on boron-containing alumina is known to be highly stable and active in the steam reforming reaction by preventing carbon deposition [54].
- Supported Ni-Fe alloy nanoparticles have also been employed to the steam reforming reaction, and they showed the enhanced catalytic performance and high resistance toward carbon deposition [55].

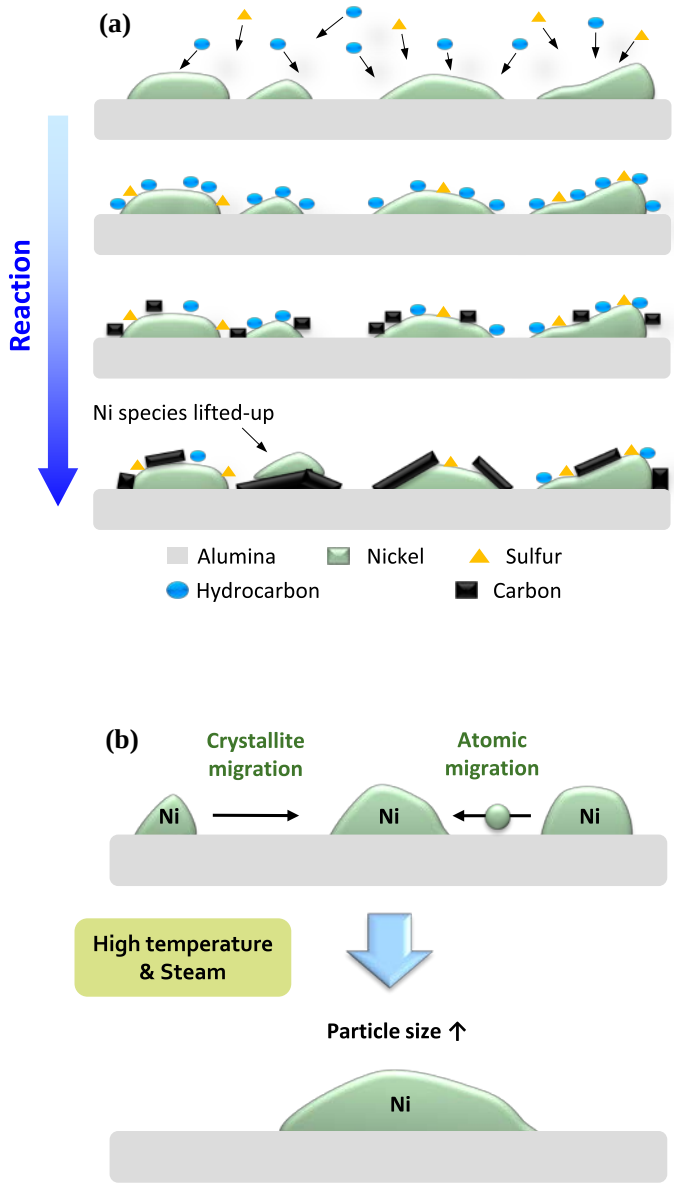

Fig. 1.3. Deactivation of nickel-based catalysts by (a) carbon deposition and (b) sintering.

1.3. Objective

Nickel-based reforming catalysts are vulnerable to catalyst deactivation due to carbon deposition and nickel sintering during the reaction. To tackle the catalyst deactivation problem and to enhance the catalytic activity of the nickel-based catalysts, various modifications of the catalysts such as second metal addition, sol-gel processing, hard/soft templating, supercritical drying, and non-metal promotion have been attempted. Nickel dispersion, textural property, and crystalline structure of the catalysts could be tuned by these methods, resulting in the enhanced catalytic performance of the nickel-based catalysts in the steam reforming reaction. It is known that nickel dispersion is a crucial factor determining overall reaction rate and hydrogen yield. Considering that steam reforming of methane occurs on the reduced nickel atom and the reaction is initiated by dissociative chemisorption step of methane (a rate-determining step), methane adsorption capacity of nickel catalyst is also important. It is widely accepted that well-developed mesoporous structure of Ni-Al_2O_3 catalyst not only facilitated the heat/mass transfer over the catalyst, but also enhanced the dispersion of active nickel site on the alumina support, resulting in a high catalytic performance [41,56,57]. In this work, therefore, modifications of mesoporous nickel-alumina catalysts have been attempted for improving both catalytic activity and stability in the steam reforming of LNG.

Traditionally, gel-based metal oxide materials have been prepared by an alkoxide-based sol-gel method using metal alkoxide precursors such as

aluminum tri-*sec*-butoxide [58]. However, these metal alkoxide precursors are expensive and difficult to handle due to their high reactivity and sensitivity to heat and moisture. To tackle these problems, a new versatile sol-gel synthesis route utilizing simple inorganic salt precursors and epoxide has been proposed with an aim of preparing mesoporous metal oxides such as iron oxide [59], alumina [60], and titania [61]. In this method, epoxide serves as an acid scavenger and gelation agent in the sol-gel polymerization process. Hydrated metal cations, which act as strong acid due to charge transfer from the coordinated water molecules, protonate oxygen atoms of epoxide molecules. Because this protonation step is very fast, many hydroxyl groups are rapidly generated on the metal cations. The resulting hydroxyl groups on the metal cations then induce polycondensation reaction through rapid formation of metal-O-metal bond. To our best knowledge, however, a mesoporous Ni-Al_2O_3 aerogel catalyst prepared by an epoxide-driven sol-gel method has never been employed for hydrogen production by steam reforming of LNG. Therefore, a systematic investigation on the application of mesoporous Ni-Al_2O_3 aerogel catalyst prepared by a single-step epoxide-driven sol-gel method to hydrogen production by steam reforming of LNG would be worthwhile.

It is known that various mesoporous metal oxides as a catalyst support can be prepared by a templating method [62-64]. In this method, template compounds, which affect the textural properties of metal oxides, are used as a structure-directing agent. In general, template compounds are classified into hard templates and soft templates by the phase of templates. Although soft templates are more advantageous for elaborate synthesis of mesoporous

structure, synthesis conditions such as reaction temperature and template concentration in solution should be strictly controlled. On the other hand, hard templates including silica and carbon materials are easy to use for the preparation of mesoporous materials due to their solidness and defined structure. In this point of view, preparation of mesoporous nickel-alumina xerogel catalysts using hard template for practical application to hydrogen production by steam reforming of LNG was carried out.

Only a few researches have focused on promotion of nickel-based catalysts via addition of non-metal elements such as boron, sulfur, and phosphorus [54,65,66]. Non-metal elements are useful for alleviation of carbon deposition on the surface of nickel-based catalyst in the steam reforming reaction, because these non-metal elements predominantly retain rich valence electrons and high electronegativity compared to metal elements. Moreover, this feature of non-metal elements may cause changes in textural and surface properties of nickel-based catalyst by forming a defective and asymmetrical electronic structure. It is expected that nickel dispersion, crystalline structure, and chemical affinity with reactant molecule of nickel-based catalyst can be modified by the addition of non-metal element. In particular, addition of phosphorus into alumina is known to be effective for stabilization of framework and modification of Lewis acid property of alumina [67]. For these reasons, a systematic investigation on the effect of phosphorus addition on the catalytic activity and physicochemical property of nickel-alumina catalyst was conducted. To further study phosphorus-modified nickel-alumina catalyst, nickel-phosphorus-alumina xerogel and aerogel catalysts were also prepared.

Various metal oxide supports with ordered mesoporous structure can be prepared by an evaporation-induced self-assembly (EISA) method using surfactants such as triblock copolymer [68-70]. In this method, self-assembled micelle structure is induced by increasing micelle concentration through evaporation of solvent. Unidimensionally ordered mesoporous supports are formed by removing cylindrical micelle assembly through thermal decomposition of micelle. According to the previous studies [71,72], these ordered mesoporous supports can effectively prevent aggregation of active metal particles by so-called confinement effect during high-temperature catalytic reaction. In other words, activity and stability of the catalyst can be improved by finely dispersing active metal throughout the supports. Therefore, developing an ordered mesoporous nickel-alumina catalyst for hydrogen production by steam reforming of LNG would be of great interest.

Generally, conventional impregnation method is unfavorable to disperse active component onto support. In order to increase dispersion of active component, chemical immobilization method has been studied. Chemical immobilization method involves charge generation on active metal species and support followed by immobilization due to Coulombic interaction. Different charge of active metal species and support attract each other, resulting in fine dispersion of active metal on support. To our best knowledge, however, no study has been conducted on nickel/alumina catalyst prepared by epoxide-driven sol-gel method and subsequent chemical immobilization method. Thus, design of nickel/alumina catalyst by chemical immobilization method for steam reforming of LNG would be worthwhile.

1.4. Outlook

As researches on catalyst development for hydrogen production by steam reforming of LNG progress, there would be some positive effects on technology, research, economy, and industrial fields as described below.

- First of all, the results from development of new reforming catalytic system are expected to be core foundations for manufacture of highly efficient fuel processor operated under low-temperature condition.
- Cost of fuel processor will decrease by the use of economic non-noble metal reforming catalyst, resulting in promotion of commercialization.
- Various preparation methods of porous catalysts can be applied to several research areas including electronics, IT, advanced materials, and biomass conversion, and so on.
- It is expected that hydrogen production efficiency will gradually increase, and accordingly, hydrogen production cost will decrease by ca. 20%.
- New hydrogen production process might not only decrease air pollution mainly caused by power generation but also heavily influence on energy saving.
- If new reforming technologies or catalytic systems are commercialized, it will be possible to establish national solutions towards rapid changes of global oil price as well as to strengthen national energy security by stable and consistent energy supply.

- Fuel cell, which is the most important and representative area of hydrogen utilization, can be applied to various fields such as vehicle, submarine, aircraft, and power generation. Thus, market size of reforming process can be readily expanded in the near future.
- Today, global market size is about 600 billion-won and it would be increased by 20% annually. According to this, basic research on reforming technologies can be an important factor determining foreign trade balance of Korea.
- After 2015, it is expected that fuel cell vehicles (FCVs) will exhibit high durability and convenience comparable to current gasoline or diesel engine vehicle. In this point of view, applications of the research results about reforming technologies are expected to be widespread with increasing supply and public interest for FCVs.

Chapter 2. Experimental

2.1. Preparation of catalysts

2.1.1. Preparation of mesoporous nickel-alumina aerogel catalyst by a single-step epoxide-driven sol-gel method

A mesoporous Ni-Al_2O_3 aerogel catalyst was prepared by a single-step epoxide-driven sol-gel method and a subsequent supercritical CO_2 drying method [60]. 8.6 g of aluminum precursor (aluminum nitrate nonahydrate, Sigma-Aldrich) and 2.4 g of nickel precursor (nickel nitrate hexahydrate, Sigma-Aldrich) were dissolved in ethanol (90 ml) with vigorous stirring for hydration of Al^{3+} and Ni^{2+} ions. Propylene oxide as a gelation agent was then added into the metal precursor solution to make hydroxyl group on the hydrated ions and to induce polycondensation reaction between Al^{3+} and Ni^{2+} ions. Molar ratio of aluminum precursor:nickel precursor:propylene oxide was fixed at 1:0.35:13.5. After maintaining the resulting solution for several minutes, a green opaque nickel-alumina composite gel was formed. The gel was aged for 2 days, and then it was dried at 50 ^oC and 120 atm for 18 h in a stream of supercritical CO_2. The resulting powder was then calcined at 700 ^oC for 5 h to yield a mesoporous Ni-Al_2O_3 aerogel catalyst. The Ni-Al_2O_3 aerogel catalyst prepared by a single-step epoxide-driven sol-gel method was denoted as NA-ES.

For comparison, a mesoporous Ni-Al_2O_3 aerogel catalyst was prepared by a single-step alkoxide-based sol-gel method and a subsequent supercritical CO_2 drying method, according to the similar method reported in literature [41]. 7.0 g of aluminum precursor (aluminum tri-sec-butoxide, Sigma-Aldrich) was dissolved in ethanol (60 ml) at 80 ^oC with vigorous stirring. Small amounts of distilled water and nitric acid, which had been diluted with ethanol, were slowly added into the solution of aluminum precursor for partial hydrolysis of aluminum precursor. After maintaining the resulting solution at 80 ^oC for a few minutes, a clear sol was obtained. The sol was cooled to 60 ^oC, and 2.4 g of nickel precursor (nickel acetate tetrahydrate, Sigma-Aldrich) was slowly added into the sol to obtain a nickel-alumina composite sol. After cooling the nickel-alumina composite sol to room temperature, a monolithic gel was obtained by adding an appropriate amount of water diluted with ethanol into the sol. The gel was aged for 2 days, and then it was dried at 50 ^oC and 120 atm for 18 h in a stream of supercritical CO_2. The resulting powder was finally calcined at 700 ^oC for 5 h to yield a mesoporous Ni-Al_2O_3 aerogel catalyst. The Ni-Al_2O_3 aerogel catalyst prepared by a single-step alkoxide-based sol-gel method was denoted as NA-AS. Nickel loading in the NA-ES and NA-AS catalysts was fixed at 40 wt%.

In addition, mesoporous alumina aerogel supports were prepared by an epoxide-driven sol-gel method and an alkoxide-based sol-gel method without using nickel precursor, according to the similar methods described above. The prepared mesoporous alumina aerogels prepared by an epoxide-driven sol-gel method and an alkoxide-based sol-gel method were denoted as A-ES and A-AS, respectively.

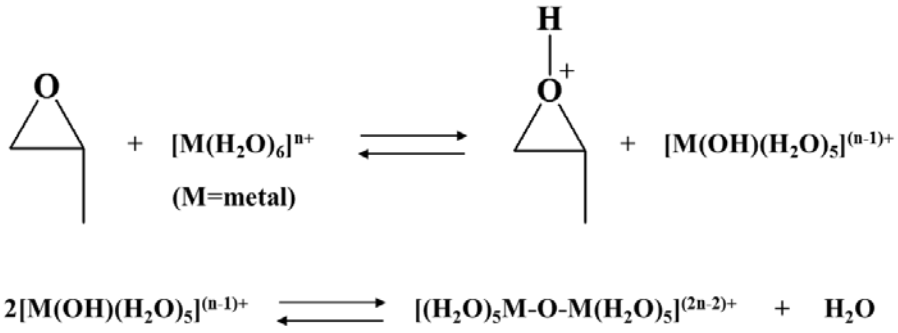

Fig. 2.1. Reactions involved in the preparation of metal oxide by an epoxide-driven sol-gel method.

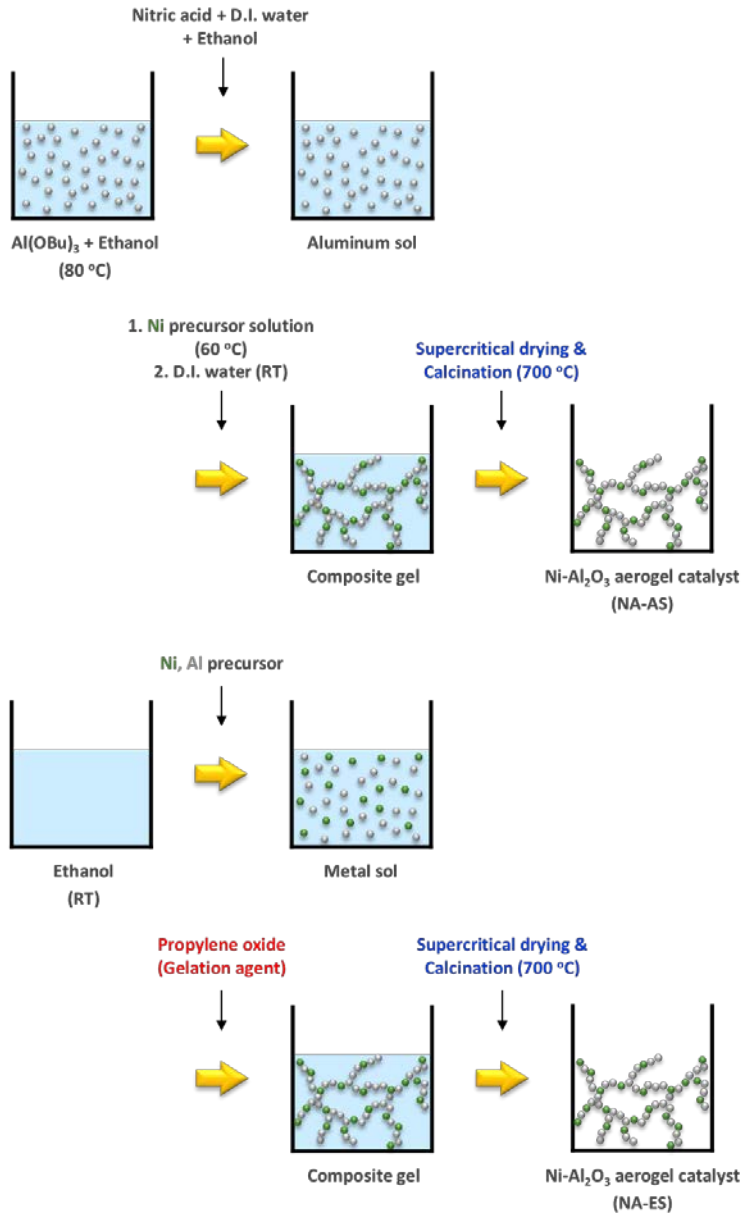

Fig. 2.2. Schematic procedures for the preparation of NA-AS by an alkoxide-based sol-gel method and NA-ES catalysts by an epoxide-driven sol-gel method.

2.1.2. Preparation of mesoporous nickel-alumina xerogel catalyst by a carbon-templating sol-gel method

A series of nickel-alumina xerogel catalysts were prepared by a single-step carbon-templating sol-gel method using different amount of carbon template, according to the similar method reported in the literatures [60,73]. 13.7 g of aluminum precursor (aluminum nitrate nonahydrate, Sigma-Aldrich) and 3.7 g of nickel precursor (nickel nitrate hexahydrate, Sigma-Aldrich) were dissolved in ethanol (80 ml) with vigorous stirring. Commercial carbon particle (Carbon Black Pearls 2000, Cabot Corp.) as a template was then added into the solution. The amount of carbon particle was adjusted to be 0, 6, 12, 18, and 24 mg/g-ethanol. For better dispersion of carbon particles, carbon-suspended solution was placed in sonicator for 20 min. This solution was additionally stirred for 10 min, and then 34.5 ml of propylene oxide (Acros Organics) was added into the solution for polycondensation reaction between Al^{3+} and Ni^{2+} ions. After maintaining the solution for several minutes, a black nickel-alumina composite gel was obtained. The gel was aged for 2 days, and then it was dried at 80 ^{o}C for 24 h in a convection oven. The resulting powder was finally calcined at 700 ^{o}C for 5 h to yield a mesoporous nickel-alumina xerogel catalyst. The prepared mesoporous nickel-alumina xerogel catalysts were denoted as CNAX (X = 0, 6, 12, 18, and 24), where X represented the amount of carbon template (mg) used per 1 g of ethanol solvent. For example, CNA12 means a nickel-alumina xerogel catalyst prepared using 12 mg of carbon template for 1 g of ethanol.

Table 2.1

Physical properties of commercial carbon template

Carbon Black Pearls 2000 (Cabot Corp.)	
BET surface area (m^2/g)	1500
Primary particle size (nm)	12
Bulk density (g/cm^3)	0.15

2.1.3. Preparation of nickel catalyst supported on mesoporous phosphorus-modified alumina xerogel

A series of mesoporous phosphorus-modified alumina xerogel supports were prepared by an epoxide-driven sol-gel method [59,60,74]. 16.1 g of aluminum precursor (aluminum nitrate nonahydrate, Sigma-Aldrich) was dissolved in anhydrous ethanol (100 ml) at room temperature with vigorous stirring for 30 min (Solution A). For sufficient hydration of aluminum species, a small amount of distilled water (2.3 ml) was added into the solution A (Solution B). Phosphoric acid (Sigma-Aldrich), which served as a structural modifier, was then introduced into the solution B (Solution C). During this process, P/Al molar ratio was adjusted to be 0, 0.02, 0.05, 0.10, and 0.20. After stirring the solution C for 20 min, propylene oxide as a gelation agent was added into the solution C to induce polycondensation between metal species. White opaque gel was obtained within 20 min after the addition of propylene oxide. The gel was aged for 2 days and it was dried in a convection oven for 2 days at 80 ^{o}C. The resulting powder was calcined at 700 ^{o}C for 5 h to yield a mesoporous phosphorus-modified alumina xerogel support. The prepared mesoporous phosphorus-modified alumina xerogel supports were denoted as XPA (X = 0, 0.02, 0.05, 0.10, and 0.20), where X represented the P/Al molar ratio.

A set of nickel catalysts supported on mesoporous phosphorus-modified alumina xerogel supports (XPA) were prepared by an incipient wetness impregnation method. Nickel precursor (nickel nitrate hexahydrate, Sigma-

Aldrich) was dissolved in anhydrous ethanol for 20 min. The nickel precursor solution was added dropwise to XPA support for impregnation. The supported nickel catalyst was dried at 80 ^{o}C overnight in a convection oven. As-prepared catalyst sample was finally calcined at 700 ^{o}C for 5 h to yield a nickel catalyst supported on mesoporous phosphorus-modified alumina xerogel. The prepared nickel catalysts were denoted as Ni/XPA (X = 0, 0.02, 0.05, 0.10, and 0.20). The Ni loading was fixed at 20 wt% in all the Ni/XPA catalysts.

2.1.4. Preparation of mesoporous nickel-phosphorus-alumina aerogel catalyst by a single-step epoxide-driven sol-gel method

A mesoporous nickel-phosphorus-alumina aerogel catalyst was prepared by a single-step epoxide-driven sol-gel method and a subsequent supercritical CO_2 drying method [59,60]. 10.0 g of aluminum precursor (aluminum nitrate nonahydrate, Sigma-Aldrich) and 1.4 g of nickel precursor (nickel nitrate hexahydrate, Sigma-Aldrich) were dissolved in ethanol (73 ml) with vigorous stirring (Solution A). Distilled water (1.7 ml) was introduced into the solution A for sufficient hydration of metal species (Solution B). 0.1 ml of phosphoric acid (Sigma-Aldrich) was then added into the solution B, where P/Al molar ratio was adjusted to be 0.05 (Solution C). Solution C was additionally stirred for 20 min, and 22 ml of propylene oxide (Acros Organics) was then added into the solution C for cross-linking of metal species (Solution D). After maintaining the solution D for a few minutes, a green opaque composite gel was obtained. The gel was aged for 2 days, and it was transferred to autoclave for supercritical CO_2 drying. Supercritical CO_2 drying was conducted at 50 ^oC and 100 atm for 4 h. The resulting aerogel powder was then calcined at 700 ^oC for 5 h to obtain a mesoporous nickel-phosphorus-alumina aerogel catalyst. The prepared catalyst was denoted as NPAA. For comparison, a mesoporous nickel-phosphorus-alumina xerogel catalyst (denoted as NPAX) was also prepared by the similar methods described above, except that it was dried by evaporative drying at 80 ^oC for 48 h in a convection oven instead of supercritical CO_2 drying.

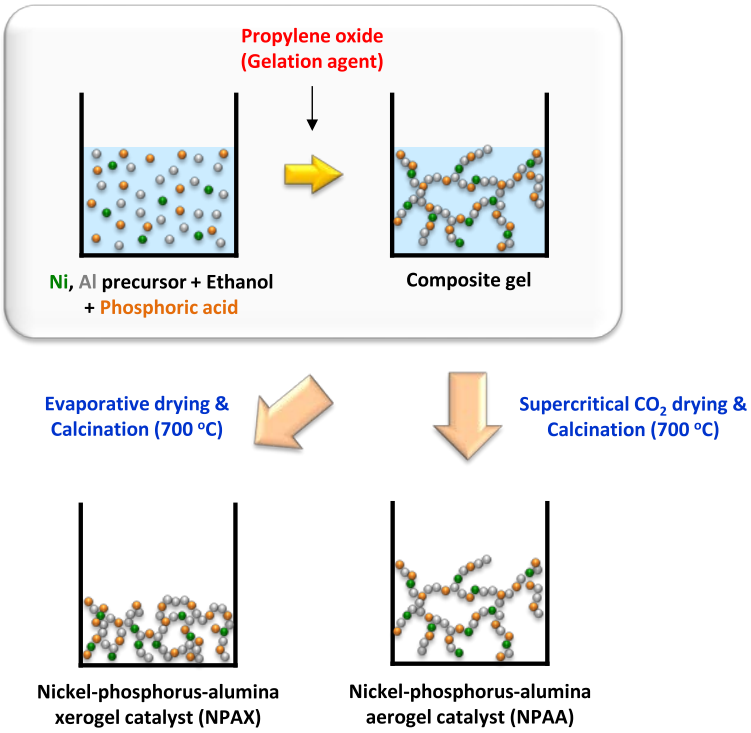

Fig. 2.3. Schematic procedures for the preparation of NPAX and NPAA catalysts.

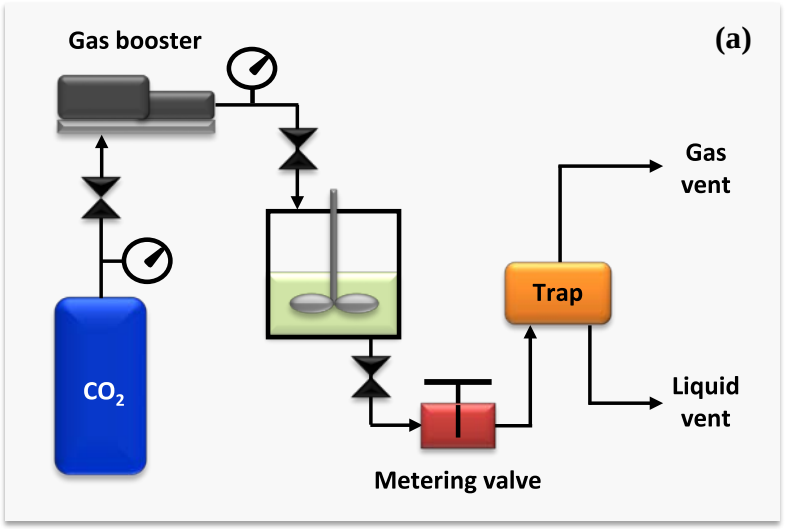

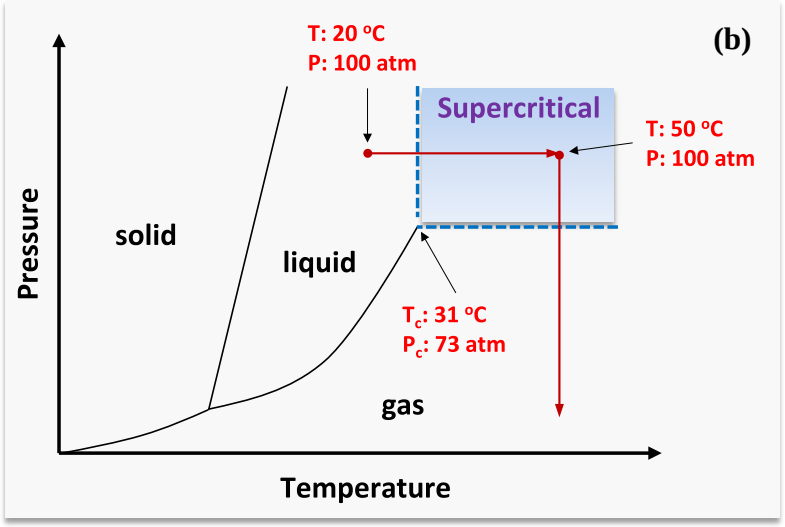

Fig. 2.4. (a) Supercritical CO_2 drying apparatus and (b) supercritical CO_2 drying process expressed on phase diagram.

2.1.5. Preparation of ordered mesoporous nickel-alumina catalyst by an evaporation-induced self-assembly method

An ordered mesoporous nickel-alumina catalyst was prepared by a single-step evaporation-induced self-assembly (EISA) method, according to the similar method reported in the literatures [62,75,76]. Fig. 2.5 shows the schematic procedures for the preparation of ordered mesoporous nickel-alumina catalyst. 2.3 g of $(EO)_{20}(PO)_{70}(EO)_{20}$ triblock copolymer (Pluronic P123, Sigma-Aldrich) was dissolved in anhydrous ethanol (50 ml) at room temperature with constant stirring for 4 h (Solution A). 4.3 g of aluminum precursor (aluminum isopropoxide, Sigma-Aldrich) and 1.1 g of nickel precursor (nickel nitrate hexahydrate, Sigma-Aldrich) were then added into the solution A (Solution B). 3.7 ml of nitric acid (69%) was then added to the solution B for complete homogenization and hydrolysis of metal precursors (Solution C). The solution C was stirred for 5 h, and then self-assembly of micelle structure was induced through solvent evaporation at 60 ^{o}C for 48 h without stirring. In this stage, concentration of triblock copolymer gradually increased up to critical micelle concentration to form a cylindrical micelle structure. The resulting sample was calcined at 400 ^{o}C for 5 h at a heating rate of 1 ^{o}C/min, and finally, it was further calcined at 700 ^{o}C for 5 h at a heating rate of 5 ^{o}C/min. The prepared ordered mesoporous nickel-alumina catalyst was denoted as OMNA.

For comparison, an ordered mesoporous alumina support (denoted as OMA) was prepared by an EISA method without using a nickel precursor,

according to the similar method described above. A nickel catalyst supported on ordered mesoporous alumina (OMA) was then prepared by an incipient wetness impregnation method. 1.0 g of nickel precursor (nickel nitrate hexahydrate, Sigma-Aldrich) was dissolved in 2.0 ml of anhydrous ethanol. The solution was then added dropwise to 1.0 g of OMA support to impregnate nickel precursor. The resulting sample was dried at 80 ºC for 3 h, and it was finally calcined at 700 ºC for 5 h at a heating rate of 5 ºC/min. The prepared catalyst was denoted as Ni/OMA. The Ni/Al atomic ratio in both Ni/OMA and OMNA catalysts was fixed at 0.17.

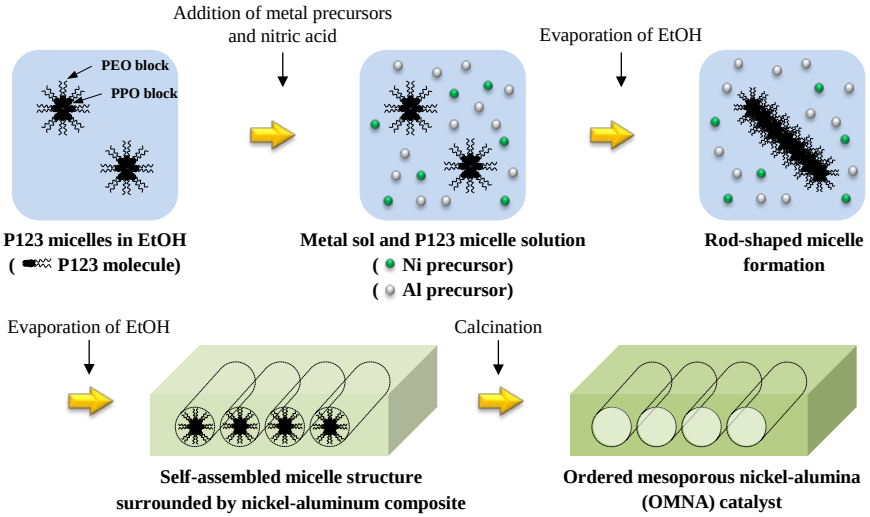

Fig. 2.5. Schematic procedures for the preparation of OMNA catalyst by an evaporation-induced self-assembly.

2.1.6. Preparation of nickel/alumina catalyst by a chemical immobilization method

A nickel/alumina catalyst was prepared by a chemical immobilization method. Fig. 2.6 shows schematic procedures for the preparation of nickel/alumina catalysts. Alumina support (denoted as Al) was prepared by an epoxide-driven sol-gel method as similar method described in Section 2.1.3. 2.7 g of nickel precursor (nickel nitrate hexahydrate, Sigma-Aldrich) was dissolved in 2.0 ml of distilled water (Solution A). 2.6 g of EDTA (ethylenediaminetetraacetic acid, Sigma-Aldrich) was added in 15 ml of distilled water (Solution B). In order to completely solubilize EDTA, pH of Solution B was kept at 8.0 using ammonia solution (Solution C). Solution A was then added dropwise into the solution C to yield blue-colored nickel-EDTA complex solution (Solution D). 1.3 g of Al support was dispersed in 13 ml of distilled water (Solution E). Nitric acid was added dropwise into the solution E until pH = 4 to make surface of Al support positively-charged by protonating hydroxyl groups (Solution F). The solution D was then slowly introduced to the solution F for impregnation of nickel precursor (Solution G). The solution G was heated and stirred for removal of solvent. The resulting material was then dried at 100 ^{o}C, and subsequently calcined at 700 ^{o}C. The obtained nickel/alumina catalyst prepared by a chemical immobilization method was denoted NiE/Al. For comparison, another nickel/alumina catalyst (denoted as Ni/Al) was also prepared by a conventional impregnation method. Nickel loading was kept at 40 wt% in both NiE/Al and Ni/Al catalysts.

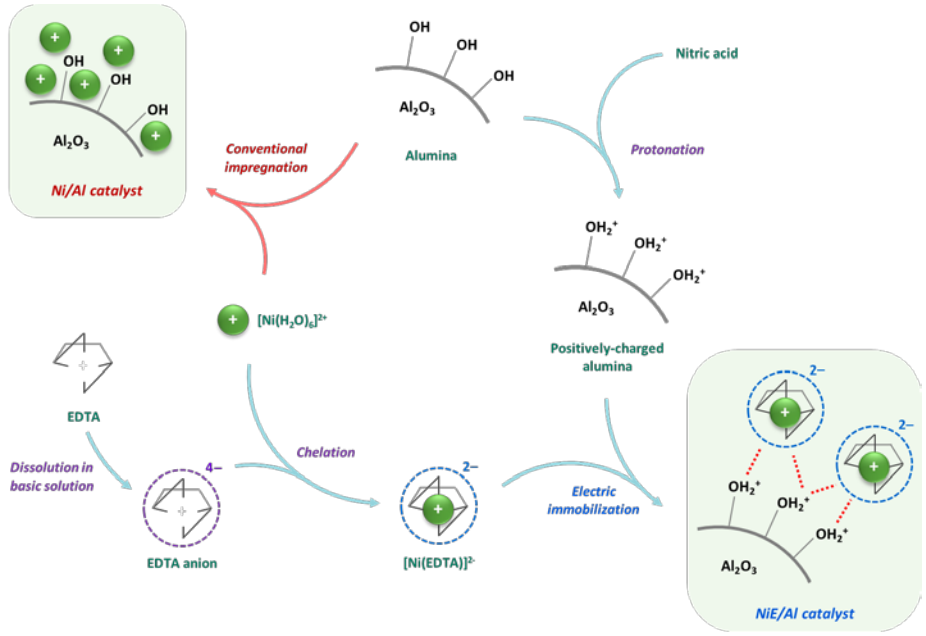

Fig. 2.6. Schematic procedures for the preparation of NiE/Al and Ni/Al catalysts.

2.2. Characterization

2.2.1. Physicochemical properties

Chemical compositions of calcined catalysts were determined by ICP-AES (ICPS-1000IV, Shimadzu) analyses.

In order to evaluate textural properties of the catalysts, nitrogen adsorption-desorption measurements were carried out with ASAP-2010 (Micromeritics) or BELSORP-mini II (BEL Japan) apparatus. Before the measurements, the catalysts were degassed at 150 ^{o}C for 6 h by rotary vacuum pump for removal of moisture and other adsorbed gases on the surface of samples. Surface areas of the catalysts were calculated by the Brunauer-Emmett-Teller (BET) method.

2.2.2. Crystalline structure

X-ray diffraction (XRD) analyses were performed using a D-Max2500-PC (Rigaku) diffractometer operated at 50 kV and 150 mA to examine crystalline characteristics of calcined and reduced catalysts. Diffraction data were collected under Cu-Kα radiation (λ = 1.541 Å) with a scan rate of 10 ^{o}/min. For the XRD of reduced catalysts, 0.1 g of each calcined catalyst was reduced with a mixed stream of H_2 (3 ml/min) and N_2 (30 ml/min) at 700 ^{o}C for 3 h.

Small angle X-ray scattering (SAXS) experiments (GADDS, Bruker)

were performed in order to confirm the ordered mesoporous structure of support and catalysts.

2.2.3. Chemical states of elements

Chemical states of aluminum species in the A-ES and A-AS supports were examined by ^{27}Al MAS NMR (magic angle spinning nuclear magnetic resonance) spectra, which were obtained with a Bruker AVANCE II spectrometer (500 MHz) at an MAS frequency of 11 kHz.

Chemical states of aluminum and phosphorus species in XPA supports were examined by ^{27}Al MAS NMR and ^{31}P MAS NMR spectra obtained using an AVANCE 400 WB spectrometer operated at resonance frequencies of 104 MHz for ^{27}Al and 162 MHz for ^{31}P. MAS frequencies were kept at 10 kHz for ^{27}Al MAS NMR and 7 kHz for ^{31}P MAS NMR.

X-ray photoelectron spectroscopy (XPS) analyses were conducted to determine binding energies of nickel species in the calcined catalysts using an AXIS-HSi (KRATOS) apparatus. All the spectra were calibrated taking C 1s peak at 284.5 eV as a reference.

UV-vis-diffuse reflectance spectra (UV-vis-DRS) of the calcined catalysts were obtained using a Lambda-35 (Perkin-Elmer) spectrometer within the range of 400-800 nm to examine coordination state of nickel species.

2.2.4. Reducibility

Temperature-programmed reduction (TPR) measurements were conducted in order to examine reducibility of catalysts. 50 mg of each catalyst was charged into the U-shaped quartz reactor and then it was reduced with a mixed stream of H_2 (2 ml/min) and N_2 (20 ml/min). TPR profiles were collected using a thermal conductivity detector (TCD) at a heating rate of 5 ^oC/min from room temperature to 1000 ^oC.

2.2.5. Morphological feature

Transmission electron microscopy (TEM) analyses were carried out with JEM-2100 (Jeol) electron microscope operating at 200 kV to examine morphological features of calcined, reduced, and used catalysts.

For the TEM analyses of reduced catalysts, ex-situ reduction with a mixed stream of H_2 (3 ml/min) and N_2 (30 ml/min) was preliminarily conducted before the analyses.

2.2.6. H_2 and CH_4 chemisorption studies

Hydrogen chemisorption experiments (BELCAT-B, BEL Japan) were conducted to measure the nickel surface area, nickel dispersion, and average nickel diameter of reduced catalysts in Sections 3.1 and 3.5. Prior to the chemisorption measurements, 50 mg of each catalyst was reduced with a

mixed stream of hydrogen (2.5 ml/min) and argon (47.5 ml/min) at 700 ^{o}C for 3 h, and subsequently, it was purged with pure argon (50 ml/min) for 15 min at 700 ^{o}C. The sample was then cooled to 50 ^{o}C under a flow of argon (50 ml/min). The amount of hydrogen uptake was measured by periodically injecting diluted hydrogen (5% hydrogen and 95% argon) into the reduced catalyst using an on-line sampling valve. Nickel surface area, nickel dispersion, and average nickel diameter were calculated by assuming that one hydrogen atom occupies one surface nickel atom.

H_2 temperature-programmed desorption (H_2-TPD) measurements were conducted to measure the amount of hydrogen uptake and hydrogen-binding strength on the surface of reduced catalysts using a BELCAT-B (BEL Japan) apparatus equipped with a thermal conductivity detector (TCD). Each catalyst was introduced in a quartz cell and it was reduced at 700 ^{o}C for 3 h with 5% H_2/Ar flow (50 ml/min), and subsequently, it was purged with Ar flow (50 ml/min) for 10 min at 700 ^{o}C. After cooling the cell to 50 ^{o}C under Ar flow (50 ml/min), 5% H_2/Ar flow (50 ml/min) was introduced to saturate the catalyst surface with hydrogen for 30 min. To remove physisorbed hydrogen on the surface of the catalyst, temperature of the cell was maintained at 100 ^{o}C for 1 h. After the cell was cooled to 50 ^{o}C, H_2-TPD measurement was conducted within the temperature range of 50-950 ^{o}C under Ar flow (50 ml/min).

In order to elucidate adsorption behavior of methane on the reduced catalysts, CH_4 temperature-programmed desorption (CH_4-TPD) measurements were carried out in a conventional flow system. 0.1 g of each catalyst was loaded into the U-shaped quartz reactor. It was reduced at 700 °C for 3 h with

a mixed stream of H_2 (3 ml/min) and He (30 ml/min). The reactor was then cooled to room temperature under He flow (30 ml/min) and it was purged for 20 min using He flow (30 ml/min). 20 ml of methane was then pulsed into the reactor every minute at room temperature under a flow of helium (5 ml/min), until the surface of the catalyst was saturated with methane. After purging the reactor with He flow (30 ml/min) at 50 ^oC for 1 h to remove physisorbed methane, temperature of the reactor was increased from room temperature to 900 °C at a heating rate of 10 °C/min under a flow of helium (10 ml/min). H_2 flow (2 ml/min) was also introduced to the reactor during the measurement for complete desorption of adsorbed carbon species. Desorbed species were detected using a GC-MSD (6890N GC-5975MSD, Agilent).

2.2.7. Carbon deposition on used catalysts

The amount of carbon deposition on used catalysts after the reaction was determined by CHNS elemental analyses (CHNS 932, Leco / TruSpec Micro CHNS, Leco).

Temperature-programmed oxidation (TPO) experiments were conducted to investigate the nature of deposited carbon species on the used catalysts using a flow system connected to TCD. 50 mg of each used catalyst was loaded in a quartz tube, and a mixed stream of O_2 (2 ml/min) and He (20 ml/min) was supplied to the system. TPO profiles were obtained within the temperature range of room temperature-900 ^oC with a heating rate of 5 ^oC/min.

2.3. Hydrogen production by steam reforming of LNG

Catalytic performance of the catalysts in the steam reforming of LNG was tested in a fixed-bed flow reactor at 550-600 °C and 1 atm. In order to activate nickel species, each catalyst was preliminarily reduced in the reactor at 700 °C for 3 h under H_2 flow (3 ml/min) and N_2 flow (30 ml/min). Reactor temperature was then fixed at reaction temperature under N_2 flow (30 ml/min). Simulated LNG (CH_4: 4.6 ml/min + C_2H_6: 0.4 ml/min) was then supplied into the reactor together with steam (11.3 ml/min, steam/carbon molar ratio = 2.09) and N_2 flow (30 ml/min). Reaction products were periodically injected to on-line gas chromatograph (ACME 6000, Younglin) equipped with a TCD. Catalytic performance was evaluated by following equations.

$$LNG\ conversion\ (\%) = (1 - \frac{F_{CH_4,out} + F_{C_2H_6,out}}{F_{CH_4,in} + F_{C_2H_6,in}}) \times 100 \quad (2.1)$$

$$Hydrogen\ yield\ (\%) = \frac{F_{H_2,out}}{2 \times F_{CH_4,in} + 3 \times F_{C_2H_6,in}} \times 100 \quad (2.2)$$

$$Composition\ of\ species\ i\ in\ outlet\ gas\ (\%) = \frac{F_{i,out}}{F_{total,out} - F_{N_2,out}} \times 100 \quad (2.3)$$

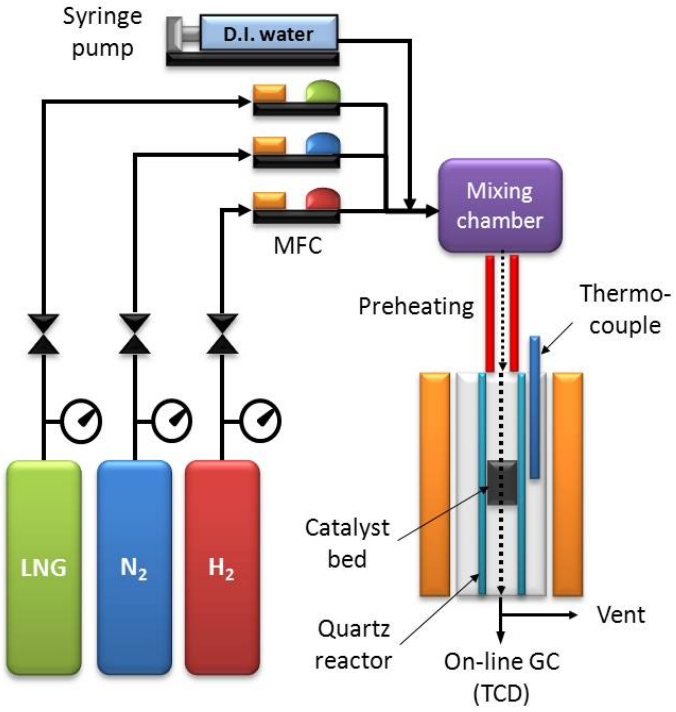

Fig. 2.7. Reaction system for steam reforming of LNG.

Table 2.2

Steam reforming reaction conditions

	Reaction temperature (°C)	Catalyst weight (mg)	S/C molar ratio	Total flow rate (ml/h·g-cat.)
Section 3.1	600	100	2.09	27,793
Section 3.2	600	100	2.09	27,793
Section 3.3	600	100	2.09	27,793
Section 3.4	550	15	2.09	185,285
Section 3.5	600	100	2.09	27,793
Section 3.6	550	20	2.09	138,964

Chapter 3. Results and Discussion

3.1. Mesoporous nickel-alumina aerogel catalyst prepared by a single-step epoxide-driven sol-gel method

3.1.1. Textural properties of calcined catalysts

Both calcined NA-ES and NA-AS catalysts exhibited IV-type isotherms indicative of well-developed mesoporous structure [77]. NA-ES catalyst showed hysteresis loop similar to H1-type, while NA-AS catalyst exhibited H2-type hysteresis loop. It has been reported that IV-type isotherm with H1-type hysteresis loop appears in mesoporous materials comprising nearly spherical-shaped agglomerates [78]. On the other hand, IV-type isotherm with H2-type hysteresis loop is associated with the “ink-bottle” pore structure [60,78]. Thus, it can be inferred that NA-ES catalyst consists of fairly regular spherical-shaped particles compared to NA-AS catalyst.

Detailed textural properties of NA-ES and NA-AS catalysts are summarized in Table 3.1. Both catalysts showed high surface area, large pore volume, and large average pore diameter, representing successful preparation of mesoporous aerogel materials. It is believed that different pore volumes and pore sizes of these catalysts were due to different pore formation mechanism between epoxide-driven sol-gel method and alkoxide-based sol-gel method.

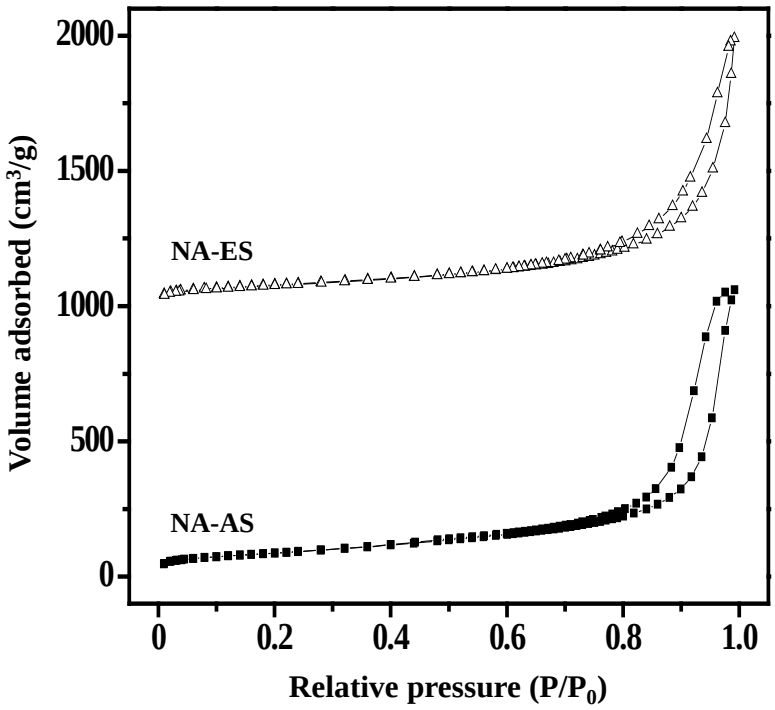

Fig. 3.1. Nitrogen adsorption-desorption isotherms of calcined NA-ES and NA-AS catalysts.

Table 3.1

Detailed textural properties of calcined NA-ES and NA-AS catalysts

Catalyst	Ni/Al atomic ratio[a]	Surface area (m^2/g)[b]	Pore volume (cm^3/g)[c]	Average pore diameter (nm)[d]
NA-ES	0.35	282	1.54	15.8
NA-AS	0.35	296	1.60	16.3

[a] Determined by ICP-AES measurement

[b] Calculated by the BET equation

[c] BJH desorption pore volume

[d] BJH desorption average pore diameter

3.1.2. Crystalline structures of calcined catalysts

Fig. 3.2 shows the XRD patterns of NA-ES and NA-AS catalysts calcined at 700 ºC. It was found that NA-ES and NA-AS catalysts exhibited no characteristic diffraction peaks corresponding to bulk nickel oxide (solid lines in Fig. 3.2). Instead, both NA-ES and NA-AS catalysts showed three distinct diffraction peaks corresponding to nickel aluminate phase (closed circles in Fig. 3.2). It should be noted that the diffraction peaks of γ-Al_2O_3 (440) (dashed line in Fig. 3.2) shifted to a lower diffraction angle in both catalysts. This is because cationic deficient sites in the lattice of Al_2O_3 were expanded by the incorporation of Ni^{2+} ions [79,80]. From these results, it can be inferred that nickel species were finely dispersed in alumina as a form of nickel aluminate with the strong interaction between nickel and alumina support derived from Ni-O-Al composite structure.

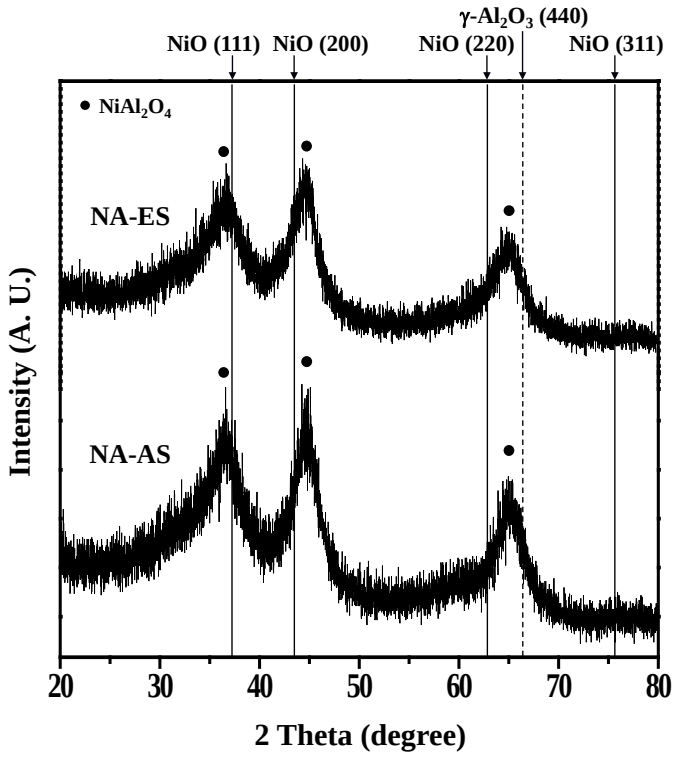

Fig. 3.2. XRD patterns of calcined NA-ES and NA-AS catalysts.

3.1.3. Effect of preparation method on chemical states of aluminum species

^{27}Al MAS NMR analyses were conducted to investigate chemical states of aluminum species in the A-ES and A-AS supports. Although ^{27}Al MAS NMR analyses of NA-ES and NA-AS catalysts were also carried out, significant decrease in NMR signal (poor resolution of peaks) was observed. This is due to the presence of paramagnetic nickel species in the Al_2O_3 supports. It is known that NMR signal is reduced when a paramagnetic metal ion is near the NMR nucleus [81]. Therefore, we obtained NMR spectra of A-ES and A-AS supports to indirectly investigate the effect of preparation method on chemical states of Al atoms in the Al_2O_3 crystalline structures.

It is known that chemical states of Al atoms can be classified into three types; octahedral (Al^{VI}), pentahedral (Al^{V}), and tetrahedral (Al^{IV}) coordination [82,83]. As-synthesized Al_2O_3, which is composed of $Al(OH)_3$, mainly has octahedrally coordinated Al atoms. During the thermal treatment, however, these octahedrally coordinated Al atoms in $Al(OH)_3$ migrate toward tetrahedral or pentahedral coordination sites because of dehydration and dehydroxylation of $Al(OH)_3$ [84].

As shown in Fig. 3.3, both A-ES and A-AS supports exhibited three peaks at around 8, 37, and 67 ppm, corresponding to octahedrally coordinated Al, pentahedrally coordinated Al, and tetrahedrally coordinated Al, respectively. These NMR spectra were deconvoluted to three bands, and percentages of peak area were calculated as presented Table 3.2. It is noted

that the peak area percentage for pentahedrally coordinated Al in the A-ES support was much larger than that in the A-AS support, representing that a more defective structure was formed in the A-ES support. Because epoxide served as an acid scavenger in the epoxide-driven sol-gel method, gelation process in the epoxide-driven sol-gel method was faster than that in the alkoxide-based sol-gel method. As a result, unsaturated Al atoms were more easily formed in the epoxide-driven sol-gel method than in the alkoxide-based sol-gel method. In other words, disorder in coordination state of Al atoms easily occurred in the epoxide-driven sol-gel method. According to previous study [85], pentahedrally coordinated Al atoms act as Lewis acid center on the surface of γ-Al_2O_3. When Ni^{2+} ions incorporate into the lattice of Al_2O_3, Lewis acid sites serve as anchoring sites for nickel species. From this, it is believed that large amount of pentahedrally coordinated Al atom as electron-deficient sites was responsible for fine dispersion of nickel species on the surface of NA-ES catalyst. It was also found that chemical shifts of Al atoms in the A-ES support were smaller than those in the A-AS support. This might be due to the less deshielded environment around Al atom in the A-ES support. It is believed that the formation of less deshielded environment around Al atoms in the A-ES support was caused by decrease in amount of high coordination state of Al atoms as represented in Table 3.2.

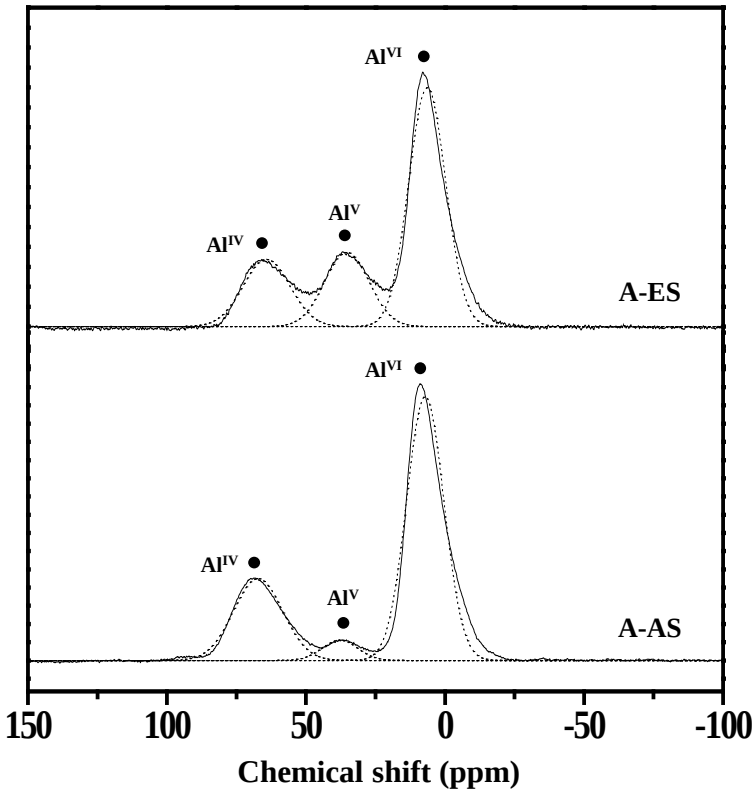

Fig. 3.3. ^{27}Al MAS NMR spectra of calcined A-ES and A-AS supports.

Table 3.2

Chemical states of aluminum species in the A-ES and A-AS supports calcined at 700 ^{o}C

Support	A-ES		A-AS	
	Chemical shift (ppm)	Peak area (%)	Chemical shift (ppm)	Peak area (%)
Al^{VI} (Octahedral)	7.9	57.9	8.8	67.5
Al^{V} (Pentahedral)	36.2	21.5	37.1	4.9
Al^{IV} (Tetrahedral)	66.0	20.6	68.1	27.6

3.1.4. Reducibility and metal-support interaction

TPR measurements were carried out to examine the interaction between nickel species and Al_2O_3 support in the Ni-Al_2O_3 aerogel catalysts. Fig. 3.4 shows the TPR profiles of NA-ES and NA-AS catalysts calcined at 700 ºC. It was found that the reduction peak temperature of NA-ES catalyst was lower than that of NA-AS catalyst. In other words, nickel species in the NA-ES catalyst was more reducible than those in the NA-AS catalyst, although nickel loading in the catalysts was nearly identical. It is known that tetrahedral coordination sites or octahedral coordination sites of Al_2O_3 support are occupied by Ni^{2+} ions during the preparation of Ni-Al_2O_3 catalysts, resulting in the formation of nickel aluminate phase [86]. Ni^{2+} ions in the octahedral coordination sites of Al_2O_3 support (Ni_{oct}) are more reducible than those in the tetrahedral coordination sites of Al_2O_3 support (Ni_{tet}). From these results, it is inferred that NA-ES catalyst exhibiting a lower reduction temperature mainly consists of more reducible Ni_{oct} compared to NA-AS catalyst. This is because smaller amount of octahedrally coordinated Al atom was formed by the epoxide-driven sol-gel method than by the alkoxide-based sol-gel method (Table 3.2). Therefore, Ni^{2+} ions can easily occupy cationic vacancies in the octahedral coordination sites of Al_2O_3 support in the NA-ES catalysts.

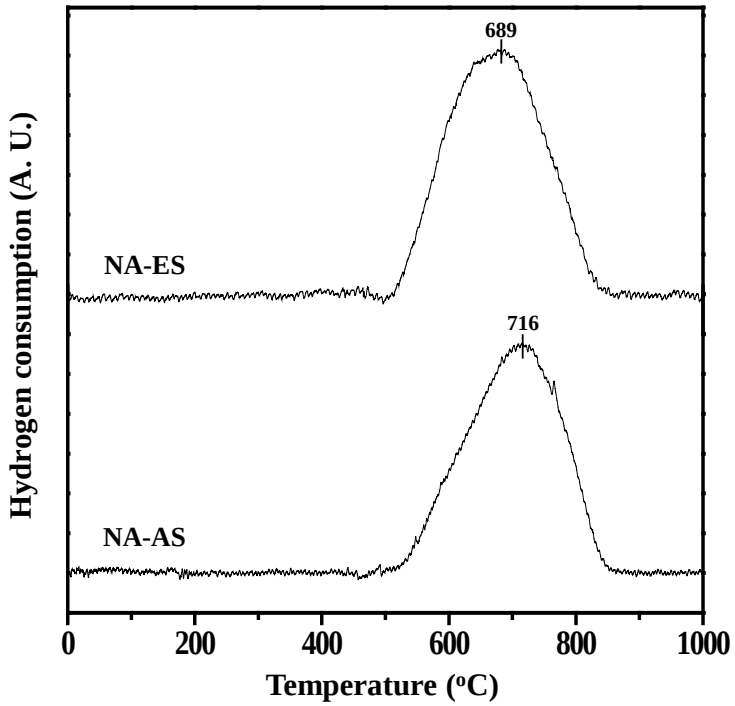

Fig. 3.4. TPR profiles of calcined NA-ES and NA-AS catalysts.

3.1.5. Characterization of reduced catalysts

XRD patterns of NA-ES and NA-AS catalysts reduced at 700 ^{o}C are presented in Fig. 3.5. It is noticeable that the diffraction peak of γ-Al_2O_3 (440) in the calcined catalysts shifted to the higher diffraction angle (Figs. 3.2 and 3.5), i.e., toward original diffraction angle of γ-Al_2O_3 (440) phase (dashed line in Fig. 3.5). Furthermore, the reduced catalysts showed diffraction peaks corresponding to metallic nickel (solid lines in Fig. 3.5). This implies that nickel aluminate phase in both calcined NA-ES and NA-AS catalysts were successfully reduced into metallic nickel during the reduction process employed in this work.

Hydrogen chemisorption measurements were conducted in order to determine the nickel surface area, nickel dispersion, and average nickel diameter in the reduced NA-ES and NA-AS catalysts. Hydrogen chemisorption results for reduced NA-ES and NA-AS catalysts are listed in Table 3.3. The amount of hydrogen uptake and nickel surface area of NA-ES catalysts were larger than those of NA-AS catalyst. Consequently, active nickel species were more finely dispersed in the NA-ES catalyst than in the NA-AS catalyst, resulting in smaller average nickel diameter in the NA-ES catalyst. This implies that NA-ES catalyst exhibited stronger resistance toward aggregation of nickel species during the reduction process than NA-AS catalyst.

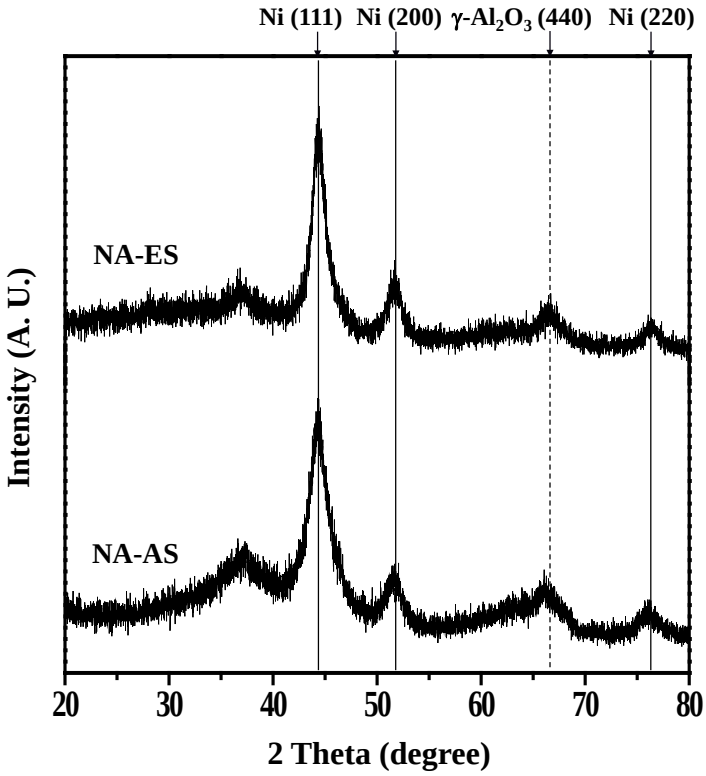

Fig. 3.5. XRD patterns of reduced NA-ES and NA-AS catalysts.

Table 3.3

Hydrogen chemisorption results for reduced NA-ES and NA-AS catalysts

Catalyst	NA-ES	NA-AS
Amount of hydrogen uptake (μmol/g-catalyst)[a]	174.4	154.6
Nickel surface area (m^2/g-catalyst)[a]	13.6	12.0
Nickel dispersion (%)[a]	7.2	6.3
Average nickel diameter (nm)[a]	14.1	15.9

[a] Calculated by assuming $H/Ni_{atom}=1$

3.1.6. Catalytic performance in the steam reforming of LNG

Fig. 3.6 shows the LNG conversions and hydrogen yields with time on stream in the steam reforming of LNG over NA-ES and NA-AS catalysts at 600 ^{o}C. Both NA-ES and NA-AS catalysts showed a stable catalytic performance without any significant catalyst deactivation during the steam reforming reaction. It is believed that fine dispersion of active metallic nickel species on the catalysts was responsible for stable catalytic performance by suppressing carbon deposition and nickel sintering. CHNS analysis revealed that the amounts of carbon deposited on the surface of NA-ES and NA-AS catalysts after a 1000 min-reaction were very small (1.6 and 2.3 wt%, respectively).

NA-ES catalyst exhibited a higher catalytic activity in the steam reforming of LNG than NA-AS catalyst in terms of LNG conversion and hydrogen yield. This result was due to fine dispersion of active nickel species in the NA-ES catalyst. Average nickel diameter served as an important factor determining the catalytic performance in the steam reforming of LNG. According to previous kinetic study on the steam reforming of methane [87], C-H bond cleavage of methane on the surface active nickel site is known as a rate-determining step for overall reaction. It has also been reported that methane is more preferentially adsorbed on active nickel sites where the energy level for dehydrogenated methane can be lowered [88]. This indicates that small nickel particle is favorable for high catalytic activity in the steam reforming reaction, because stronger interaction between active nickel site and

reactant is possible on the smaller nickel particle, causing a stabilization effect on the adsorbed intermediate.

Compositions of outlet gas obtained after a 1000 min-reaction over NA-ES and NA-AS catalysts are presented in Fig. 3.7. Composition of carbon monoxide over NA-ES catalyst was larger than that over NA-AS catalyst, while composition of carbon dioxide over NA-ES catalyst was smaller than that over NA-AS catalyst. This result indicates water-gas shift reaction (equation (3.1)) was suppressed over NA-ES catalyst during the steam reforming reaction. This is because smaller nickel particles are easier to contact surface of Al_2O_3, resulting a formation of weak bond between carbon monoxide and nickel particles [87]. From this result, it can be inferred that steam reforming of methane (equation (3.2)) occurred more actively than water-gas shift reaction over the NA-ES catalyst, resulting higher hydrogen yield over the NA-ES catalyst.

$$CO + H_2O \leftrightarrow CO_2 + H_2 \quad (3.1)$$

$$CH_4 + H_2O \leftrightarrow CO + 3H_2 \quad (3.2)$$

It is concluded that NA-ES catalyst with small average nickel diameter served as an efficient catalyst for hydrogen production by steam reforming of LNG. Small nickel particles of NA-ES catalyst were favorable for strong interaction between reactant and catalyst surface. High reducibility of nickel species in the NA-ES catalyst was also partly responsible for excellent catalytic performance in the steam reforming reaction.

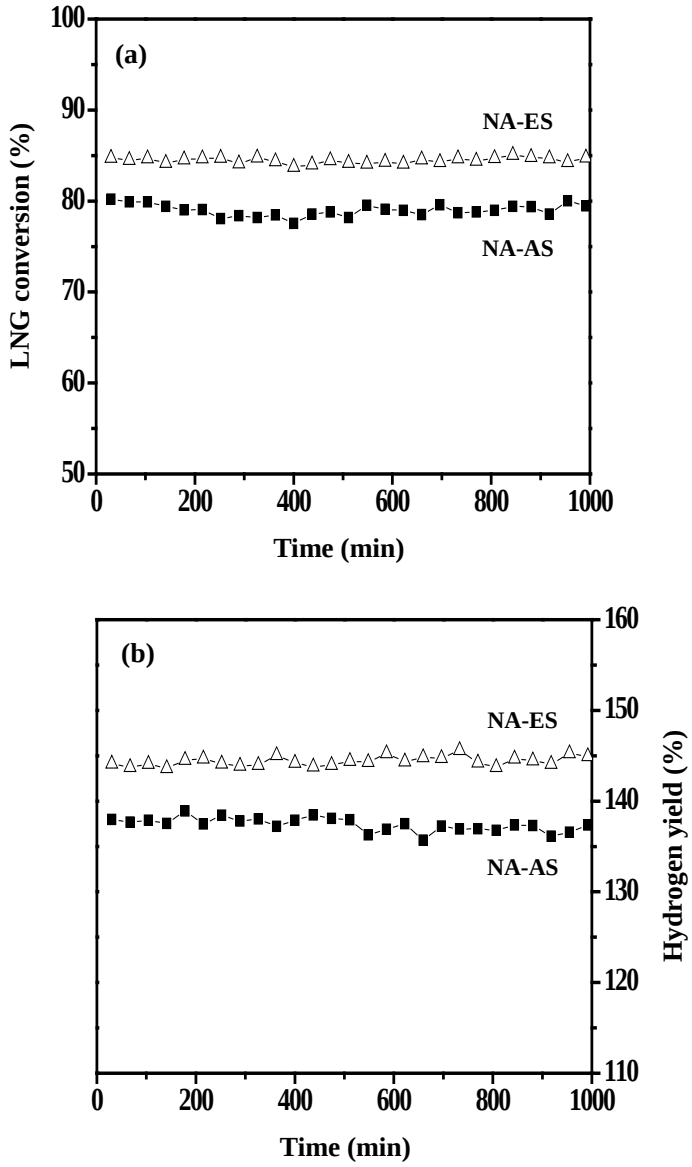

Fig. 3.6. (a) LNG conversions and (b) hydrogen yields with time on stream in the steam reforming of LNG over NA-ES and NA-AS catalysts at 600 ºC. All the catalysts were reduced at 700 ºC for 3 h prior to the reaction.

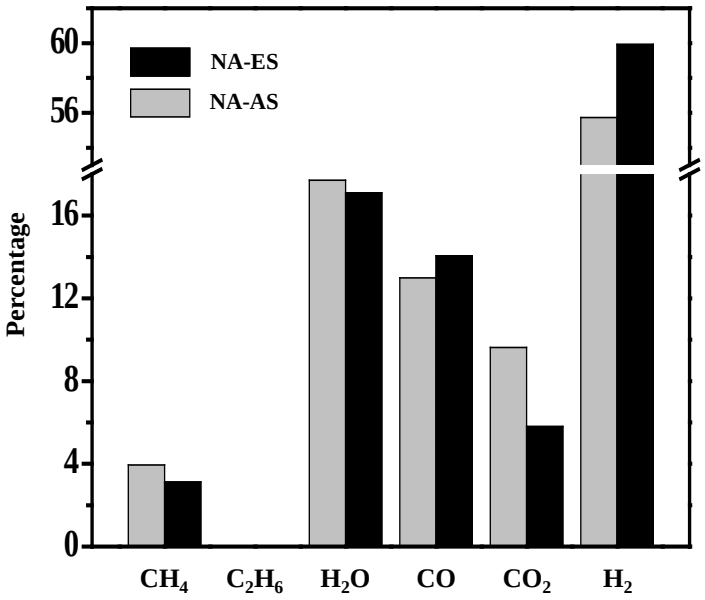

Fig. 3.7. Compositions of outlet gas obtained after a 1000 min-reaction over NA-ES and NA-AS catalysts.

3.2. Mesoporous nickel-alumina xerogel catalyst prepared by a carbon-templating sol-gel method

3.2.1. Textural properties of calcined catalysts

Fig. 3.8(a) shows the nitrogen adsorption-desorption isotherms of CNAX catalysts. CNA0 catalyst exhibited IV-type isotherm, indicating the formation of well-developed mesoporous structure [77,78]. On the other hand, CNAX (X = 6, 12, 18, and 24) catalysts exhibited IV-type-like isotherms at relative pressure lower than ca. 0.9, and additional increase of nitrogen adsorption was observed at high relative pressure. This implies that additional pore structure was formed by carbon template in the catalysts. The effect of carbon template on the textural properties of CNAX (X = 6, 12, 18, and 24) catalysts was also observed in the BJH pore size distribution of the catalysts as presented in Fig. 3.8(b). It was found that CNAX (X = 6, 12, 18, and 24) catalysts exhibited large pores than CNA0 catalyst.

Detailed textural properties of CNAX (X = 0, 6, 12, 18, and 24) catalysts calcined at 700 ^{o}C are summarized in Table 3.4. All the prepared catalysts retained high surface area (> 275 m^2/g), large pore volume (> 0.5 cm^3/g), and large average pore size (> 5.6 nm). It was found that surface area, pore volume, and average pore diameter of CNAX catalysts increased with increasing the amount of carbon template. This means that mesoporosity of nickel-alumina xerogel catalysts can be controlled by the carbon template which occupies the space in the wet gel.

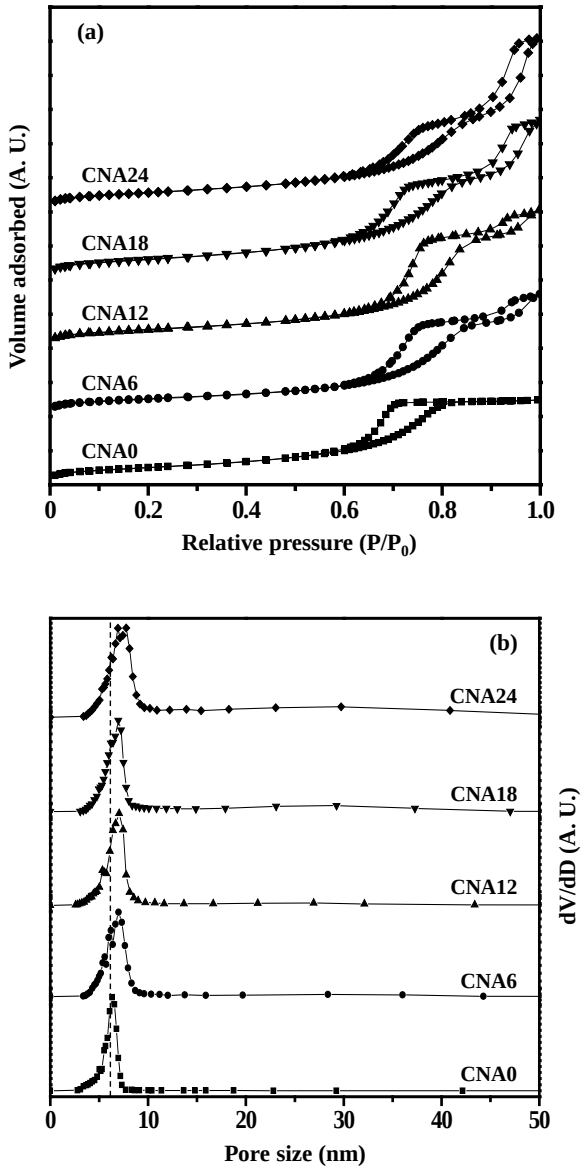

Fig. 3.8. (a) Nitrogen adsorption-desorption isotherms and (b) BJH pore size distributions of calcined CNAX (X = 0, 6, 12, 18, and 24) catalysts.

Table 3.4

Detailed textural properties of calcined CNAX catalysts

Catalyst	Ni/Al atomic ratio[a]	Surface area (m^2/g)[b]	Pore volume (cm^3/g)[c]	Average pore diameter (nm)[d]
CNA0	0.35	275.8	0.58	5.6
CNA6	0.36	279.2	0.84	8.1
CNA12	0.35	298.5	0.94	8.3
CNA18	0.35	312.2	1.09	8.8
CNA24	0.34	314.4	1.18	10.8

[a] Determined by ICP-AES measurement
[b] Calculated by the BET equation
[c] BJH desorption pore volume
[d] BJH desorption average pore diameter

3.2.2. Crystalline structure of calcined catalysts

Crystalline structures of calcined CNAX (X = 0, 6, 12, 18, and 24) catalysts were investigated by XRD analyses as shown in Fig. 3.9(a). It has been reported that γ-Al_2O_3 phase is formed within the temperature range of 500-800 ^oC and γ-Al_2O_3 is structurally stable within this temperature range [88]. Therefore, it is inferred that all the CNAX catalysts calcined at 700 ^oC for 5 h retained a stable γ-Al_2O_3 phase interacting with nickel species. It is noticeable that the diffraction peaks of γ-Al_2O_3 (440) shifted to a lower diffraction angle in all the catalysts. This indicates that incorporation of Ni^{2+} ions into cationic deficient sites of γ-Al_2O_3 lattice caused lattice expansion of γ-Al_2O_3 through formation of nickel aluminate phase [42,80].

It is interesting to note that CNA18 and CNA24 catalysts exhibited not only characteristic diffraction peaks corresponding to nickel aluminate phase (solid lines in Fig. 3.9(a)) but also small diffraction peaks corresponding to bulk nickel oxide phase (closed circles in Fig. 3.9(a)). On the other hand, CNAX (X = 0, 6, and 12) catalysts exhibited only three diffraction peaks indicative of nickel aluminate phase. This means nickel species in the CNAX (X = 0, 6, and 12) catalysts were more finely dispersed in the form of nickel aluminate phase than those in the CNA18 and CNA24 catalysts. This is because the number of aluminum species adjacent to nickel species decreased with increasing the amount of carbon template in the preparation of nickel-alumina xerogel catalyst. When a large amount of carbon template was used for the preparation of nickel-alumina xerogel catalyst, mesopores were readily

generated and nickel species located on the surface of mesopore would weakly interact with aluminum species. This will provide more chance of local nickel oxide formation because nickel species weakly incorporated into alumina lattice can be more generated. Thus, it can be summarized that crystalline structure of nickel-alumina xerogel catalysts was changed by the amount of carbon template used.

TPR measurements were carried out to examine the interaction between nickel species and alumina in the CNAX (X = 0, 6, 12, 18, and 24) catalysts. Fig. 3.9(b) shows the TPR profiles of CNAX catalysts calcined at 700 ^{o}C. All the CNAX catalysts retained a single reduction band within the range of 600-710 ^{o}C. Considering that reduction band appearing in the range of 400-800 ^{o}C is associated with the reduction of nickel oxide interacting with alumina, these reduction bands might be due to the reduction of surface nickel aluminate phase, not bulk nickel aluminate phase [89,90]. It has been reported that surface nickel aluminate phase has an intermediate nickel species-alumina interaction between bulk nickel oxide-alumina and bulk nickel aluminate-alumina interactions [91]. Therefore, all the CNAX catalysts with intermediate nickel species-alumina interaction are expected to have not only high stability compared to bulk nickel oxide but also high reducibility compared to bulk nickel aluminate.

Reduction peak of CNAX catalysts shifted to a lower temperature with increasing the amount of carbon template. This indicates that nickel species in the CNAX catalysts became more reducible as the amount of carbon template increased. According to the previous studies [92,93], Ni^{2+} ions occupy octahedral or tetrahedral coordination sites in alumina lattice after calcination.

Because Ni^{2+} ions located in the octahedral coordination sites of alumina lattice (Ni_{oct}) are more reducible than those in the tetrahedral sites (Ni_{tet}), Ni_{oct}/Ni_{tet} ratio in the CNAX catalysts is believed to increase with increasing the amount of carbon template. In case of CNA18 and CNA24 catalysts, which showed additional diffraction peaks attributed to bulk nickel oxide phase in XRD measurements, it can be inferred that bulk nickel oxide phase was also responsible for their high reducibility. Therefore, it is thought that the interaction between nickel species and alumina was closely related to the composition of crystalline phases of CNAX catalysts.

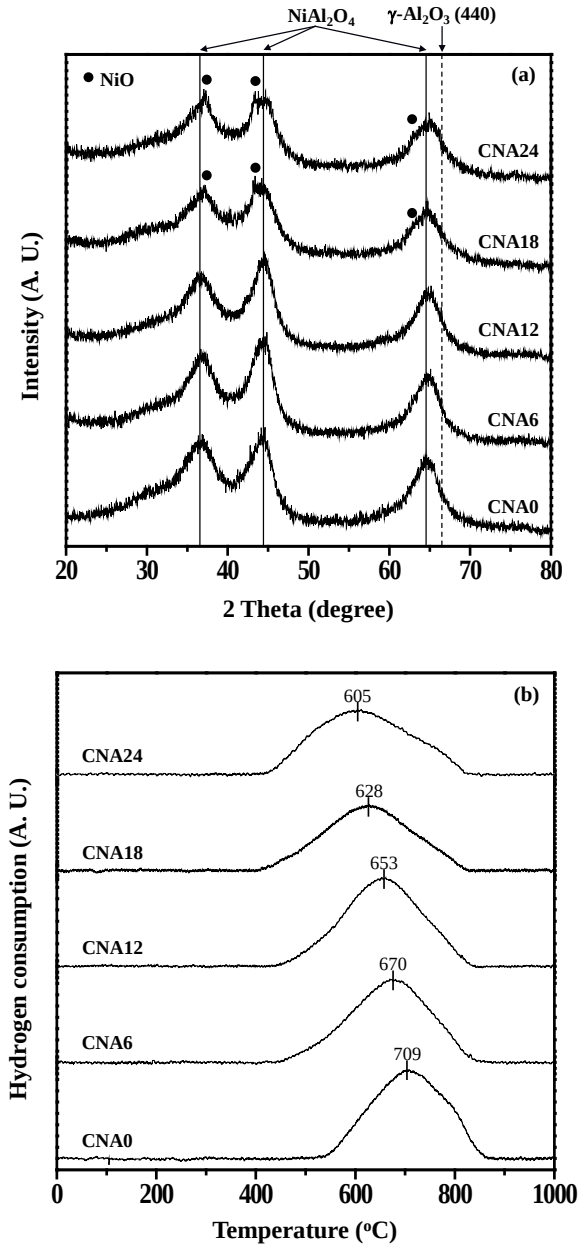

Fig. 3.9. (a) XRD patterns and (b) TPR profiles of calcined CNAX (X = 0, 6, 12, 18, and 24) catalysts.

3.2.3. Characterization of reduced catalysts

Fig. 3.10 shows the XRD patterns of CNAX (X = 0, 6, 12, 18, and 24) catalysts reduced at 700 ^{o}C for 3 h. It was found that the diffraction peak of γ-Al_2O_3 (440) (dashed line in Fig. 3.10) moved back to the original diffraction angle in all the reduced CNAX catalysts, when compared to the diffraction peak in the calcined CNAX catalysts (Fig. 3.9(a)). Moreover, neither bulk nickel oxide phase nor nickel aluminate phase was detected in all the reduced catalysts. Instead, all the reduced CNAX catalysts exhibited diffraction peaks corresponding to metallic nickel (solid lines in Fig. 3.10). This indicates that nickel species in the CNAX catalysts were readily reduced into metallic nickel during the reduction process employed in this work.

It should be noted that sharpness of diffraction peaks corresponding to metallic nickel in the reduced CNAX catalysts was different depending on the amount of carbon template. Crystallite size of metallic nickel in the reduced CNAX (X = 0, 6, 12, 18, and 24) catalysts was calculated by the Scherrer equation as presented in Table 3.5. Crystallite size of metallic nickel in the reduced CNAX catalysts showed a volcano-shaped trend with respect to the amount of carbon template. This trend is believed to be due to changes in textural properties and metal-support interaction of CNAX catalysts. As the amount of carbon template increased, textural properties such as surface area, pore volume, and average pore diameter of CNAX catalysts were enhanced as listed in Table 3.4. Therefore, it is expected that crystallite size of metallic nickel in the reduced CNAX (X = 0, 6, and 12) catalysts decreased with

increasing the amount of carbon template, because sintering of metallic nickel can be suppressed by the well-developed mesoporous structure. When a large amount of carbon template was used in the preparation of CNAX (X = 18 and 24) catalysts, however, crystallite size of metallic nickel was not decreased even though mesoporosity of the catalyst was improved. Although CNA18 and CNA24 catalysts retained similar crystallite size of metallic nickel, slight change of crystallite size of metallic nickel was not negligible. This was due to the fact that interaction between nickel species and alumina support became too weak to prevent sintering of metallic nickel species during the reduction process at large amount of carbon template. Among the catalysts prepared, CNA12 catalyst retained the smallest crystallite size (4.8 nm) of metallic nickel, suggesting an effective improvement in resistance toward sintering of active nickel phase.

TEM analyses were also conducted to confirm the above result. Fig. 3.11(a) shows that the reduced CNA0 catalyst retained relatively large metallic nickel particles compared to the reduced CNA12 (Fig. 3.11(b)) and CNA24 (Fig. 3.11(c)) catalysts. Furthermore, metallic nickel particles in the reduced CNA24 catalyst (Fig. 3.11(c)) were more aggregated than those in the reduced CNA12 catalyst (Fig. 3.11(b)). These TEM observations were well consistent with the XRD results (Fig. 3.10).

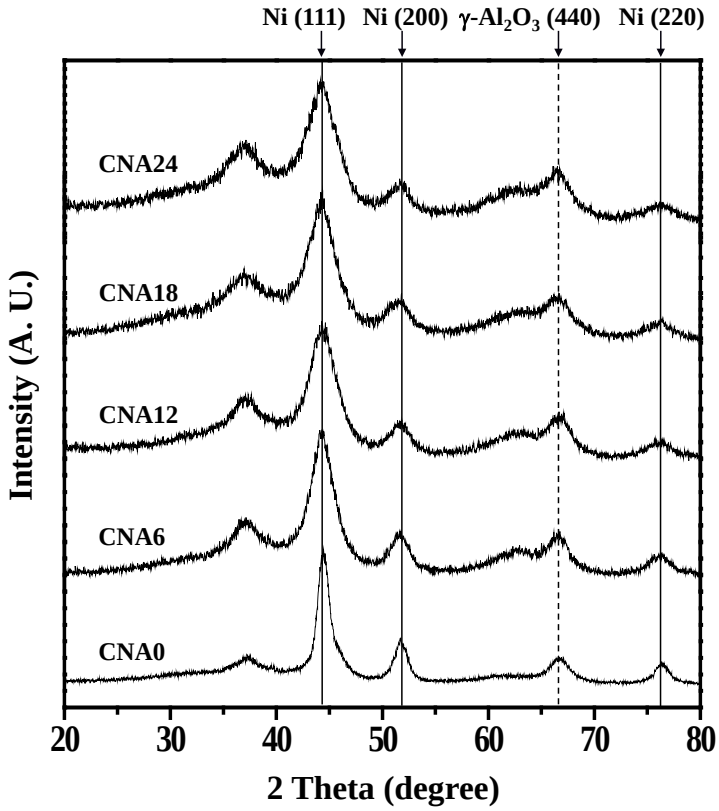

Fig. 3.10. XRD patterns of reduced CNAX (X = 0, 6, 12, 18, and 24) catalysts.

Table 3.5

Crystallite sizes of metallic nickel in the reduced CNAX catalysts

Catalyst	Crystallite size of metallic nickel (nm)[a]
CNA0	6.5
CNA6	5.8
CNA12	4.8
CNA18	5.0
CNA24	5.4

[a] Calculated by the Scherrer equation from Ni (200) diffraction peak broadening in Fig. 3.10

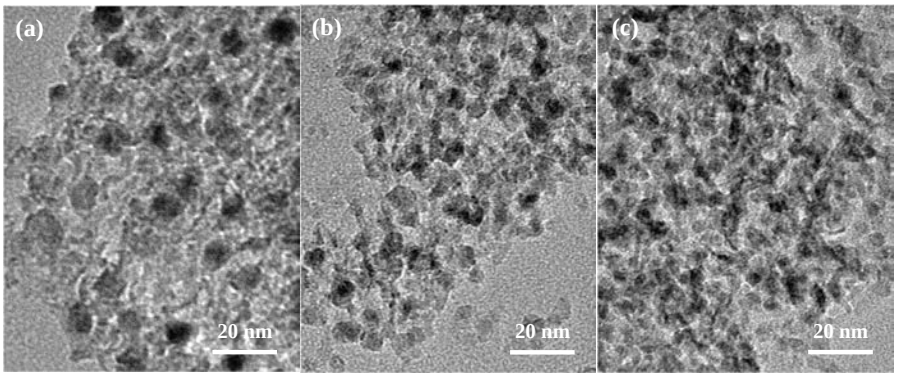

Fig. 3.11. TEM images of reduced (a) CNA0, (b) CNA12, and (c) CNA24 catalysts.

3.2.4. Catalytic performance in the steam reforming of LNG

Fig. 3.12 shows the LNG conversion and hydrogen yield with time on stream in the steam reforming of LNG over CNAX (X = 0, 6, 12, 18, and 24) catalysts at 600 ºC. CNAX (X = 0, 6, 12, and 18) catalysts exhibited a stable catalytic performance during the steam reforming reaction. Well-developed mesoporosity of the catalysts might play an important role in promoting internal mass transfer of reactants and products in the steam reforming reaction. Furthermore, small active nickel species interacting with alumina support in the CNAX (X = 0, 6, 12, and 18) catalysts were also responsible for their excellent catalytic activity. However, CNA24 catalyst experienced a catalyst deactivation during the reaction. The main reason for catalyst deactivation of CNA24 catalyst can be deduced by the fact that nickel species in the CNA24 catalyst were weakly bound to alumina support compared to those in the other catalysts. These nickel species weakly interacting with alumina support in the CNA24 catalyst are vulnerable to carbon deposition during the steam reforming reaction, because nickel species can easily migrate on the catalyst surface to be sintered.

A Ni/Al_2O_3 catalyst prepared by a conventional impregnation method using nickel nitrate and commercial alumina support (Degussa) also showed a significant catalyst deactivation. Initial LNG conversion (68.1%) and initial hydrogen yield (109.4%) of Ni/Al_2O_3 catalyst were lower than those of CNAX (X = 0, 6, 12, 18, and 24) catalysts, because crystallite size of metallic nickel (12.0 nm) in the reduced Ni/Al_2O_3 catalyst was quite larger than that in

the CNAX catalysts. This suggested that CNAX catalysts exhibited not only high catalytic activity but also high stability compared to Ni/Al_2O_3 catalyst.

Fig. 3.13(a) shows that both initial LNG conversion and initial hydrogen yield showed volcano-shaped curves with respect to the amount of carbon template. Among the catalysts tested, CNA12 catalyst exhibited the best initial catalytic activity in the steam reforming reaction. This was due to the smallest nickel crystallite size of CNA12 catalyst. Fig. 3.13(b) shows the LNG conversion and hydrogen yield after a 1000 min-reaction over CNAX (X = 0, 6, 12, 18, and 24) catalysts in the steam reforming of LNG, plotted as a function of the amount of carbon template. Catalytic performance of CNAX catalysts after a 1000 min-reaction decreased in the order of CNA12 > CNA18 > CNA6 > CNA0 > CNA24. These two correlations shown in Fig. 3.13(a) and Fig. 3.13(b) strongly indicate that an appropriate metal-support interaction was required for long-term stability in the steam reforming of LNG.

Fig. 3.14 shows the correlations between crystallite size of metallic nickel and initial catalytic activity of CNAX catalysts in the steam reforming of LNG. Interestingly, initial LNG conversion and initial hydrogen yield increased with decreasing crystallite size of metallic nickel of the catalysts. It means that crystallite size of metallic nickel in the CNAX catalysts played an important role in determining catalytic performance in the steam reforming of LNG. According to the previous studies [87,88], high catalytic activity in the steam reforming reaction can be achieved by enhancing the active nickel surface area. That is, small nickel particles are favorable for excellent catalytic performance in the reaction due to large active surface area for dehydrogenation reaction of LNG.

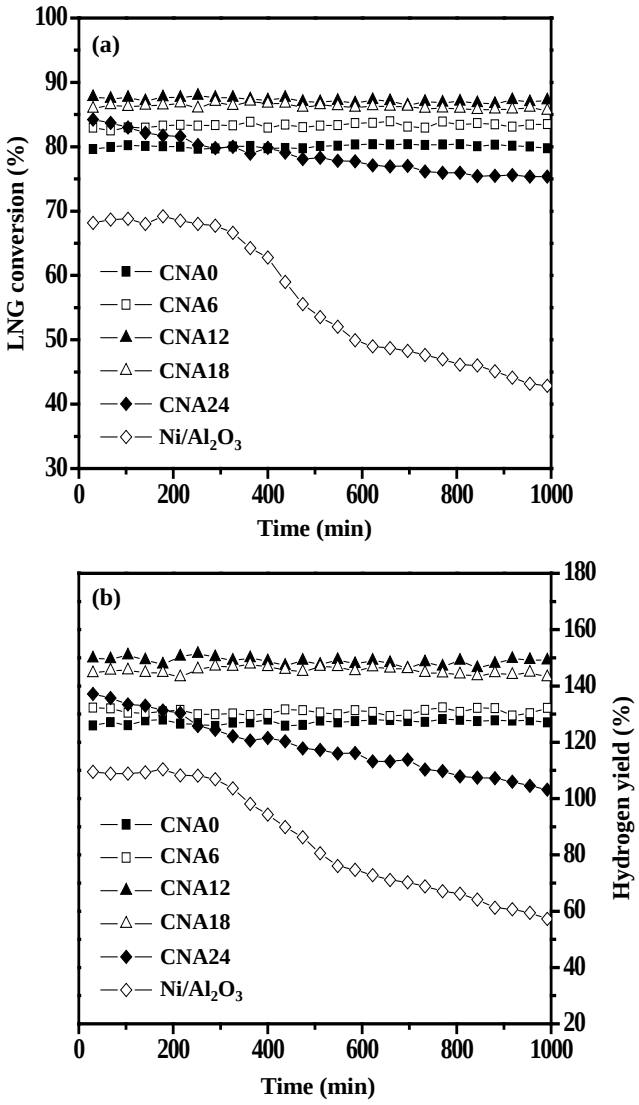

Fig. 3.12. (a) LNG conversion and (b) hydrogen yield with time on stream in the steam reforming of LNG over CNAX (X = 0, 6, 12, 18, and 24) catalysts at 600 °C. All the catalysts were reduced at 700 °C for 3 h prior to the reaction (For comparison, catalytic performance data for nickel catalyst supported on commercial alumina (denoted as Ni/Al_2O_3) were also presented).

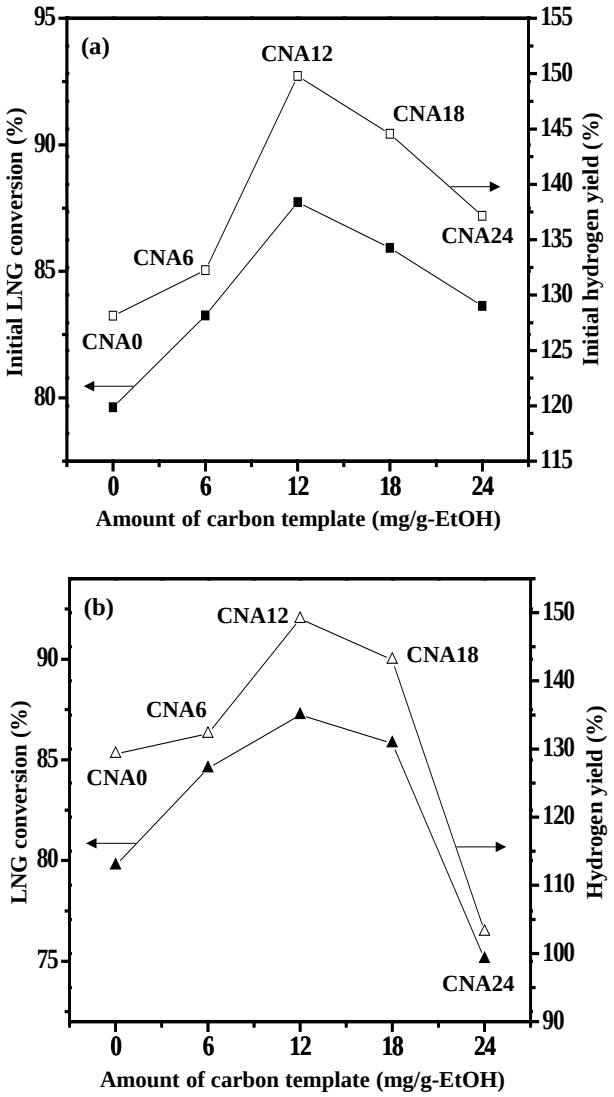

Fig. 3.13. (a) Initial LNG conversion and initial hydrogen yield and (b) LNG conversion and hydrogen yield after a 1000 min-reaction over CNAX (X = 0, 6, 12, 18, and 24) catalysts in the steam reforming of LNG, plotted as a function of the amount of carbon template.

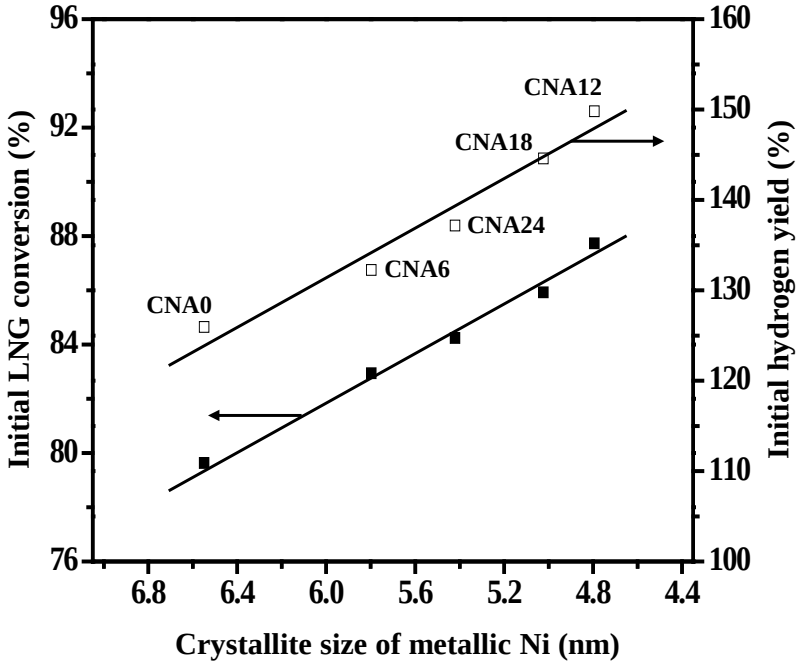

Fig. 3.14. Correlations between crystallite size of metallic nickel and initial catalytic performance of CNAX (X = 0, 6, 12, 18, and 24) catalysts in the steam reforming of LNG.

3.2.5. Characterization of used catalysts

Fig. 3.15 shows the TEM images of the used CNA0, CNA12, and CNA24 catalysts obtained after a 1000 min-reaction. The used CNA24 catalyst (Fig. 3.15(c)) retained large agglomerates of nickel particles on the surface compared to the reduced CNA24 catalyst (Fig. 3.11(c)), while CNA0 and CNA12 catalyst showed no significant morphological change before and after the reaction. This implies that metallic nickel weakly bound to alumina support in the CNA24 catalyst was sintered during the steam reforming reaction. Furthermore, filamentous carbon tubes were observed in the used CNA24 catalyst (Fig. 3.15(d)). Because a number of adjacent nickel atoms can serve as a carbon growth point, filamentous carbon tubes can be easily formed on the surface of CNA24 catalyst with large metallic nickel particle. In particular, sintered nickel particles lifted-up by carbon tubes were also observed in the CNA24 catalyst. This phenomenon might affect the catalytic performance of CNA24 catalyst, because nickel particles isolated from the alumina support drastically lost catalytic activity and stability.

Fig. 3.16 shows the XRD patterns of CNAX (X = 0, 6, 12, 18, and 24) catalysts obtained after a 1000 min-reaction. It was observed that CNA24 catalyst exhibited a diffraction peak of graphitic carbon (closed circle in Fig. 3.16) after the reaction. This can be understood by the fact that carbon deposition reaction preferentially occurred on the surface of large nickel particles [87]. This result was also supported by crystallite size of metallic nickel in the used CNAX catalyst obtained after the reaction as listed in Table

3.6, suggesting that CNA24 catalyst with the largest crystallite size of metallic nickel was vulnerable to carbon deposition. It is believed that large amount of carbon deposition on the surface of CNA24 catalyst prevented the adsorption of reactants to the active sites, resulting in deactivation of CNA24 catalyst.

The amount of carbon deposition on the surface of CNAX (X = 0, 6, 12, 18, and 24) catalysts was quantitatively measured by CHNS elemental analysis as summarized in Table 3.6. Among the catalysts tested, CNA12 catalyst retained the smallest amount of carbon deposition after a 1000 min-reaction. This indicates that CNA12 catalyst with the smallest crystallite size of metallic nickel has strong resistance toward carbon deposition. Therefore, it is concluded that CNA12 catalyst with the smallest crystallite size of metallic nickel served as the most efficient catalyst in the hydrogen production by steam reforming of LNG.

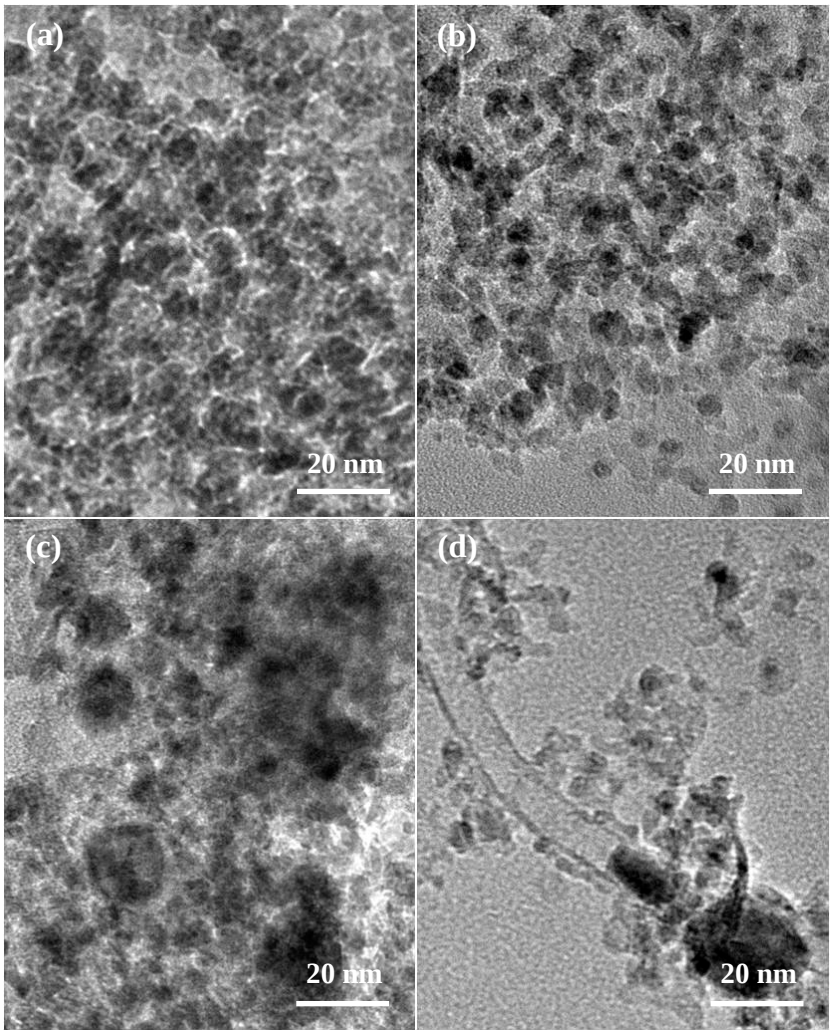

Fig. 3.15. TEM images of (a) CNA0, (b) CNA12, (c) and (d) CNA24 catalysts obtained after a 1000 min-reaction at 600 ºC.

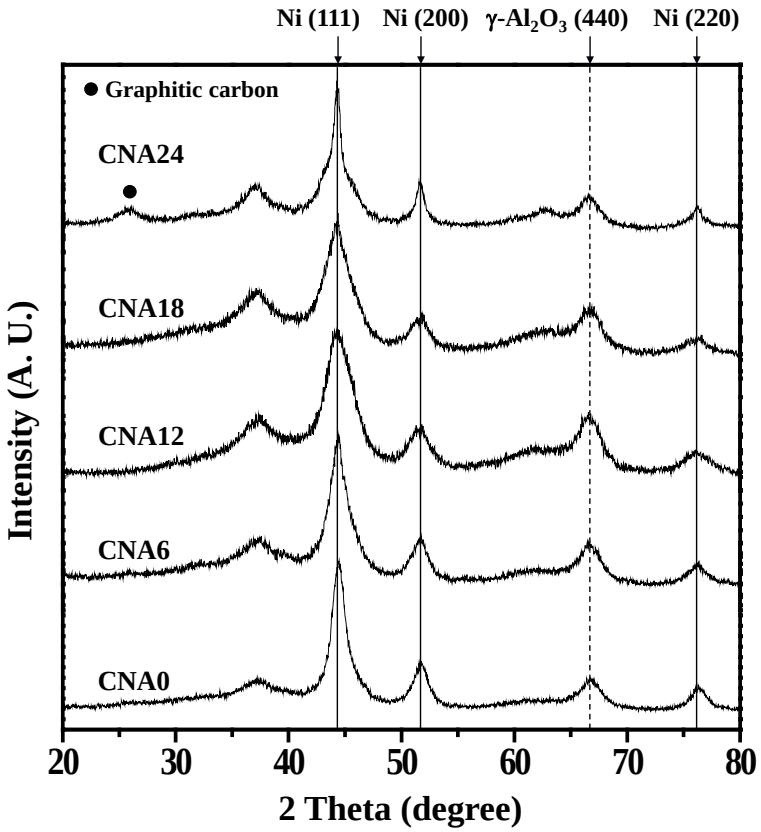

Fig. 3.16. XRD patterns of CNAX (X = 0, 6, 12, 18, and 24) catalysts obtained after a 1000 min-reaction at 600 ºC.

Table 3.6

Crystallite sizes of metallic nickel and amount of carbon deposition in the CNAX catalysts after a 1000 min-reaction

Catalyst	Crystallite size of metallic nickel (nm)[a]	Amount of carbon deposition (wt%)[b]
CNA0	6.7	3.5
CNA6	6.1	0.6
CNA12	4.9	0.2
CNA18	5.6	0.4
CNA24	10.2	11.3

[a] Calculated by the Scherrer equation from Ni (200) diffraction peak broadening in Fig. 3.16

[b] Determined by CHNS elemental analysis

3.3. Mesoporous nickel catalyst supported on phosphorus-modified alumina xerogel

3.3.1. Characterization of calcined supports

Fig. 3.17(a) shows the nitrogen adsorption-desorption isotherms of calcined 0PA, 0.02PA, and 0.20PA supports. All the XPA supports exhibited IV-type isotherms, which were attributed to the well-developed mesoporous structure [78]. It is interesting to note that the positions of limiting nitrogen uptake region were changed with a variation of P/Al molar ratio. 0PA and 0.05PA supports retained similar shapes of hysteresis loops, except that 0.05PA support showed higher height of limiting nitrogen uptake than 0PA support. On the other hand, 0.20PA support exhibited a quite different hysteresis loop with relatively small area and low steepness. A close examination revealed that the amount of limiting nitrogen uptake was maintained until low relative pressure at ca. 0.45-0.50 in the desorption branch of 0.20PA support. These results imply that 0.20PA support retained a mesoporous structure with low uniformity and small pore size compared to 0PA and 0.05PA supports [75].

Detailed textural properties of calcined XPA (X = 0, 0.02, 0.05, 0.10, and 0.20) supports are summarized in Table 3.7. All the XPA supports exhibited large surface area (> 340 m^2/g), large pore volume (> 0.3 cm^3/g), and large pore diameter (> 3 nm), indicating successful formation of mesoporous structure. It is noteworthy that surface area of XPA (X = 0.02,

0.05, 0.10, and 0.20) supports was larger than that of 0PA support, and surface area of XPA supports showed a volcano-shaped trend. This was because phosphate groups dispersed in the framework of phosphorus-aluminum gel modified the surface and pore structure of aluminum oxide. In other words, addition of phosphorus into alumina matrix was responsible for generation of complex surface morphology and porous structure of alumina. Excessive addition of phosphorus was revealed to be disadvantageous due to hindrance of phosphate or phosphorus-containing oxide on the formation of mesoporous network in alumina. In the similar manner, pore volume and pore diameter of XPA supports also showed volcano-shaped trends.

Crystalline structures of calcined XPA (X = 0, 0.02, 0.05, 0.10, and 0.20) supports were examined by XRD measurements as shown in Fig. 3.17(b). Diffraction peaks corresponding to γ-Al_2O_3 phase were detected in all the XPA supports. However, intensities for diffraction peaks decreased with increasing P/Al molar ratio in the XPA supports. This means that the addition of phosphorus makes alumina support more amorphous by acting as a structural modifier. In addition, phosphorus might induce a defective structure in alumina support during the calcination process. No distinct phosphorus-related species such as aluminum phosphate were observed in the XRD patterns of XPA supports, representing that phosphorus species were amorphously distributed in alumina. Only a broad diffraction band at ca. $2\theta = 25^{o}$ attributed to incorporation of phosphorus into alumina lattice was detected in the 0.20PA support.

In order to elucidate chemical states of aluminum species in the calcined XPA (X = 0, 0.02, 0.05, 0.10, and 0.20) supports, ^{27}Al MAS NMR

spectra of the supports were obtained as shown in Fig. 3.18. According to the previous studies [82,83], there are three types of aluminum species in transition alumina; octa-coordinated aluminum (Al^{VI}), penta-coordinated aluminum (Al^{V}), and tetra-coordinated aluminum (Al^{IV}). Cross-linking between octa-coordinated aluminum species of aluminum hydroxide is known to cause migration or transformation of aluminum into penta- and tetra-coordinated aluminum species [84]. A defective and vacant structure in alumina formed in this process is related to the generation of penta-coordinated aluminum species. As presented in Fig. 3.18, all the calcined XPA supports retained three peaks at around 0, 30, and 60 ppm, corresponding to octa-coordinated aluminum, penta-coordinated aluminum, and tetra-coordinated aluminum, respectively. Relative distribution of each aluminum species was calculated from the deconvoluted peaks of NMR spectra as listed in Table 3.8. It is noteworthy that the amount of octa-coordinated aluminum decreased while that of penta- and tetra-coordinated aluminum increased with increasing P/Al molar ratio of the XPA supports. This indicates that phosphorus caused transition of octa-coordinated aluminum species in the XPA supports into coordinately unsaturated penta- and tetra-coordinated aluminum species through the formation of Al-O-P linkage in composite oxide as reported in the literature [94]. This might be because rapid gelation by phosphorus species located in the XPA supports with higher P/Al molar ratio induced more defective and vacant sites, resulting in much coordinately unsaturated aluminum species. Penta-coordinated aluminum is known to act as a Lewis acid site which can serve as an anchoring site for metal ions [85]. Therefore, it is expected that nickel species located on the surface of XPA

support with high population of penta-coordinated aluminum more abundantly interact with the support than those on the XPA support with low population of penta-coordinated aluminum. Nevertheless, chemical shift of penta-coordinated aluminum species in the XPA supports moved to a lower chemical shift with increasing P/Al molar ratio, demonstrating that strength of aluminum species for anchoring nickel species decreased with increasing P/Al molar ratio. The explanation for this phenomenon is that the addition of electron-rich phosphorus was effective for changing aluminum to be less electron deficient (more shielded).

^{31}P MAS NMR spectra of calcined XPA (X = 0.02, 0.05, 0.10, and 0.20) supports are presented in Fig. 3.19. All the XPA supports exhibited a broad signal within the chemical shift ranging from 0 to -30 ppm. This broad band is related to the small amount of phosphorus species and various environments around phosphorus species. It was found that NMR peak moved to a lower chemical shift (upfield) region with increasing P/Al molar ratio of XPA supports, suggesting that phosphorus species in the form of phosphate group (PO_4) were transformed to tetrahedral phosphorus species such as $P(OAl)_4$ [94]. As P/Al molar ratio increased, more phosphorus would be linked with oxygen atom connected to aluminum in the supports. In this way, the environments around aluminum and phosphorus species could be changed by varying P/Al molar ratio in the XPA supports.

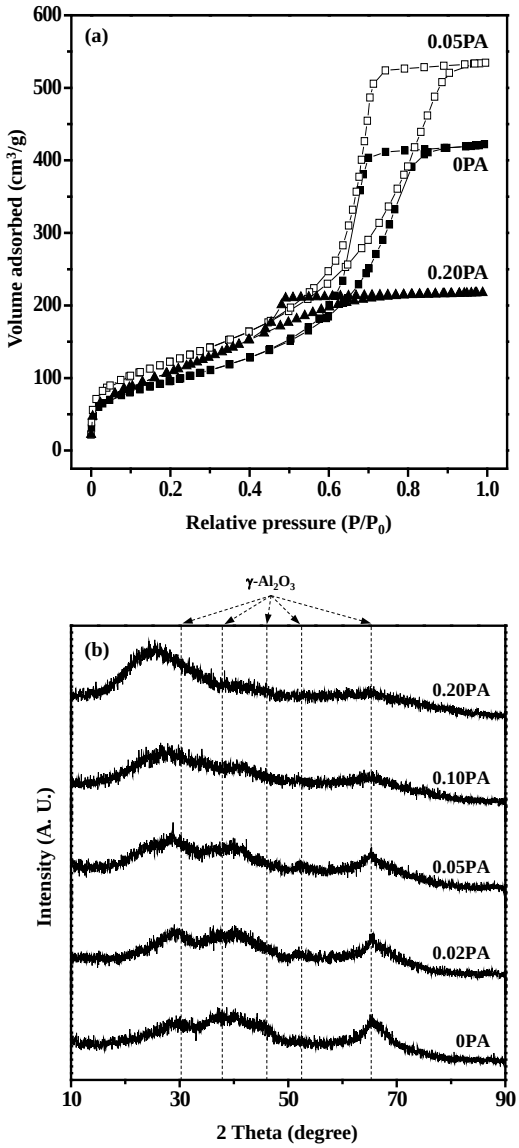

Fig. 3.17. (a) Nitrogen adsorption-desorption isotherms of calcined XPA (X = 0, 0.05, and 0.20) supports, and (b) XRD patterns of calcined XPA (X = 0, 0.02, 0.05, 0.10, and 0.20) supports.

Table 3.7

Textural properties of calcined supports (XPA) and catalysts (Ni/XPA)

	Sample	Ni/(P+Al) molar ratio[a]	P/Al molar ratio[a]	Surface area (m^2/g)[b]	Pore volume (cm^3/g)[c]	Pore diameter (nm)[d]
Support	0PA	-	0	345	0.65	7.6
	0.02PA	-	0.02	414	0.91	8.8
	0.05PA	-	0.05	444	0.83	7.4
	0.10PA	-	0.10	395	0.36	3.7
	0.20PA	-	0.20	388	0.34	3.3
Catalyst	Ni/0PA	0.18	0	230	0.46	7.9
	Ni/0.02PA	0.18	0.02	271	0.64	9.4
	Ni/0.05PA	0.18	0.05	274	0.55	8.0
	Ni/0.10PA	0.18	0.10	280	0.26	3.7
	Ni/0.20PA	0.18	0.20	282	0.21	3.0

[a] Determined by ICP-AES measurement

[b] Calculated by the BET equation

[c] Total pore volume at $P/P_0 \sim 0.995$

[d] Mean pore diameter

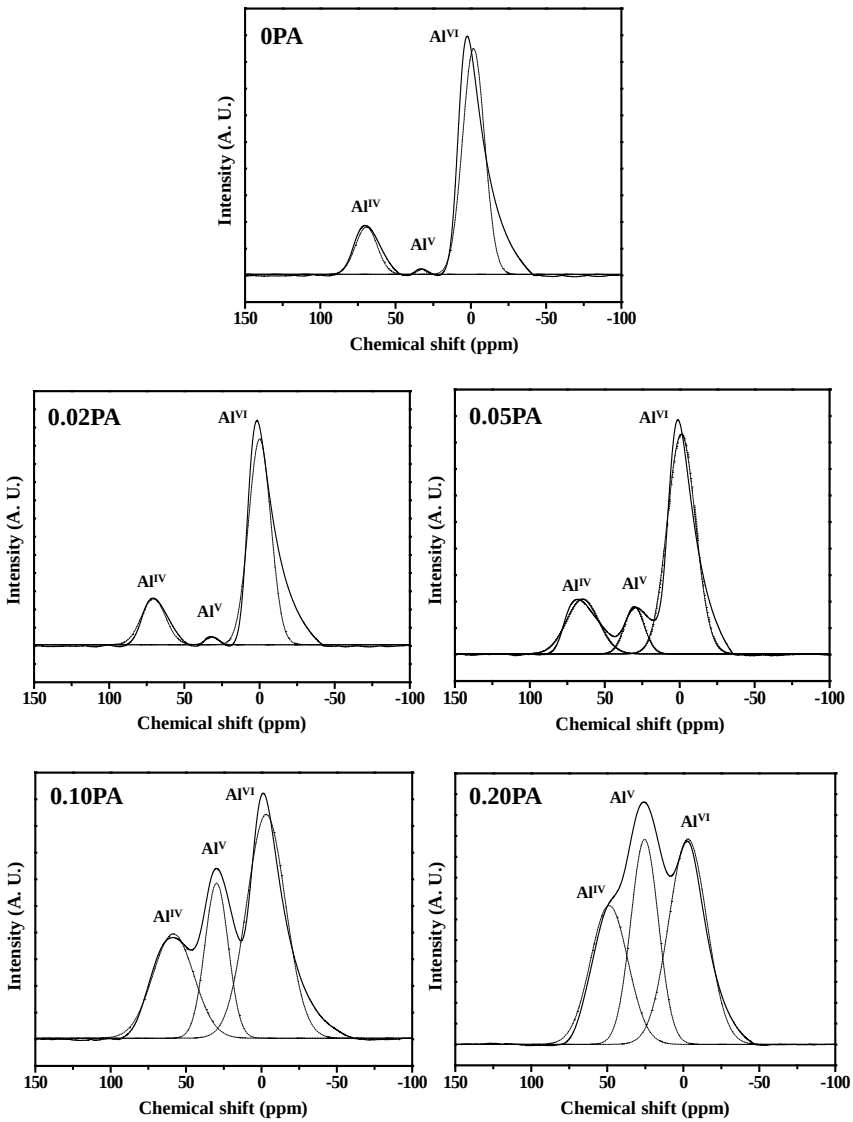

Fig. 3.18. ^{27}Al MAS NMR spectra of calcined XPA (X = 0, 0.02, 0.05, 0.10, and 0.20) supports.

Table 3.8

Chemical states of aluminum species in the XPA supports

Support	Chemical shift of penta-coordinated Al (ppm)	Relative distribution (%)[a]		
		Octa-coordinated Al (Al^{VI})	Penta-coordinated Al (Al^{V})	Tetra-coordinated Al (Al^{IV})
0PA	32.7	82.2	0.7	17.1
0.02PA	31.5	78.9	1.8	19.3
0.05PA	30.3	69.8	10.4	19.8
0.10PA	29.6	52.4	21.8	25.8
0.20PA	25.6	41.8	30.4	27.8

[a] Calculated from the deconvoluted curve in Fig. 3.18

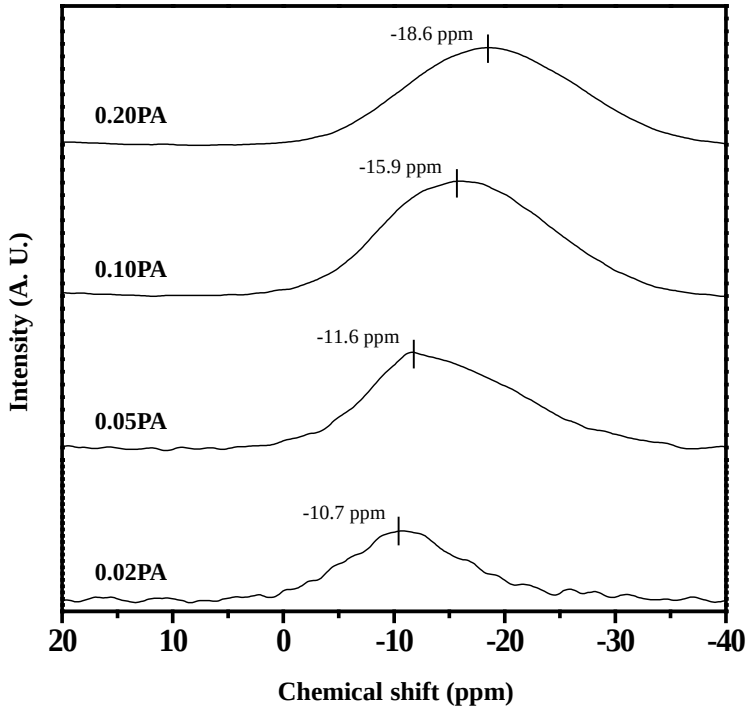

Fig. 3.19. ^{31}P MAS NMR spectra of calcined XPA (X = 0.02, 0.05, 0.10, and 0.20) supports.

3.3.2. Characterization of calcined catalysts

Fig. 3.20(a) shows the nitrogen adsorption-desorption isotherms of calcined Ni/XPA (X = 0, 0.05, and 0.20) catalysts. Although the isotherms of Ni/0.02PA and Ni/0.10PA catalysts were not shown here, it was observed that all the calcined Ni/XPA catalysts (X = 0, 0.02, 0.05, 0.10, and 0.20) exhibited IV-type isotherms with H2-type hysteresis loops. This indicates that the calcined Ni/XPA catalysts still maintained a mesoporous structure like XPA supports (Fig. 3.17(a)). As summarized in Table 3.7, however, all the calcined Ni/XPA catalysts retained smaller surface area and smaller pore volume than the calcined XPA supports. This is because mesopores in the XPA supports were considerably blocked by nickel species during the impregnation step and deformed by the additional calcination step. On the other hand, Ni/XPA (X = 0.02, 0.05, 0.10, and 0.20) catalysts still retained larger surface area than Ni/0PA catalyst. This might be due to the fact that the calcined XPA support retained more penta-coordinated aluminum species which served as anchoring sites for nickel with increasing P/Al molar ratio, as discussed in Section 3.3.1.

Crystalline structures of calcined Ni/XPA (X = 0, 0.02, 0.05, 0.10, and 0.20) catalysts were investigated as presented in Fig. 3.20(b). Five diffraction peaks ascribed to nickel oxide phase (solid lines in Fig. 3.20(b)) were detected in all the calcined catalysts. Intensities of diffraction peaks for nickel oxide phase gradually increased with increasing P/Al molar ratio of calcined Ni/XPA catalysts. Although nickel aluminate phase (dashed lines in Fig. 3.20(b)) were also detected, intensities of nickel aluminate monotonically

decreased with increasing P/Al molar ratio of calcined Ni/XPA catalysts. Thus, it can be inferred that nickel species existed in the form of nickel oxide and nickel aluminate, and the relative distribution of these forms was varied with P/Al molar ratio. In connection with NMR results of calcined XPA supports explained in Section 3.3.1, the XRD results revealed that nickel species dispersed in phosphorus-modified alumina support were gradually released from nickel aluminate spinel structure to nickel oxide phase on acidic aluminum species (coordinately unsaturated aluminum species) with increasing P/Al molar ratio. Therefore, the amount of aluminum species for anchoring nickel species increased while the strength of anchoring decreased with increasing P/Al molar ratio as discussed in ^{27}Al MAS NMR results. This resulted in the increase of nickel oxide phase which was known to have weaker metal-support interaction than nickel aluminate phase [91].

In order to examine metal-support interaction in the calcined Ni/XPA (X = 0, 0.02, 0.05, 0.10, and 0.20) catalysts, TPR measurements were conducted as shown in Fig. 3.21(a). The reduction peaks detected at around 950-970 ^{o}C were associated with reduction of phosphorus species bound to oxygen [95]. It was observed that Ni/0.02PA catalyst did not show a reduction band within that temperature range. This might be because phosphorus content was too small to form a certain reducible phosphorus species. All the calcined Ni/XPA catalysts showed a reduction peak at around 733-757 ^{o}C which was attributed to reduction of nickel aluminate spinel or nickel oxide strongly interacted with alumina [89]. It is interesting to note that shape of this reduction peak was gradually changed more asymmetrically and the peak moved toward a higher temperature with increasing P/Al molar ratio of

Ni/XPA (X = 0, 0.02, 0.05, 0.10, and 0.20) catalysts. It is believed that the asymmetrical feature of the reduction band was due to the existence of nickel aluminate ($NiAl_2O_4$) and nickel oxide strongly interacted with support. The increased reduction peak temperature with increasing P/Al molar ratio of the catalysts was due to the enhanced metal-support interaction of nickel species in the form of nickel aluminate spinel, because phosphorus partly located in the XPA support induced lower degree of nickel saturation of the spinel [96]. Another peak attributed to reduction of bulk nickel oxide phase was detected in the TPR profiles of Ni/0.10PA and Ni/0.20PA catalysts at around 349-374 ^{o}C. Thus, it can be summarized that binding of nickel species in the form of nickel oxide in the phosphorus-modified alumina supports was weakened with increasing P/Al molar ratio, because affinity of acidic aluminum species toward nickel species decreased as discussed in ^{27}Al MAS NMR spectra of XPA supports. Although nickel species were still bound in the XPA support as a form of nickel aluminate or nickel oxide with strong metal-support interaction with increasing P/Al molar ratio until 0.05, some amounts of nickel species were excluded from the XPA support as a bulk nickel oxide phase when P/Al molar ratio was 0.1 and 0.2.

Fig. 3.21(b) shows the XPS spectra in the Ni 2p level of calcined Ni/XPA (X = 0, 0.02, 0.05, 0.10, and 0.20) catalysts. Deconvolution of the XPS spectra was performed by the Gaussian curve-fitting method. It has been reported that two Ni $2p_{3/2}$ peaks are observed at 855-856 eV and 853-854 eV; the former is attributed to nickel species in the form of nickel aluminate or nickel oxide strongly interacted with support, while the latter is attributed to nickel species in the form of bulk nickel oxide [97]. However, one peak was

detected in the XPS spectra of Ni/XPA (X = 0, 0.02, and 0.05) catalysts due to the presence of nickel aluminate. On the other hand, Ni/0.10PA and Ni/0.20PA catalysts exhibited two peaks in the XPS spectra, representing that nickel species existed as nickel aluminate phase and bulk nickel oxide phase. Furthermore, binding energies of Ni $2p_{3/2}$ peak at 855-856 eV increased due to the increased metal-support interaction of nickel aluminate phase with increasing P/Al molar ratio until 0.20, as discussed in the TPR results. Additional XPS analyses for P 2p level of calcined catalysts (not shown here) revealed that phosphorus-related compounds such as nickel phosphate were not formed in the calcined Ni/XPA (X = 0.02, 0.05, 0.10, and 0.20) catalysts.

Fig. 3.22 represents the UV-vis-DRS spectra of calcined Ni/XPA (X = 0, 0.02, 0.05, 0.10, and 0.20) catalysts. The reflectance band at 720 nm corresponds to nickel species with octahedral coordination (Ni_{oct}) normally formed in nickel oxide phase, while the bands at 600 nm and 640 nm are attributed to nickel species with tetrahedral coordination (Ni_{tet}) in nickel aluminate phase [98,99]. It was observed that the reflectance band of Ni_{oct} species (720 nm) became stronger with increasing P/Al molar ratio of Ni/XPA catalysts, demonstrating that Ni_{oct}/Ni_{tet} ratio increased with increasing P/Al molar ratio. This indicates that the coordination of nickel species in the catalysts can be controlled by phosphorus addition. Ni_{oct} species are also known to be readily reducible compared to Ni_{tet} species. Thus, we can say that easily reducible nickel species were more formed with increasing P/Al molar ratio. This result was well consistent with TPR results showing that binding of nickel species in the form of nickel oxide in the supports was weakened due to the phosphorus addition.

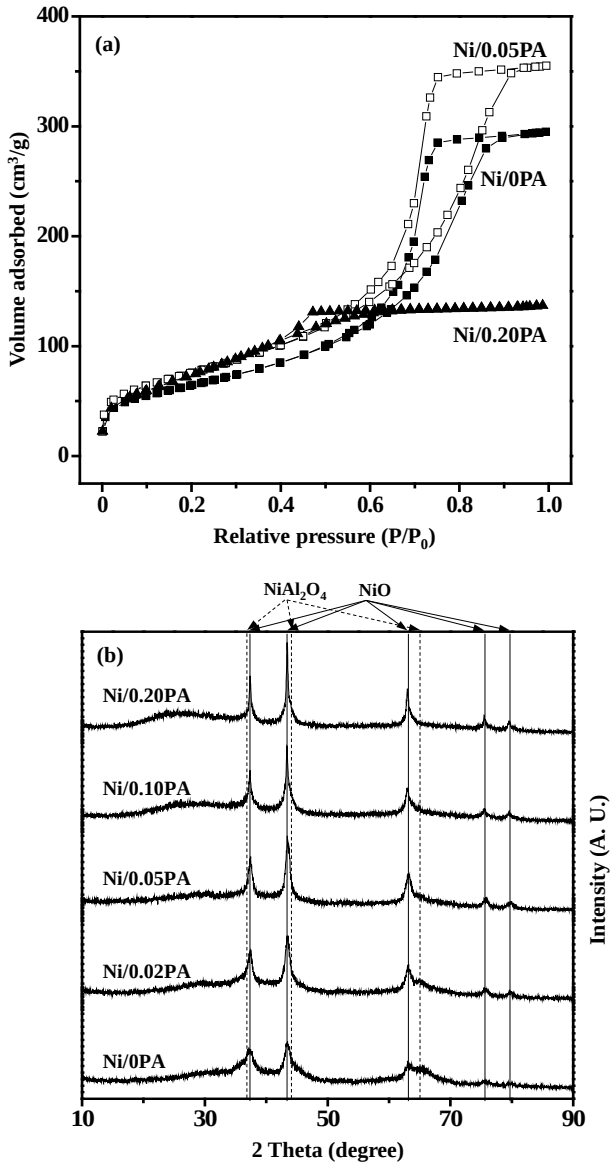

Fig. 3.20. (a) Nitrogen adsorption-desorption isotherms of calcined Ni/XPA (X = 0, 0.05, and 0.20) catalysts, and (b) XRD patterns of calcined Ni/XPA (X = 0, 0.02, 0.05, 0.10, and 0.20) catalysts.

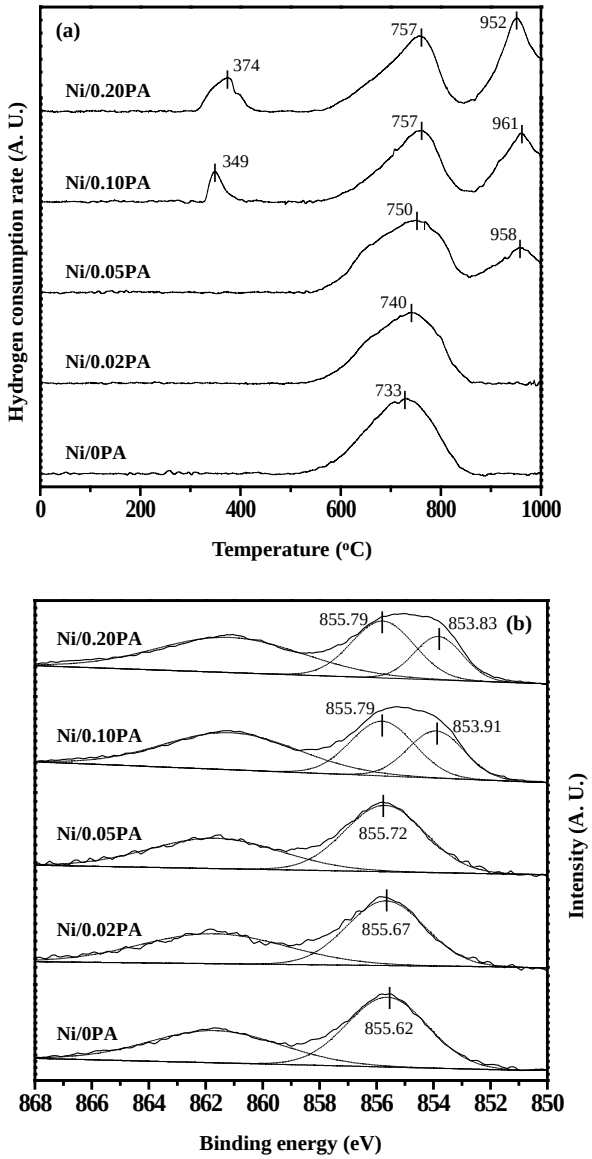

Fig. 3.21. (a) TPR profiles of calcined Ni/XPA (X = 0, 0.02, 0.05, 0.10, and 0.20) catalysts, and (b) XPS spectra in the Ni 2p level of calcined Ni/XPA (X = 0, 0.02, 0.05, 0.10, and 0.20) catalysts.

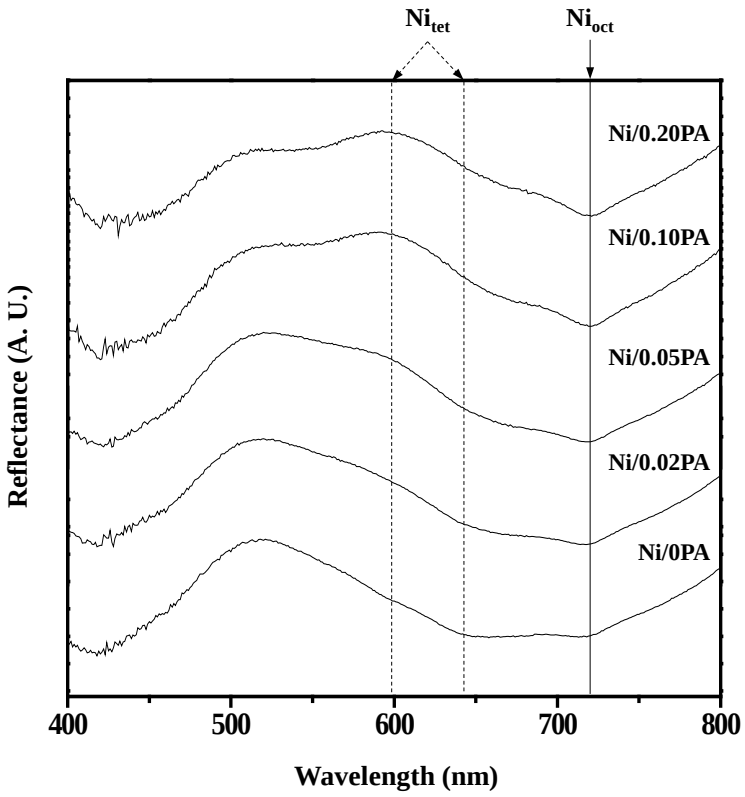

Fig. 3.22. UV-vis-DRS spectra of calcined Ni/XPA (X = 0, 0.02, 0.05, 0.10, and 0.20) catalysts.

3.3.3. Characterization of reduced catalysts

Crystalline phases of Ni/XPA (X = 0, 0.02, 0.05, 0.10, and 0.20) catalysts reduced at 700 ºC for 3 h were examined by XRD measurements. As shown in Fig. 3.23, all the reduced Ni/XPA catalysts retained metallic nickel phase (solid lines in Fig. 3.23). Diffraction peaks corresponding to nickel aluminate phase and nickel oxide phase were not detected in the XRD patterns. The diffraction peak of γ-Al_2O_3 (440) plane was also observed, indicating that the reduced Ni/XPA catalysts recovered original crystalline structure of calcined XPA supports by lattice contraction resulted from the release of nickel ions [66]. Thus, nickel species in the calcined Ni/XPA catalysts were completely reduced to metallic nickel phase during the reduction process employed in this work. Crystallite sizes of metallic nickel were also calculated as listed in Table 3.9. It was found that crystallite size of metallic nickel increased with increasing P/Al molar ratio in the reduced Ni/XPA catalysts. In particular, the reduced Ni/0.10PA and Ni/0.20PA catalysts showed a remarkable increment in the crystallite size of metallic nickel. It is generally accepted that nickel oxide phase rather than nickel aluminate phase is vulnerable to sintering at high temperature [91]. In consideration of XRD patterns of calcined Ni/XPA catalysts, therefore, it is believed that the increased amount of nickel oxide phase and the decreased amount of nickel aluminate phase with increasing P/Al molar ratio might be responsible for sintering of nickel species during the reduction process.

The trend of crystallite size of metallic nickel in the reduced Ni/XPA

catalysts (X = 0, 0.05, and 0.20) measured by XRD was also supported by TEM images. Fig. 3.24(a) shows well-dispersed nickel particles in the reduced Ni/0PA catalyst. The reduced Ni/0.05PA catalyst showed a similar size of nickel particles (Fig. 3.24(b)) compared to the reduced Ni/0PA catalyst. However, the reduced Ni/0.20PA catalyst (Fig. 3.24(c)) showed large nickel particles about 20 nm.

To make a detail comparison of nickel dispersion, H_2-TPD measurements for reduced Ni/XPA (X = 0, 0.02, 0.05, 0.10, and 0.20) catalysts were carried out as represented in Fig. 3.25. According to the literature [100], there are two hydrogen desorption regions; one (Type I) is attributed to hydrogen desorbed from the active metal species and the other (Type II) is related to hydrogen desorbed from subsurface layers or to spillover hydrogen. In order to distinguish these kinds of hydrogen in the H_2-TPD profiles of the reduced Ni/XPA catalysts, H_2-TPD profiles were deconvoluted into four bands with respect to desorption temperature; Type Ia (< 200 ^oC), Type Ib (200-400 ^oC), Type Ic (400-500 ^oC), and Type II (> 500 ^oC). The amount of hydrogen uptake by exposed nickel species of the catalysts was then calculated using deconvoluted peak area for Type I (Table 3.10). Total amount of hydrogen desorbed from the reduced Ni/XPA catalysts decreased with increasing P/Al molar ratio. This trend was in good agreement with the trend of crystallite size of metallic nickel. In addition, nickel surface area and nickel dispersion decreased with increasing P/Al molar ratio. This result implies the amount of exposed nickel species decreased with increasing P/Al molar ratio of reduced Ni/XPA catalysts.

It should be noted that there are some variations in distribution of

hydrogen-binding sites over the catalysts. Especially, the amount of strong hydrogen-binding sites showed a volcano-shaped trend with respect to P/Al molar ratio. Among the catalysts, Ni/0.05PA catalyst showed the largest amount of strong hydrogen-binding sites. This indicates that hydrogen molecules could be more strongly bound on the surface of nickel species in the reduced Ni/0.05PA catalyst compared to the other catalysts. In other words, nickel species in the reduced Ni/0.05PA catalyst was effective for stabilization of dissociated hydrogen atoms. It is believed that this is because nickel species in the reduced Ni/0.05PA catalyst are in the electronically favorable state for strong hydrogen-binding caused by high binding energy of nickel species in the XPA supports as evidenced in TPR and XPS results.

It has been reported that dissociative adsorption of methane on the surface of nickel species (equation 3.3) is a rate-determining step in the steam reforming of methane [87]. For this reason, it is expected that stabilization of methyl group and hydrogen atom on nickel surface is important for efficient methane reforming on the nickel catalysts. Therefore, the reduced Ni/0.05PA catalyst was considered to be the most efficient for dissociative methane adsorption in the steam reforming of LNG. This is further confirmed by CH_4-TPD measurements, as will be discussed in Section 3.3.4.

$$CH_4 + 2Ni^* \leftrightarrow CH_3\text{-}Ni^* + H\text{-}Ni^* \quad (3.3)$$

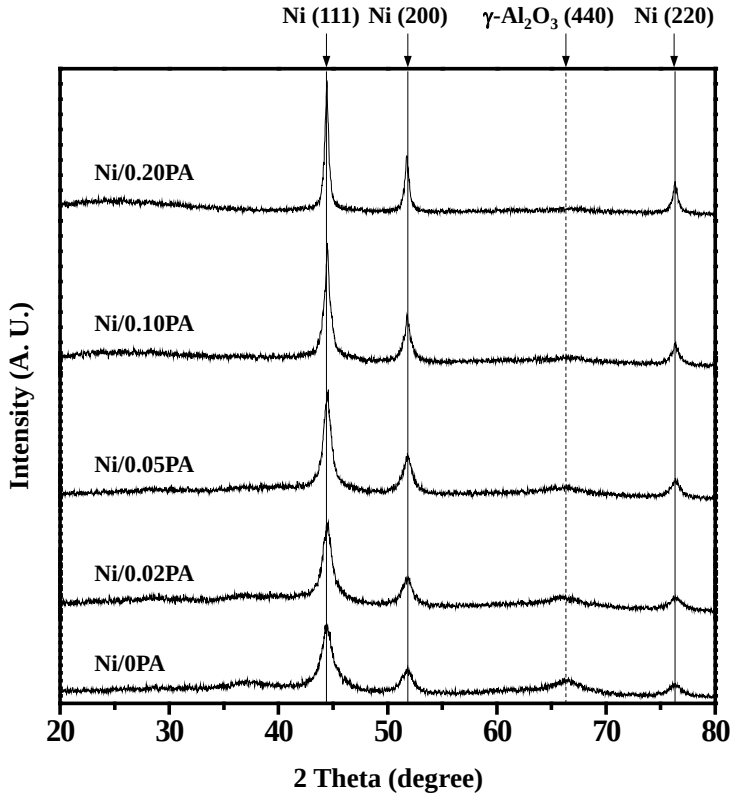

Fig. 3.23. XRD patterns of reduced Ni/XPA (X = 0, 0.02, 0.05, 0.10, and 0.20) catalysts.

Table 3.9

Crystallite sizes of metallic nickel in the reduced Ni/XPA catalysts

Catalyst	Crystallite size of metallic nickel (nm)[a]
Ni/0PA	8.8
Ni/0.02PA	9.0
Ni/0.05PA	9.5
Ni/0.10PA	14.5
Ni/0.20PA	18.6

[a] Calculated by the Scherrer equation from Ni (200) diffraction peak broadening in Fig. 3.23

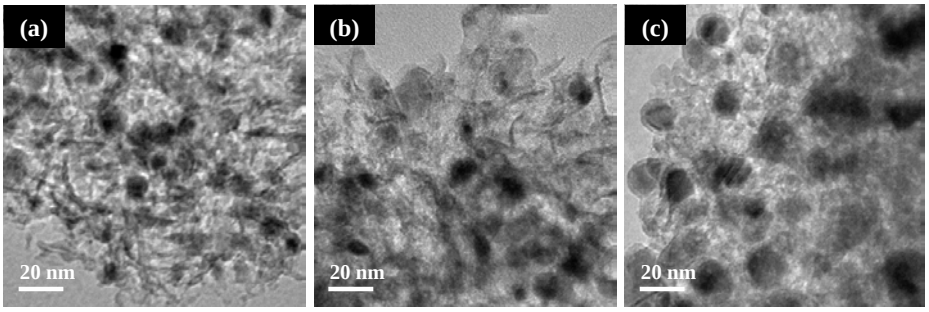

Fig. 3.24. TEM images of reduced (a) Ni/0PA, (b) Ni/0.05PA, and (c) Ni/0.20PA catalysts.

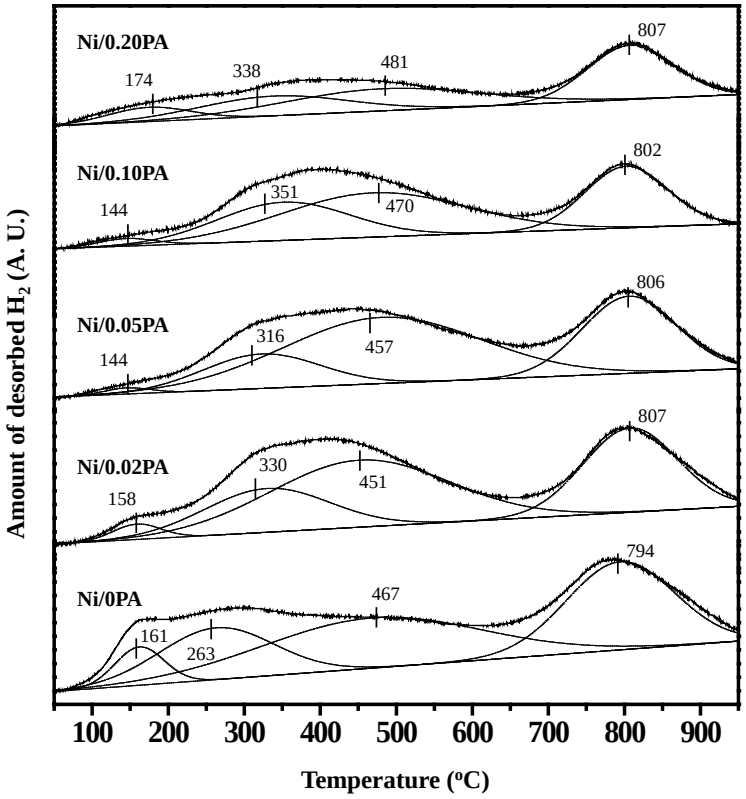

Fig. 3.25. H_2-TPD profiles of reduced Ni/XPA (X = 0, 0.02, 0.05, 0.10, and 0.20) catalysts.

Table 3.10

H_2-TPD results of reduced Ni/XPA catalysts

Catalyst	Amount of desorbed hydrogen (μmol-H_2/g)[a]				Nickel surface area (m^2/g-Ni)[b]	Nickel dispersion (%)[b]
	Weak site	Medium site	Strong site	Total		
Ni/0PA	9.4 (10.0%)[c]	29.8 (31.6%)	55.1 (58.4%)	94.3	44.2	6.6
Ni/0.02PA	3.7 (4.0%)	27.4 (30.1%)	60.1 (65.9%)	91.2	42.8	6.4
Ni/0.05PA	1.4 (1.6%)	20.3 (23.2%)	65.6 (75.2%)	87.3	40.9	6.2
Ni/0.10PA	1.8 (3.2%)	21.2 (36.8%)	34.5 (60.0%)	57.5	26.9	4.1
Ni/0.20PA	5.8 (13.8%)	14.7 (34.9%)	21.6 (51.3%)	42.1	19.7	3.0

[a] Calculated from deconvoluted peak area of H_2-TPD profiles in Fig. 3.25

[b] Calculated by assuming $H/Ni_{atom} = 1$

[c] Values in parentheses are percentage of each deconvoluted area in H_2-TPD profiles

3.3.4. Methane adsorption study on reduced catalysts

Methane (CH_4) is a major component of LNG which is a reactant in this study. Thus, CH_4-TPD measurements were carried out to explain the affinity of nickel species toward methane molecule and the trend of catalytic activities over Ni/XPA (X = 0, 0.02, 0.05, 0.10, and 0.20) catalysts. It is important to note that desorption of methane on nickel-alumina catalyst can be regarded as temperature-programmed oxidation (TPO) of carbon species originated from methane, because residual surface oxygen species on the catalyst act as an oxidant [101]. In this study, therefore, adsorbed carbon species can be oxidized into carbon monoxide and carbon dioxide, or hydrogenated into methane due to hydrogen flow during the TPD measurements. However, a signal for carbon monoxide (m/z = 28) was not detected while signals for carbon dioxide (m/z = 44), methane (m/z = 15), and water (m/z = 18) were detected from ion chromatogram acquired using a GC-MSD. Water is generated by hydrogenation of oxygen species on the reduced Ni/XPA catalysts. Therefore, we used signals for carbon dioxide and methane to calculate the amount of adsorbed methane on the reduced Ni/XPA catalysts. CHNS elemental analyses were further carried out after CH_4-TPD measurements to examine residual carbon species on the catalysts. Indeed, it was revealed that the amount of carbon species hydrogenated into methane or remained on the catalysts was negligible, when compared to the amount of carbon species oxidized into carbon dioxide. Thus, we assumed that all the carbon species adsorbed on the surface of reduced Ni/XPA catalysts were

oxidized into carbon dioxide. In other words, we assumed that the amount of carbon dioxide produced was identical to the amount of methane adsorbed on the surface of reduced Ni/XPA catalysts.

As presented in Fig. 3.26(a), a broad desorption band was observed in the CH_4-TPD profiles of reduced Ni/XPA (X = 0, 0.02, 0.05, 0.10, and 0.20) catalysts. The amount of adsorbed methane on the catalysts was calculated as listed in Table 3.11. It was found that the amount of adsorbed methane increased in the order of Ni/0.20PA < Ni/0.10PA < Ni/0PA < Ni/0.02PA < Ni/0.05PA. This trend was well matched with the trend of the absolute amount of strong hydrogen-binding sites listed in Table 3.11, suggesting that methane adsorption behavior was closely related to the stabilization of chemisorbed hydrogen species. Fig. 3.26(b) shows the relationship between the amount of adsorbed methane and the absolute amount of strong hydrogen-binding sites. The amount of adsorbed methane increased with increasing the amount of strong hydrogen-binding sites over the reduced Ni/XPA catalysts. Among the catalysts tested, Ni/0.05PA catalyst retaining the largest amount of strong hydrogen-binding sites exhibited the largest amount of adsorbed methane.

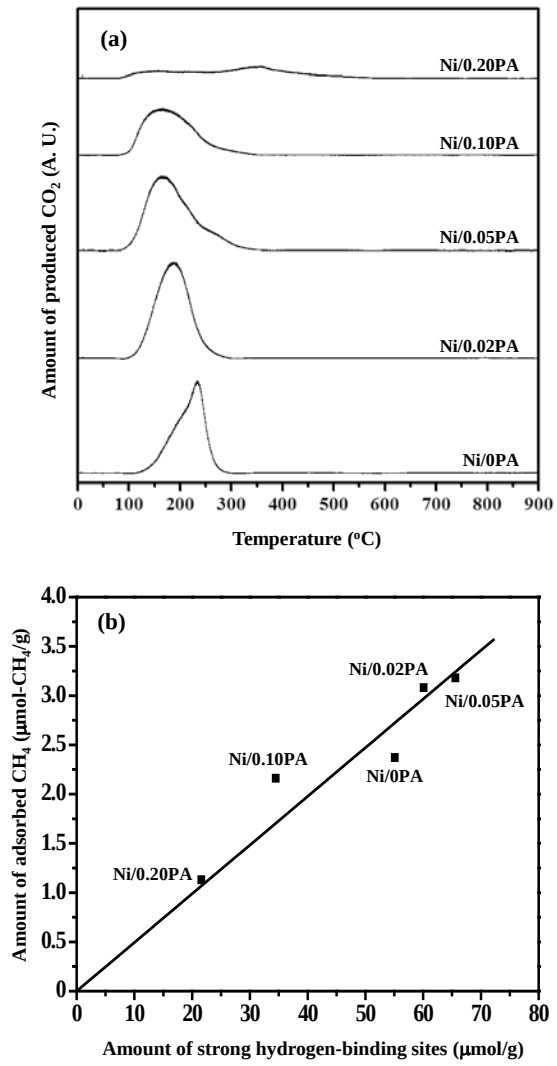

Fig. 3.26. (a) CH_4-TPD profiles of reduced Ni/XPA (X = 0, 0.02, 0.05, 0.10, and 0.20) catalysts and (b) a correlation between the amount of adsorbed CH_4 in CH_4-TPD measurements and the amount of strong hydrogen-binding sites in H_2-TPD measurements of reduced Ni/XPA (X = 0, 0.02, 0.05, 0.10, and 0.20) catalysts.

Table 3.11

Amount of adsorbed CH_4 on the reduced Ni/XPA catalysts

Catalyst	Amount of adsorbed CH_4 (μmol-CH_4/g)[a]
Ni/0PA	2.37
Ni/0.02PA	3.08
Ni/0.05PA	3.18
Ni/0.10PA	2.16
Ni/0.20PA	1.13

[a] Calculated from peak area of CH_4-TPD profiles in Fig. 3.26(a)

3.3.5. Catalytic performance in the steam reforming of LNG

LNG conversion and hydrogen yield with time of stream in the hydrogen production by steam reforming of LNG over Ni/XPA (X = 0, 0.02, 0.05, 0.10, and 0.20) catalysts are presented in Fig. 3.27. Ni/XPA (X = 0, 0.02, and 0.05) catalysts exhibited a stable catalytic performance during the steam reforming of LNG. Small crystallite size of metallic nickel, high nickel surface area, and large amount of strong hydrogen-binding sites of these catalysts played crucial roles for their excellent catalytic performance. However, Ni/0.10PA and Ni/0.20PA catalysts experienced a catalyst deactivation. In particular, Ni/0.20PA catalyst showed a severe catalyst deactivation during the reaction; 25% decrease of LNG conversion and 65% decrease of hydrogen yield. The catalyst deactivation of Ni/0.10PA and Ni/0.20PA catalysts were mainly due to nickel sintering during the reaction. It was previously revealed that Ni/0.10PA and Ni/0.20PA catalysts retained relatively large crystallite size of metallic nickel caused by weak metal-support interaction between nickel species and support. Thus, nickel species weakly bound to the support in the Ni/0.10PA and Ni/0.20PA catalysts are vulnerable to sintering during the reaction. Nickel sintering was quantitatively examined by XRD measurements for the used catalysts after a 1000 min-reaction (Fig. 3.28). The calculated crystallite size of metallic nickel in the used catalysts is listed in Table 3.12. Crystallite size of metallic nickel on the used Ni/XPA (X = 0, 0.02, 0.05, 0.10, and 0.20) catalysts was larger than that on the reduced catalysts (Table 3.9). In addition, the degree of sintering of

Ni/0.10PA and Ni/0.20PA catalysts was much higher than that of the other Ni/XPA catalysts. The amount of carbon deposition in the used catalysts is listed in Table 3.13. It is noticeable that the amount of carbon deposition decreased with increasing P/Al molar ratio of the catalysts. This might be due to the basic nature of phosphorus species which served as an electron donor as reported in the literature [102]. From these results, it is believed that nickel sintering rather than carbon deposition was a main factor for catalyst deactivation of Ni/0.10PA and Ni/0.20PA catalysts during the steam reforming reaction.

Fig. 3.29(a) shows the initial LNG conversion and initial hydrogen yield over Ni/XPA (X = 0, 0.02, 0.05, 0.10, and 0.20) catalysts in the steam reforming of LNG plotted as a function of P/Al molar ratio. Initial LNG conversion and initial hydrogen yield exhibited volcano-shaped curves with respect to the P/Al molar ratio. This indicates that an optimal P/Al molar ratio was required for maximum hydrogen production by steam reforming of LNG over Ni/XPA catalysts. These catalytic performance data were also well correlated with the amount of adsorbed methane which was related to the affinity toward methane of Ni/XPA catalysts, as presented in Fig. 3.29(b). As the amount of adsorbed methane increased, LNG conversion and hydrogen yield over Ni/XPA catalysts increased. In other words, catalytic performance of Ni/XPA catalysts was enhanced with increasing the amount of active sites available for methane adsorption. Among the catalysts tested, Ni/0.05PA catalyst with the highest affinity toward methane served as the most efficient catalyst in the hydrogen production by steam reforming of LNG.

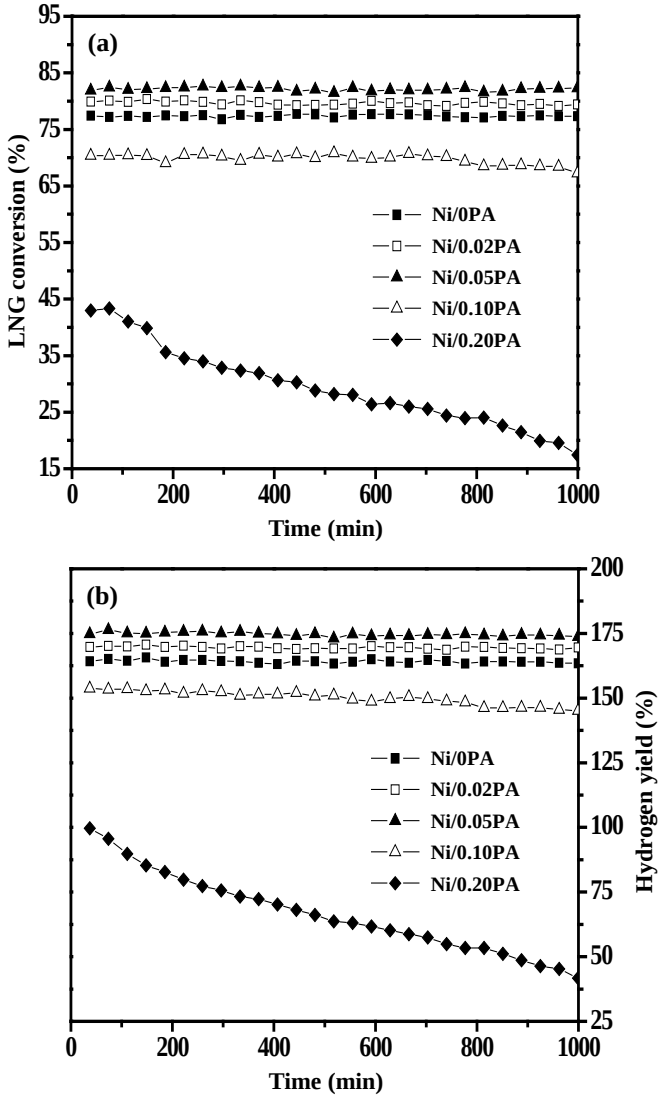

Fig. 3.27. (a) LNG conversion and (b) hydrogen yield with time on stream in the steam reforming of LNG over Ni/XPA (X = 0, 0.02, 0.05, 0.10, and 0.20) catalysts at 600 ºC.

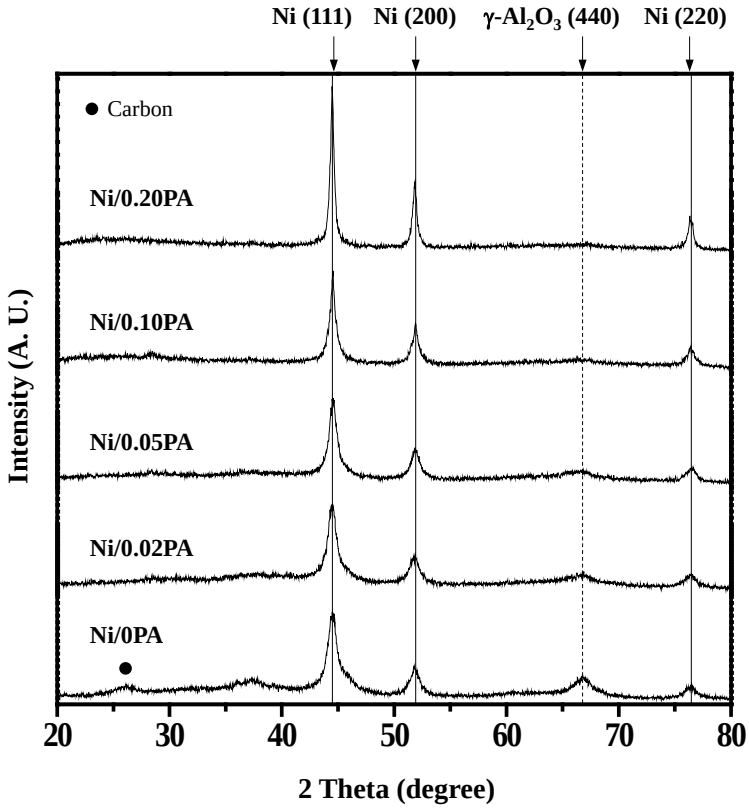

Fig. 3.28. XRD patterns of used Ni/XPA (X = 0, 0.02, 0.05, 0.10, and 0.20) catalysts.

Table 3.12

Crystallite sizes of metallic nickel and degree of sintering of the used Ni/XPA catalysts after a 1000 min-reaction

Catalyst	Crystallite size of metallic nickel (nm)[a]	Degree of sintering (%)[b]
Ni/0PA	9.0	2.6
Ni/0.02PA	9.2	3.0
Ni/0.05PA	10.0	4.9
Ni/0.10PA	16.4	12.9
Ni/0.20PA	22.2	19.3

[a] Calculated by the Scherrer equation from Ni (200) diffraction peak broadening in Fig. 3.28

[b] Calculated by following equation:

$$Degree\ of\ \ sintering\ (\%) = \frac{Crystallite\ size\ of\ \ metallic\ nickel\ after\ reaction\ (nm)}{Crystallite\ size\ of\ \ metallic\ nickel\ after\ reduction\ (nm)} \times 100$$

Table 3.13

Amount of carbon deposition in the used Ni/XPA catalysts after a 1000 min-reaction

Catalyst	Amount of carbon deposition (wt%)[a]
Ni/0PA	7.8
Ni/0.02PA	0.5
Ni/0.05PA	0.2
Ni/0.10PA	0.1
Ni/0.20PA	-

[a] Determined by CHNS elemental analysis

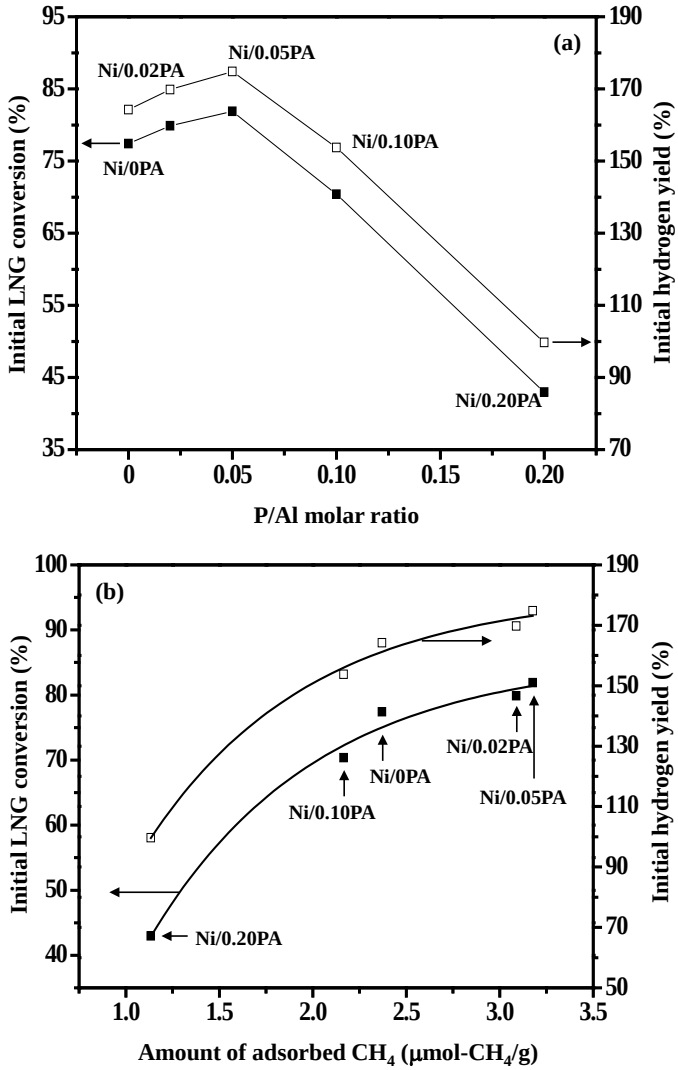

Fig. 3.29. (a) Correlations between initial catalytic performance and P/Al molar ratio of Ni/XPA (X = 0, 0.02, 0.05, 0.10, and 0.20) catalysts and (b) correlations between initial catalytic performance and the amount of adsorbed CH_4 calculated in the CH_4-TPD profiles of Ni/XPA (X = 0, 0.02, 0.05, 0.10, and 0.20) catalysts.

3.4. Mesoporous nickel-phosphorus-alumina xerogel and aerogel catalysts

3.4.1. Textural properties of calcined catalysts

Textural properties of NPAX and NPAA catalysts calcined at 700 ^{o}C for 5 h were examined by nitrogen adsorption-desorption measurements as shown in Fig. 3.30. IV-type isotherms, which were related to capillary condensation in a well-developed mesoporous structure, were obtained in the nitrogen adsorption-desorption measurements of NPAX and NPAA catalysts. However, both catalysts showed different hysteresis loops in the isotherms. NPAX catalyst exhibited a H2-type hysteresis loop indicative of ink bottle-shaped pore structure, while NPAA catalyst showed a H1-type hysteresis loop ascribed to mesoporous network caused by nearly spherical primary agglomerates [78], implying that drying method played an important role in determining pore structure.

Both catalysts retained excellent textural properties and mesoporous features even after high temperature calcination process (Table 3.14). It is interesting to note that NPAA catalyst exhibited larger surface area, larger pore volume, and larger average pore diameter than NPAX catalyst, although chemical compositions of the catalysts were nearly identical. This result indicates that supercritical CO_2 drying method was effective for suppressing rapid collapse of gel structure by removing residual liquid molecules confined in gel network smoothly in the preparation of NPAA catalyst.

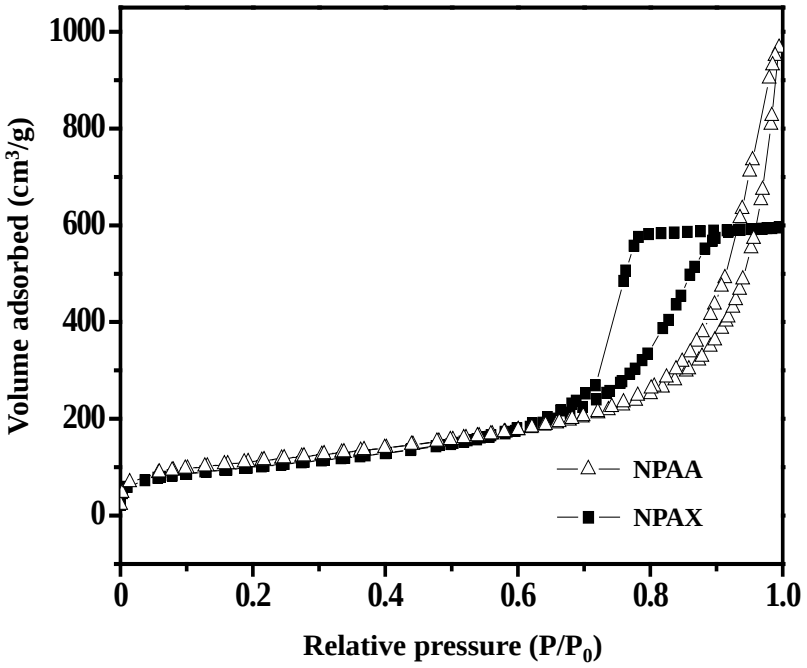

Fig. 3.30. Nitrogen adsorption-desorption isotherms of calcined NPAX and NPAA catalysts.

Table 3.14

Textural properties calcined NPAX and NPAA catalysts

Catalyst	NPAX	NPAA
P/Al molar ratio[a]	0.05	0.05
Ni/(P+Al) molar ratio[a]	0.14	0.14
Surface area (m^2/g)[b]	358	400
Pore volume (cm^3/g)[c]	0.92	1.41
Average pore diameter (nm)	10.3	14.1

[a] Determined by ICP-AES measurement

[b] Calculated by the BET equation

[c] Total pore volume at $P/P_0 \sim 0.995$

3.4.2. Crystalline structure of calcined catalysts

Fig. 3.31(a) shows XRD patterns of calcined NPAX and NPAA catalysts. Both catalysts exhibited diffraction peaks corresponding to γ-Al_2O_3 phase and nickel aluminate phase, implying that nickel ions were incorporated into the crystalline structure of γ-Al_2O_3 phase by forming strong interaction between nickel and aluminum species. A close examination also revealed that intensities of diffraction peaks for NPAA catalyst were weaker than those for NPAX catalyst, demonstrating that nickel species in the form of nickel aluminate phase were more finely dispersed in the NPAA catalyst than those in the NPAX catalyst.

Reducibility of NPAX and NPAA catalysts were examined by H_2-TPR measurements as presented in Fig. 3.31(b). Both catalysts showed two reduction peaks at 698-728 ^oC and 944-948 ^oC; the former was attributed to the reduction of nickel species in the form of surface nickel aluminate phase, while the latter was attributed to the reduction of phosphorus species interacting with oxygen [95,103,104]. Thus, it is expected that nickel species in the catalysts retained high stability for sintering during the reduction process due to the aluminate nature [91]. It should be noted that the reduction peak temperature of nickel species in the NPAA catalyst was higher than that in the NPAX catalyst. This means metal-support interaction between nickel species and phosphorus-containing alumina in the NPAA catalyst was stronger than that in the NPAX catalyst.

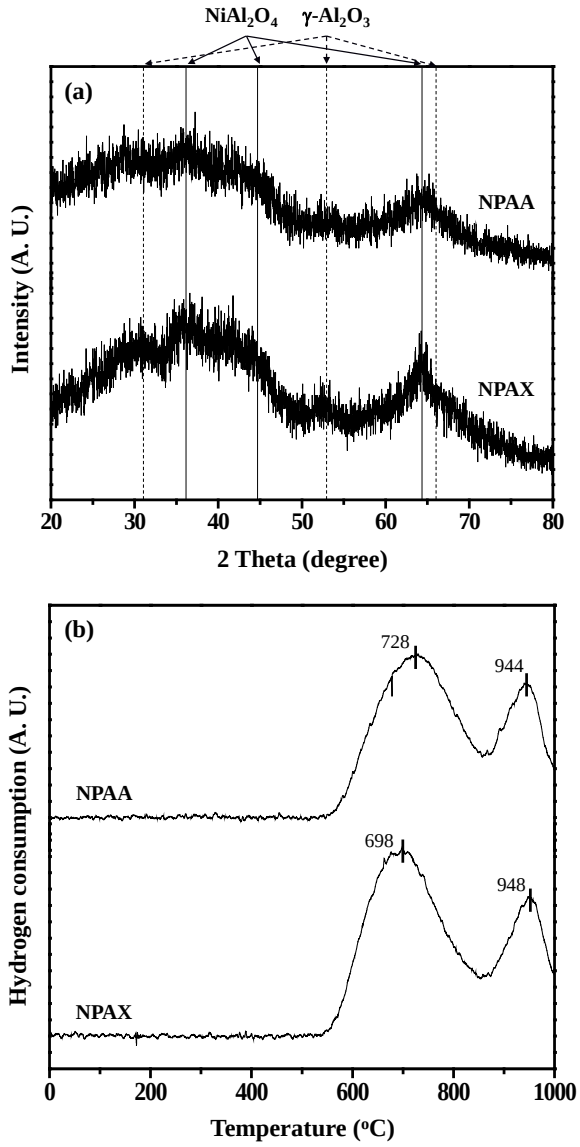

Fig. 3.31. (a) XRD patterns and (b) TPR profiles of calcined NPAX and NPAA catalysts.

3.4.3. Characterization of reduced catalysts

Crystalline structures of NPAX and NPAA catalysts reduced at 700 ºC for 3 h were examined by XRD measurements as presented in Fig. 3.32(a). Both reduced catalysts showed γ-Al_2O_3 (440) plane (dashed line in Fig. 3.32(a)) and metallic nickel phase (solid lines in Fig. 3.32(a)). No diffraction peaks corresponding to nickel aluminate phase and bulk nickel oxide phase were observed in the XRD patterns. This means that nickel species in the calcined NPAX and NPAA catalysts were completely reduced into metallic nickel during the reduction process. It was also found that XRD signals for metallic nickel phase in the reduced NPAX catalyst were sharper than those in the reduced NPAA catalyst. This means NPAA catalyst retained smaller metallic nickel crystallite than NPAX catalyst after the reduction process. This might be due to the fact that NPAA catalyst retained stronger metal-support interaction than NPAX catalyst as discussed in the TPR result. In other words, NPAA catalyst exhibited stronger resistance toward nickel sintering than NPAX catalyst. This was further confirmed by TEM images of reduced NPAX and NPAA catalysts. The reduced NPAX catalyst (Fig. 3.32(b)) retained relatively large aggregates of nickel particles compared to the reduced NPAA catalyst (Fig. 3.32(c)), although both reduced catalysts showed small nickel particles less than 20 nm. That is, nickel dispersion on the reduced NPAA catalyst was higher than that on the reduced NPAX catalyst.

For quantitative comparison of nickel dispersion on the reduced NPAX and NPAA catalysts, H_2-TPD measurements were carried out. Fig. 3.33 shows

the H_2-TPD profiles of reduced NPAX and NPAA catalysts. According to the previous study [100], hydrogen molecules desorbed above 650 ^oC in Fig. 3.33 can be assigned to spillover hydrogen on support or hydrogen desorbed from subsurface layers. In this work, therefore, only hydrogen desorption bands appearing below 650 ^oC are related to desorption process from the active nickel species. H_2-TPD profiles of the reduced catalysts were deconvoluted in order to classify the identity of hydrogen with respect to desorption peak temperature; weak site (< 200 ^oC), medium site (200-400 ^oC), and strong site (400-500 ^oC). Deconvolution results for H_2-TPD profiles of the reduced catalysts are summarized in Table 3.15. It was found that total amount of desorbed hydrogen from the reduced NPAA catalyst was larger than that from the reduced NPAX catalyst. This indicates that the reduced NPAA catalyst exhibited high nickel surface area and small average nickel diameter compared to the reduced NPAX catalyst. These results strongly suggest that the amount of exposed active nickel sites for steam reforming reaction on the reduced NPAA catalyst was larger than that on the reduced NPAX catalyst. Furthermore, it is interesting to note that the reduced NPAA catalyst retained larger amount of strong hydrogen-binding sites than the reduced NPAX catalyst, implying that the reduced NPAA catalyst was more favorable for stabilizing dissociated hydrogen species than the reduced NPAX catalyst. This result might be due to the fact that NPAA catalyst exhibited strong metal-support interaction between nickel species and support, resulting in an electronically favorable state of nickel for hydrogen-binding.

It is well known that the rate-determining step for steam reforming of methane is dissociative adsorption of methane ($CH_4 + 2Ni^* \leftrightarrow CH_3\text{-}Ni^* + H\text{-}$

Ni*) [87]. Thus, stabilization of methyl group and hydrogen atom derived from methane is an important factor determining the catalytic performance of nickel catalyst in the reaction. As discussed above, the reduced NPAA catalyst retained high nickel dispersion and much amount of strong hydrogen-binding sites compared to the reduced NPAX catalyst. This implies that the reduced NPAA catalyst is expected to exhibit higher affinity toward methane than the reduced NPAX catalyst.

In order to verify the amount of adsorbed methane on the surface of reduced catalysts, CH_4-TPD measurements were conducted as presented in Fig. 3.34. A broad band at 210 ^oC was detected in the CH_4-TPD profiles of the reduced catalysts. The amounts of adsorbed methane on the reduced catalysts calculated from the peak area in CH_4-TPD profiles are listed in Table 3.16. It was found that the reduced NPAA catalyst showed larger amount of adsorbed methane than the reduced NPAX catalyst. This suggests that the reduced NPAA catalyst retained large amount of effective methane adsorption sites for steam reforming of LNG compared to the reduced NPAX catalyst.

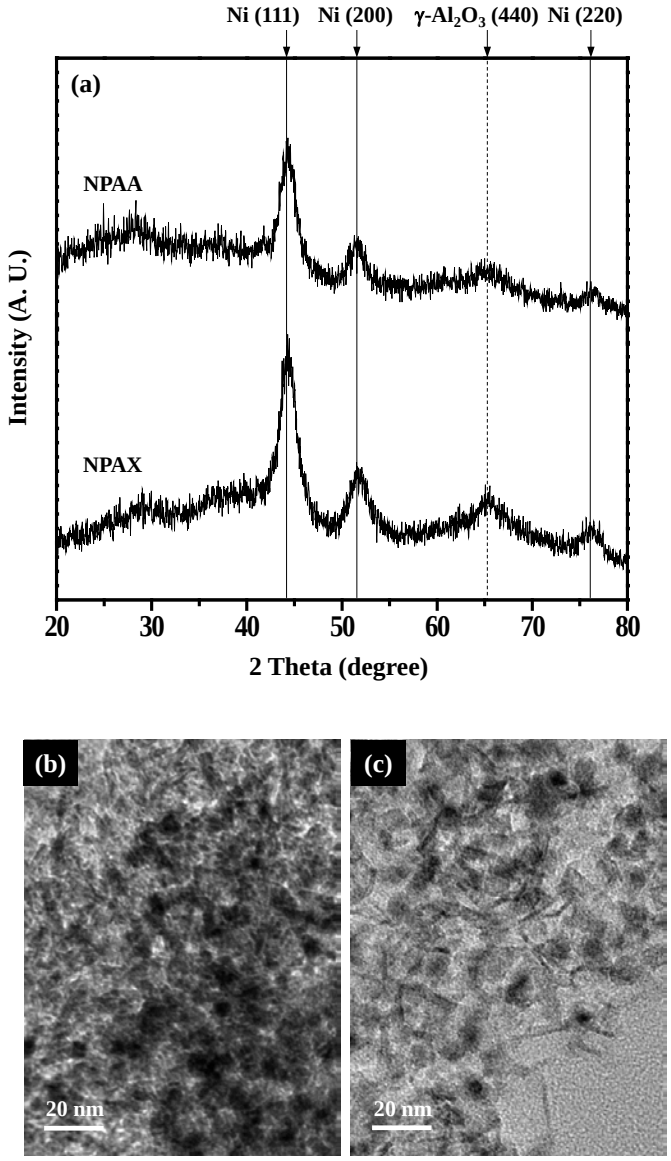

Fig. 3.32. (a) XRD patterns of reduced NPAX and NPAA catalysts, TEM images of reduced (b) NPAX and (c) NPAA catalysts.

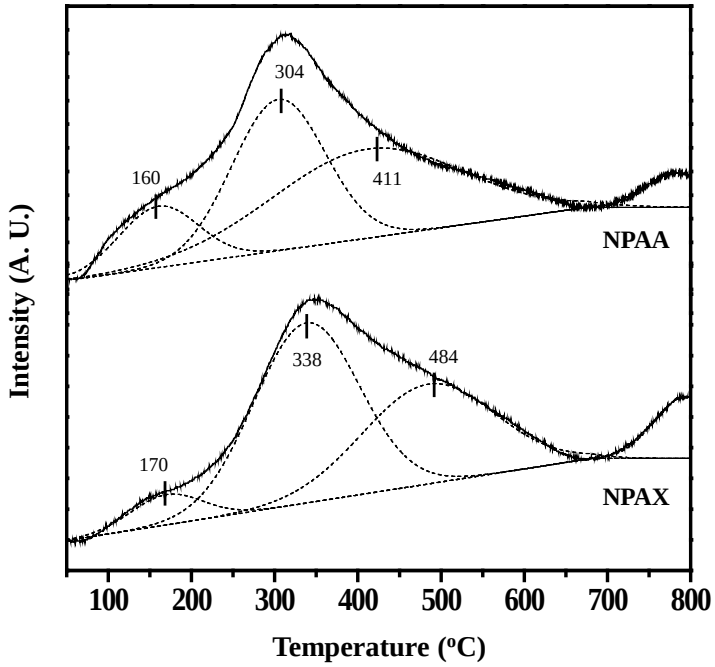

Fig. 3.33. H_2-TPD profiles of reduced NPAX and NPAA catalysts.

Table 3.15

H_2-TPD results of reduced NPAX and NPAA catalysts

Catalyst	Amount of desorbed hydrogen (μmol-H_2/g)[a]				Nickel surface area (m^2/g-Ni)[b]	Average nickel diameter (nm)
	Weak site	Medium site	Strong site	Total		
NPAX	8.9 (6.3%)[c]	77.6 (55.2%)	54.0 (38.5%)	140.5	65.8	10.2
NPAA	25.7 (13.5%)	74.8 (39.3%)	89.7 (47.2%)	190.2	89.1	7.6

[a] Calculated from deconvoluted peak area of H_2-TPD profiles in Fig. 3.33

[b] Calculated by assuming $H/Ni_{atom} = 1$

[c] Values in parentheses are percentage of each deconvoluted area in H_2-TPD profiles

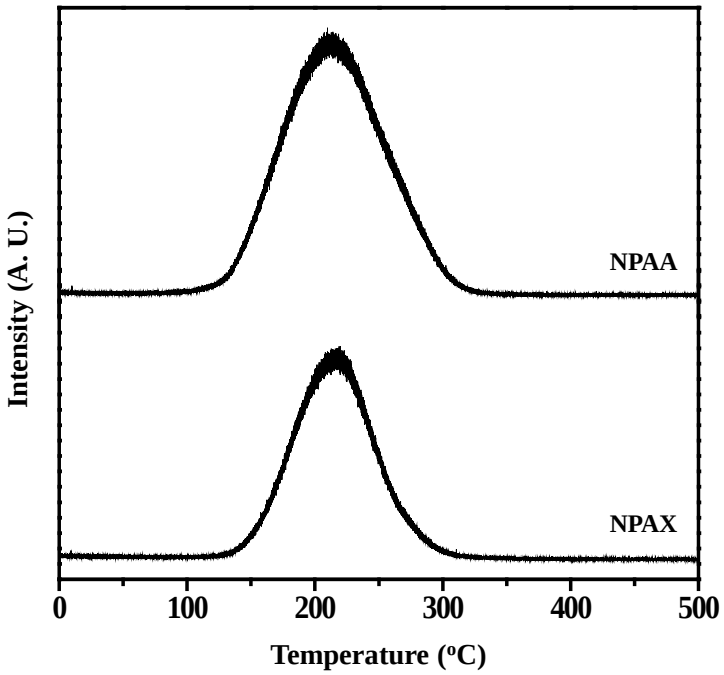

Fig. 3.34. CH_4-TPD profiles of reduced NPAX and NPAA catalysts.

Table 3.16

Amount of adsorbed CH_4 on the reduced NPAX and NPAA catalysts

Catalyst	Amount of adsorbed CH_4 (μmol-CH_4/g)[a]
NPAX	3.5
NPAA	5.5

[a] Calculated from peak area of CH_4-TPD profiles in Fig. 3.34

3.4.4. Catalytic performance in the steam reforming of LNG

Fig. 3.35 shows the catalytic performance (LNG conversion and hydrogen yield) with reaction time in the hydrogen production by steam reforming of LNG over NPAX and NPAA catalysts at 550 ^{o}C. Both catalysts showed a stable catalytic performance without noticeable catalyst deactivation during the 16 h-reaction. The stable catalytic performance of the catalysts was due to well-dispersed nickel species on the catalyst surface and strong metal-support interaction. Excellent textural properties of the catalysts were also believed to play an important role in promoting efficient mass transfer of reactant molecules during the reaction. CHNS elemental analyses (Table 3.17) revealed that both catalysts retained small amount of carbon deposition less than 3 wt% after a 16 h-reaction, representing that both NPAX and NPAA catalysts were tolerant toward carbon deposition and effective for gasification of surface carbon species.

It was found that NPAA catalyst was more active than NPAX catalyst in the steam reforming of LNG. High affinity toward methane, which was due to high nickel dispersion and abundant strong hydrogen-binding sites, was believed to be a main reason for high catalytic performance of NPAA catalyst. In conclusion, NPAA catalyst with large amount of effective methane adsorption sites served as an efficient catalyst in the hydrogen production by steam reforming of LNG.

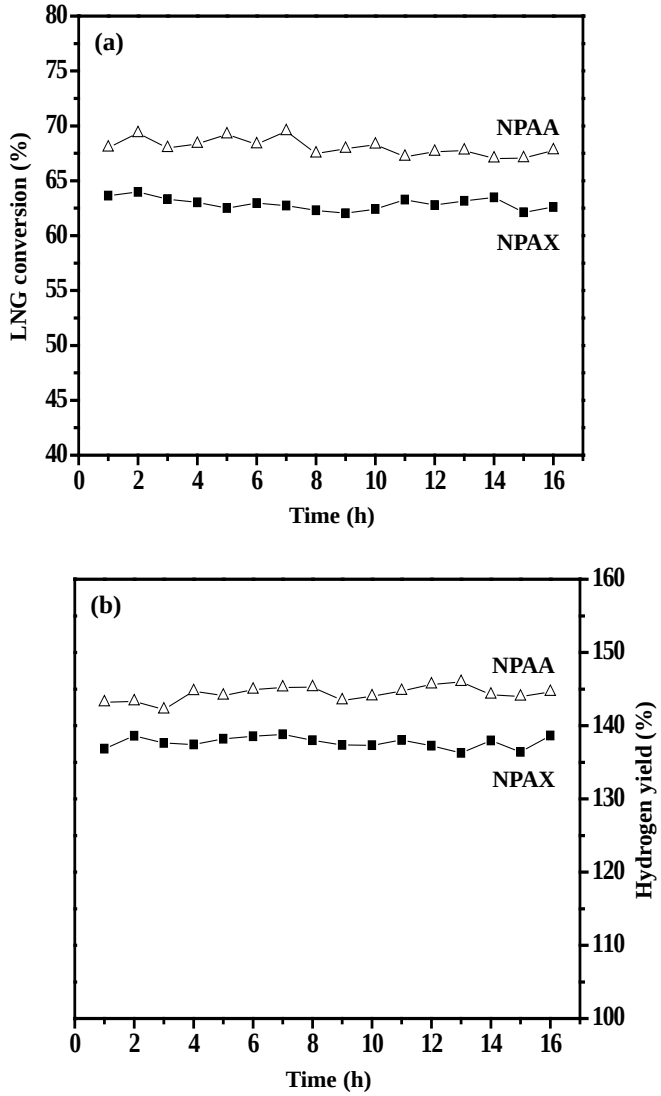

Fig. 3.35. (a) LNG conversion and (b) hydrogen yield with time on stream in the steam reforming of LNG over NPAX and NPAA catalysts at 550 °C.

Table 3.17

Amount of carbon deposition on the used NPAX and NPAA catalysts after a 16 h-reaction

Catalyst	Amount of carbon deposition (wt%)[a]
NPAX	2.5
NPAA	1.4

[a] Determined by CHNS elemental analysis

3.5. Ordered mesoporous nickel-alumina catalyst

3.5.1. Textural properties of calcined catalysts

Fig. 3.36 shows the nitrogen adsorption-desorption isotherms of support (OMA) and catalysts (Ni/OMA and OMNA). All the samples showed a typical IV-type isotherm, indicating the well-developed mesoporous structure [78]. It is interesting to note that the isotherm of OMA support and OMNA catalyst exhibited a narrower and steeper hysteresis loop, which was characteristics of cylindrical mesopores, than that of Ni/OMA catalyst [105]. Furthermore, desorption branch of Ni/OMA catalyst rapidly decreased at low relative pressure ($P/P_0 \approx 0.45$), representing a large H2-type hysteresis loop. This indicates that cage-like mesopores or constricted mesopores with small pore diameter were mainly formed in the Ni/OMA catalyst [75].

Detailed textural properties of support (OMA) and catalysts (Ni/OMA and OMNA) are listed in Table 3.18. All the samples exhibited high surface area, large pore volume, and large average pore diameter. It should be noted that Ni/OMA catalyst retained lower surface area, pore volume, and average pore diameter than OMNA catalyst, even though Ni/Al atomic ratio in both catalysts was identical. This means that mesopores in the OMA support were significantly blocked by the nickel species during the impregnation step. On the other hand, OMNA catalyst showed comparable textural properties to OMA support. This is because nickel precursor (nickel nitrate hexahydrate) used in the preparation of OMNA catalyst acted as a swelling agent by

increasing micelle size of triblock copolymer. It has been reported that micelle size of triblock copolymer increases with increasing concentration of nitrate ions in solution, due to the salting-in effect caused by nitrate ions adsorbed in EO blocks of triblock copolymer [106]. In addition, crystallograpic water molecules separated from nickel precursor in the preparation of OMNA catalyst are also responsible for swelling of hydrophilic block [107].

TEM images and SAXS patterns of calcined support (OMA) and catalysts (Ni/OMA and OMNA) are presented in Fig. 3.37. All the calcined samples retained an ordered unidimensional rod-like mesoporous structure. Furthermore, all the calcined samples exhibited a (100) diffraction peak around ca. $2\theta = 1.0^{o}$ in the SAXS patterns (Fig. 3.37(d)), indicating the successful formation of ordered structures. In particular, Ni/OMA catalyst (Fig. 3.37(b)) exhibited relatively non-uniform mesoporous channels compared to OMA support (Fig. 3.37(a)) and OMNA catalyst (Fig. 3.37(c)). This might be because original mesoporous structure of OMA support was collapsed by the addition of nickel precursor in the preparation of Ni/OMA catalyst. In addition, several particles were observed in the mesoporous network of Ni/OMA catalyst (Fig. 3.37(b)). These particles corresponded to bulk nickel oxides which were not incorporated into alumina lattice and aggregated during the impregnation step. This result indicates that nickel species in the OMNA catalyst were more finely dispersed than those in the Ni/OMA catalyst.

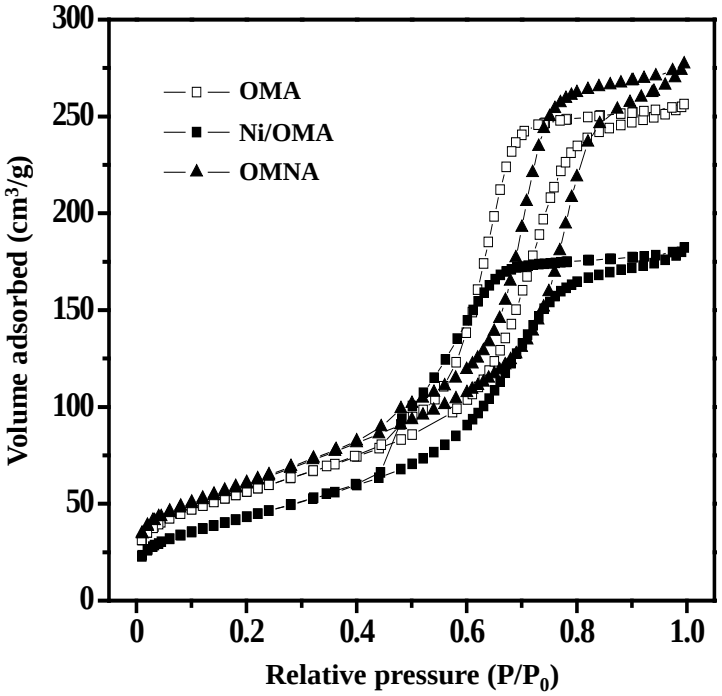

Fig. 3.36. Nitrogen adsorption-desorption isotherms of calcined support (OMA) and catalysts (Ni/OMA and OMNA).

Table 3.18

Textural properties of calcined support (OMA) and catalysts (Ni/OMA and OMNA)

Sample	OMA	Ni/OMA	OMNA
Ni/Al atomic ratio[a]	-	0.17	0.17
Surface area (m^2/g)[b]	205	163	223
Pore volume (cm^3/g)[c]	0.40	0.28	0.43
Average pore diameter (nm)	5.3	4.3	6.1

[a] Determined by ICP-AES measurement

[b] Calculated by the BET equation

[c] BJH desorption pore volume

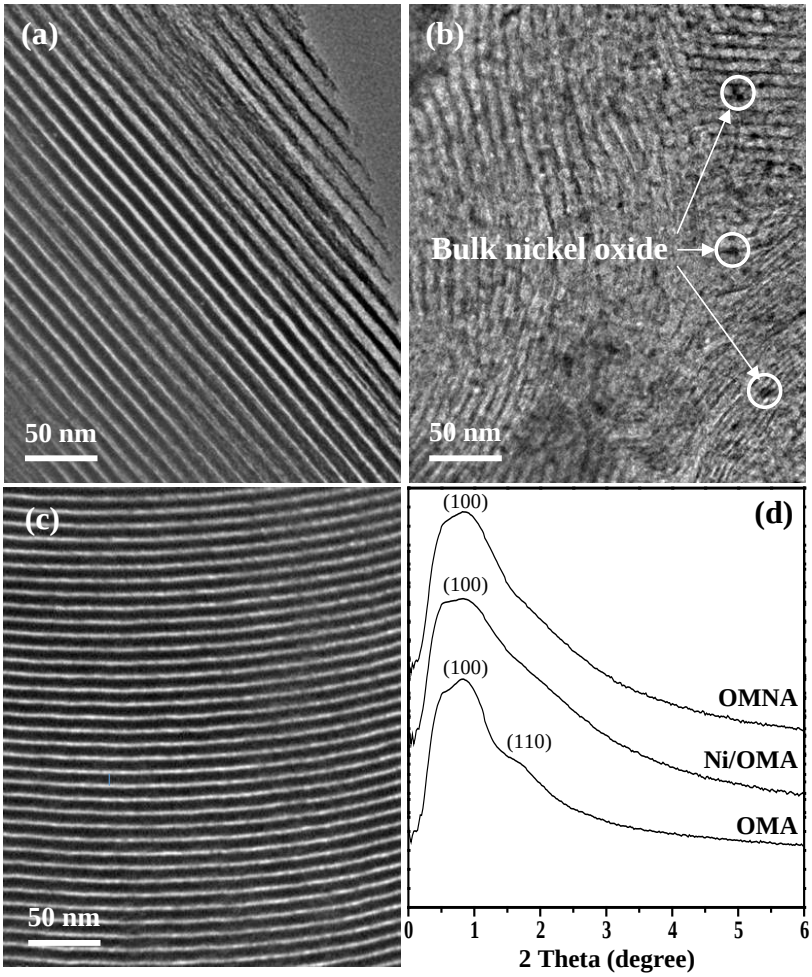

Fig. 3.37. TEM images of calcined (a) OMA support, (b) Ni/OMA catalyst, (c) OMNA catalyst, and (d) SAXS patterns of calcined support (OMA) and catalysts (Ni/OMA and OMNA).

3.5.2. Crystalline structure of calcined catalysts

Crystalline structures of calcined support (OMA) and catalysts (Ni/OMA and OMNA) were investigated by XRD measurements as shown in Fig. 3.38(a). It is known that γ-Al_2O_3 phase is readily formed within the temperature range of 500-800 ^oC and γ-Al_2O_3 is thermally stable within this temperature range [88]. Thus, it is inferred that both Ni/OMA and OMNA catalysts retained a thermally stable γ-Al_2O_3 phase interacting with nickel species. OMNA catalyst exhibited three distinct peaks corresponding to nickel aluminate phase (closed circles in Fig. 3.38(a)). On the other hand, Ni/OMA catalyst showed not only diffraction peaks corresponding to nickel aluminate phase (closed circles in Fig. 3.38(a)) but also diffraction peaks corresponding to bulk nickel oxide phase (solid lines in Fig. 3.38(a)). This means that nickel species in the Ni/OMA catalyst were poorly dispersed in the alumina lattice compared to those in the OMNA catalyst, as also shown in TEM image (Fig. 3.37(b)). Interestingly, the diffraction peaks of γ-Al_2O_3 (440) (dashed line in Fig. 3.38(a)) shifted to a lower diffraction angle in both catalysts, representing that γ-Al_2O_3 lattice was expanded by incorporation of Ni^{2+} ions into cationic deficient sites of the lattice [80]. A close examination revealed that the diffraction peak of γ-Al_2O_3 (440) in the OMNA catalyst shifted to lower diffraction angle ($2\theta = 65.1^o$) than that in the Ni/OMA catalyst ($2\theta = 65.7^o$). This result can be explained by the fact that finely dispersed nickel species in the OMNA catalyst more intimately contacted with γ-Al_2O_3 lattice, forming a more nickel-saturated surface nickel aluminate phase than those in the

Ni/OMA catalyst.

Fig. 3.38(b) shows the TPR profiles of Ni/OMA and OMNA catalysts calcined at 700 ^{o}C. OMNA catalyst exhibited a single reduction band at 697 ^{o}C, which was attributed to the reduction of surface nickel aluminate phase [108]. On the other hand, Ni/OMA catalyst showed two reduction bands at 342 ^{o}C and 734 ^{o}C. The reduction band appearing at 342 ^{o}C in the Ni/OMA catalyst was due to the reduction of bulk nickel oxide phase, while the reduction band appearing at 734 ^{o}C corresponded to the reduction of surface nickel aluminate phase [108]. Although bulk nickel oxide phase in the Ni/OMA catalyst can be readily reduced at low temperature, they are vulnerable to sintering during the reduction process. However, nickel species in the form of surface nickel aluminate phase in both Ni/OMA and OMNA catalysts would be more stable at high temperature than those in the form of bulk nickel oxide phase due to the aluminate nature [109].

It is noteworthy that reduction peak temperature of OMNA catalyst was lower than that of Ni/OMA catalyst. Considering the fact that the single-step preparation method of the catalyst was more effective for the formation of finely dispersed nickel species in the alumina support than the impregnation method [109], it is expected that OMNA catalyst retained more nickel-saturated surface nickel aluminate phase than Ni/OMA catalyst. According to the previous studies [42,96], surface nickel aluminate phase with a high degree of nickel-saturation is more reducible than that with a low degree of nickel-saturation. This is because reduction of nickel species is favorable when nickel species are surrounded by less aluminum species which act as electron deficient sites.

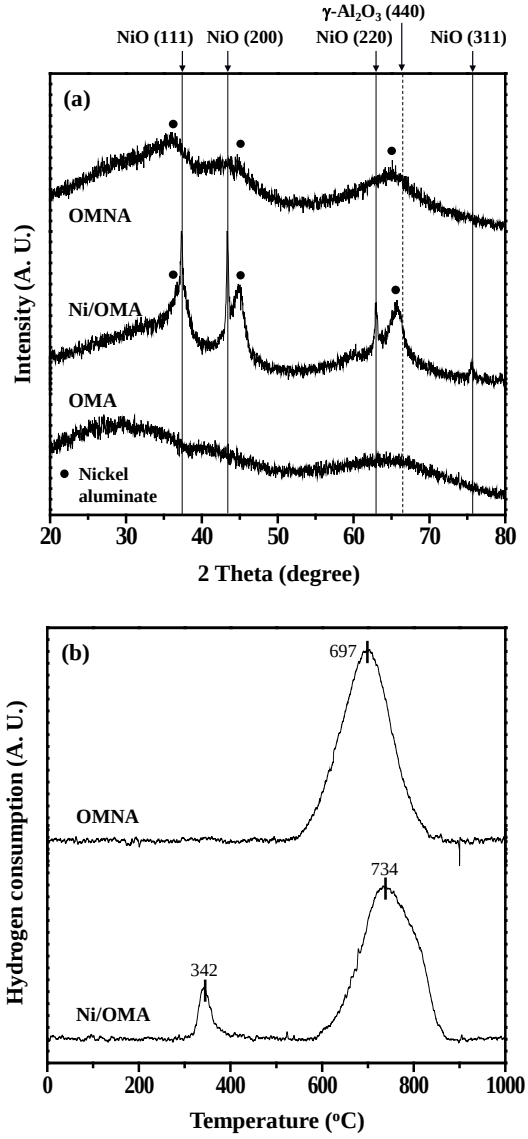

Fig. 3.38. (a) XRD patterns and (b) TPR profiles of calcined samples.

3.5.3. Characterization of reduced catalysts

XRD patterns of Ni/OMA and OMNA catalysts reduced at 700 ^{o}C are presented in Fig. 3.39(a). It was observed that the diffraction peak of γ-Al_2O_3 (440) (dashed line in Fig. 3.39(a)) moved back to the original diffraction angle in the reduced Ni/OMA and OMNA catalysts when compared to the diffraction peak in the calcined catalysts (Fig. 3.38(a)). Furthermore, neither nickel aluminate phase nor bulk nickel oxide phase was detected in both reduced catalysts. This means that nickel species in both catalysts were successfully reduced into metallic nickel.

Crystallite size of metallic nickel in the reduced Ni/OMA and OMNA catalysts was calculated by the Scherrer equation, as listed in Table 3.19. Crystallite size of metallic nickel in the reduced OMNA catalyst was smaller than that in the reduced Ni/OMA catalyst. This implies that the reduced OMNA catalyst retained larger amount of surface active sites than the reduced Ni/OMA catalyst. In other words, finely dispersed nickel species in the OMNA catalyst were less aggregated than those in the Ni/OMA catalyst during the reduction process, because metallic nickels were strongly confined in the mesopore of OMNA catalyst.

TEM analyses were also conducted to compare the crystallite size of metallic nickel in the reduced Ni/OMA and OMNA catalysts. Fig. 3.39(b) shows that relatively large aggregates of nickel species were formed in the reduced Ni/OMA catalyst. On the other hand, the reduced OMNA catalyst exhibited finely dispersed small nickel particles (Fig. 3.39(c)).

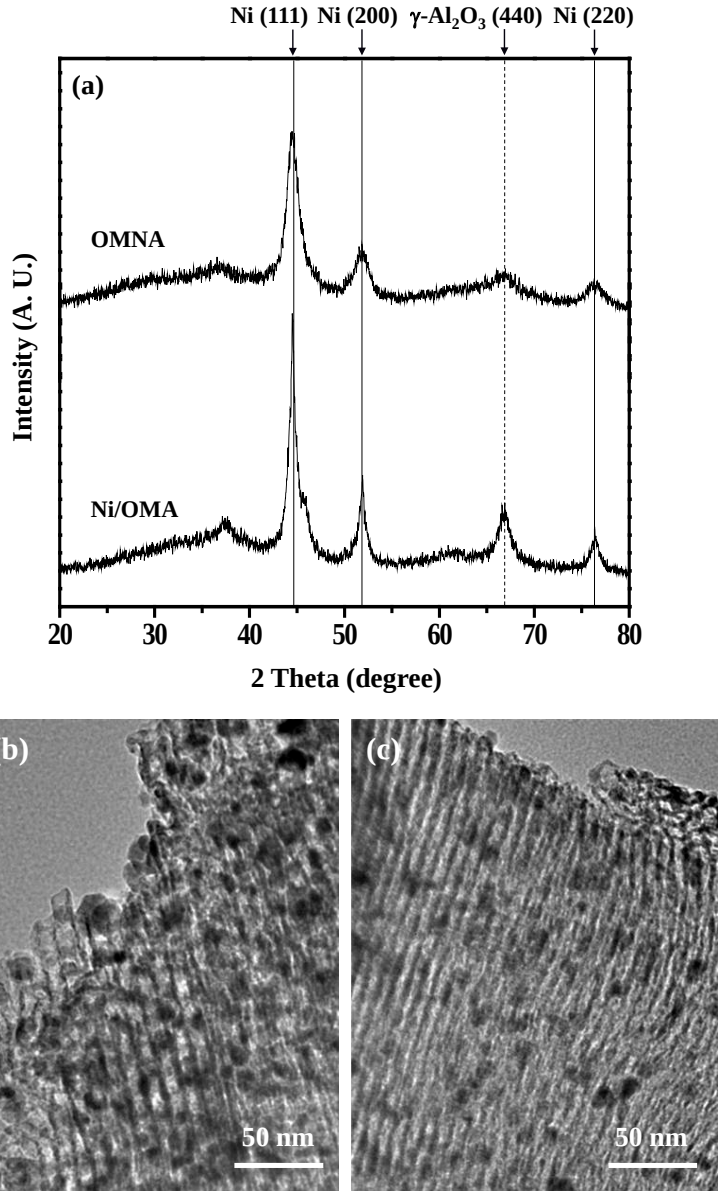

Fig. 3.39. (a) XRD patterns of reduced Ni/OMA and OMNA catalysts, TEM images of reduced (b) Ni/OMA and (c) OMNA catalysts.

Table 3.19

Crystallite size of metallic nickel in the reduced Ni/OMA and OMNA catalysts

Catalyst	Crystallite size of metallic nickel (nm)[a]
Ni/OMA	10.5
OMNA	5.0

[a] Calculated by the Scherrer equation from Ni (200) diffraction peak broadening in Fig. 3.39(a)

3.5.4. Catalytic performance in the steam reforming of LNG

Fig. 3.40 shows the LNG conversion and hydrogen yield with time on stream in the steam reforming of LNG over Ni/OMA and OMNA catalysts at 600 °C. It was found that both Ni/OMA and OMNA catalysts showed a stable catalytic performance without catalyst deactivation. Confinement effect derived from ordered mesopores was responsible for their stable catalytic performance by preventing aggregation of active metallic nickel in the catalysts. It is also believed that gasification reaction between adsorbed carbon intermediates and steam molecules was facilitated on the surface of finely dispersed metallic nickel in the catalysts.

It is interesting to note that OMNA catalyst exhibited a better catalytic performance in the steam reforming of LNG than Ni/OMA catalyst. This result can be explained by the fact that the reduced OMNA catalyst retained a smaller crystallite size of metallic nickel than the reduced Ni/OMA catalyst. According to the previous report [88], many stepped nickel atoms, on which dehydrogenated methane intermediates are stabilized, can be generated with decreasing crystallite size of metallic nickel in the reduced nickel catalyst. Furthermore, it is important to make small nickel crystallites which are finely dispersed in the network of mesoporous support, because carbon deposition is enhanced on the nickel cluster composed of aggregates of adjacent active nickel [87]. This was well supported by the CHNS elemental analysis data of the used catalysts as presented in Table 3.20. It was found that OMNA catalyst exhibited a smaller amount of carbon deposition than Ni/OMA catalyst after a

1000 min-reaction.

XRD patterns of the used Ni/OMA and OMNA catalysts obtained after a 1000 min-reaction were represented in Fig. 3.41(a). Crystallite size of metallic nickel in the used catalysts was calculated by the Scherrer equation as listed in Table 3.21. OMNA catalyst showed smaller crystallite size of metallic nickel than Ni/OMA catalyst. In addition, degree of sintering of metallic nickel in the OMNA catalyst was smaller than that in the Ni/OMA catalyst. This implies that OMNA catalyst retained strong resistance toward sintering of metallic nickel during the steam reforming of LNG compared to Ni/OMA catalyst. It was also observed that the used OMNA catalyst (Fig. 3.41(c)) still exhibited well dispersed nickel particles even after the reaction, while the used Ni/OMA catalyst (Fig. 3.41(b)) showed large agglomerates of nickel particles compared to the reduced Ni/OMA catalyst (Fig. 3.39(b)).

Fig. 3.42 shows the comparison result of catalytic performance in the steam reforming of LNG between nickel-alumina catalysts prepared by an evaporation-induced self-assembly (EISA) method and those prepared by common single-step surfactant-templating methods [109]. Ni/OMA and OMNA catalysts showed a better catalytic performance than Ni-A-CS (a mesoporous Ni-Al_2O_3 catalyst prepared by a single-step cationic surfactant-templating method), Ni-A-AS (a mesoporous Ni-Al_2O_3 catalyst prepared by a single-step anionic surfactant-templating method), and Ni-A-NS (a mesoporous Ni-Al_2O_3 catalyst prepared by a single-step non-ionic surfactant-templating method) catalysts. The result shown in Fig. 3.42 demonstrates that EISA method was more favorable for activating nickel species in the alumina support than common surfactant-templating methods.

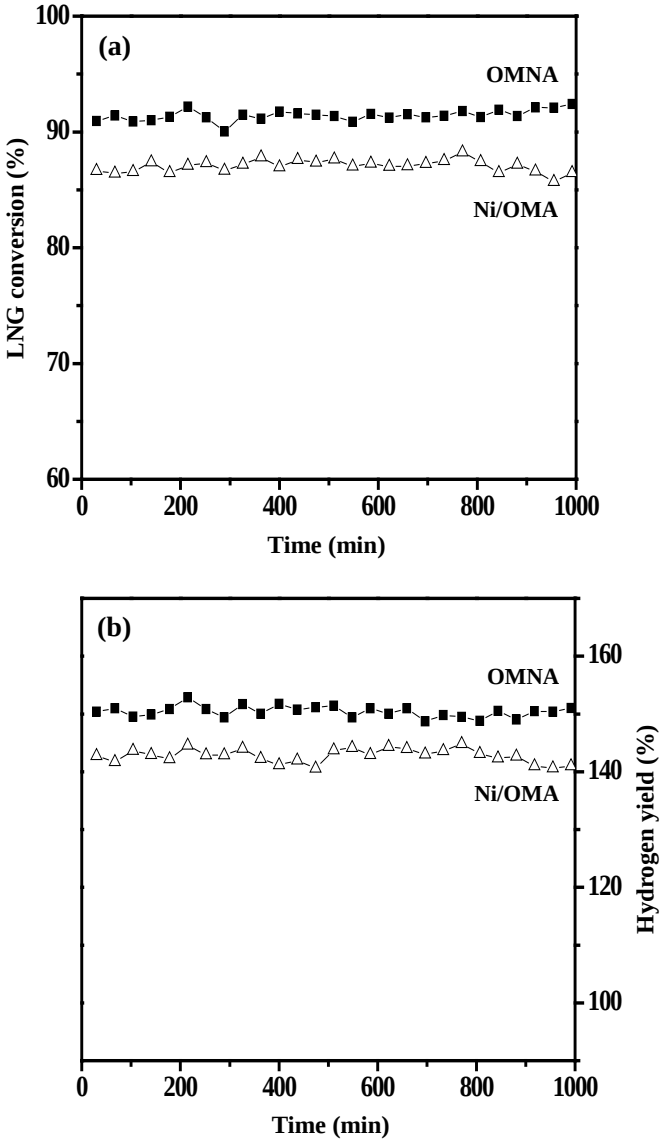

Fig. 3.40. (a) LNG conversion and (b) hydrogen yield with time on stream in the steam reforming of LNG over Ni/OMA and OMNA catalysts at 600 °C. Both catalysts were reduced at 700 °C for 3 h prior to the reaction.

Table 3.20

Amount of carbon deposition in the used Ni/OMA and OMNA catalysts after a 1000 min-reaction

Catalyst	Amount of carbon deposition (wt%)[a]
Ni/OMA	4.9
OMNA	0.1

[a] Determined by CHNS elemental analysis

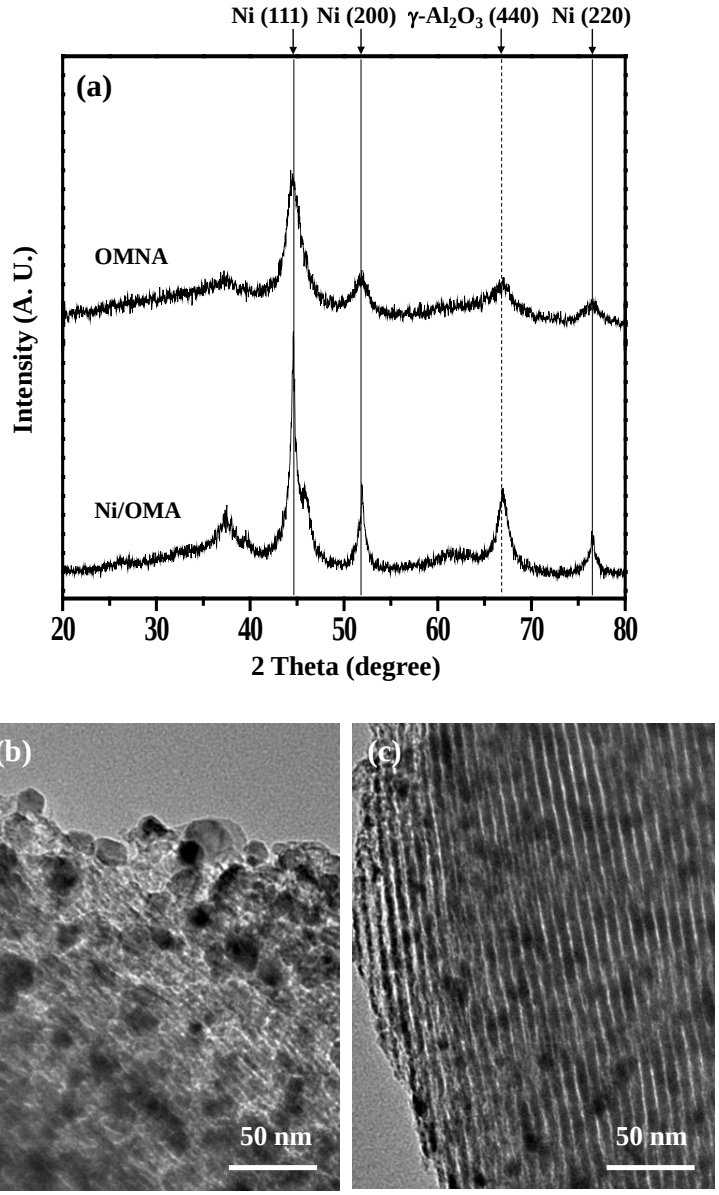

Fig. 3.41. (a) XRD patterns of used Ni/OMA and OMNA catalysts, TEM images of used (b) Ni/OMA and (c) OMNA catalysts.

Table 3.21

Crystallite size of metallic nickel and degree of sintering of the used Ni/OMA and OMNA catalysts after a 1000 min-reaction

Catalyst	Crystallite size of metallic nickel (nm)[a]	Degree of sintering (%)[b]
Ni/OMA	12.8	21.9
OMNA	5.3	8.0

[a] Calculated by the Scherrer equation from Ni (200) diffraction peak broadening in Fig. 10

[b] Calculated by following equation:

$$Degree\ of\ \ sintering\ (\%) = \frac{Crystallite\ size\ of\ \ metallic\ nickel\ after\ reaction\ (nm)}{Crystallite\ size\ of\ \ metallic\ nickel\ after\ reduction\ (nm)} \times 100$$

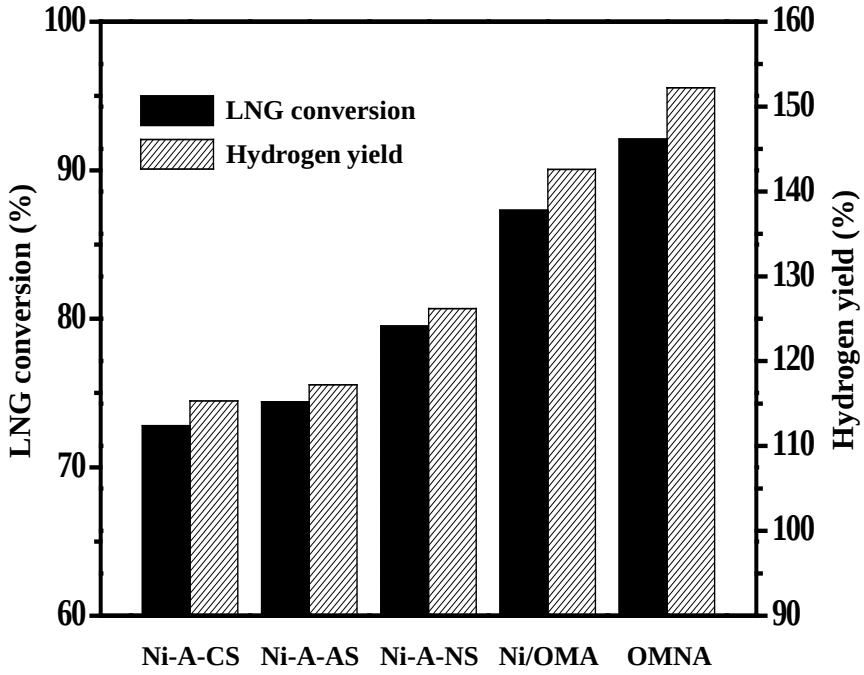

Fig. 3.42. LNG conversion and hydrogen yield over various nickel-alumina catalysts in the steam reforming of LNG at 600 ºC after a 400 min-reaction. All the catalysts were reduced at 700 ºC for 3 h prior to the reaction. Catalytic performance data for Ni-A-CS, Ni-A-AS, and Ni-A-NS catalysts were taken from a literature [109].

3.6. Nickel/alumina catalyst prepared by a chemical immobilization method

3.6.1. Characterization of catalysts

Textural properties of calcined support (Al) and catalysts (NiE/Al and Ni/Al) were examined by nitrogen adsorption-desorption measurements as represented in Fig. 3.43. All the calcined samples showed type-IV isotherm with H2-type hysteresis loop, representing that well-developed mesoporous structure was formed. As listed in Table 3.22, however, NiE/Al catalyst exhibited better textural properties than Ni/Al catalyst in terms of surface area, pore volume, and pore diameter. This result indicates that mesoporous structure of Al support was significantly blocked by nickel species during the impregnation step of Ni/Al catalyst. In case of NiE/Al catalyst, on the other hand, it is believed that nickel species can be finely impregnated onto Al support during the chemical immobilization step due to Coulombic interaction between positively-charged Al support and $Ni(EDTA)^{2-}$ complex ion.

Crystalline structure of calcined support (Al) and catalysts (NiE/Al and Ni/Al) were examined by XRD and TPR analyses. Fig. 3.44(a) shows XRD patterns of calcined samples. Al support showed amorphous feature even after the high temperature calcination process. Both calcined NiE/Al and Ni/Al catalysts exhibited diffraction peaks corresponding to nickel oxide phase and nickel aluminate phase. It is interesting to note that Ni/Al catalyst showed sharper diffraction peaks of nickel oxide phase than NiE/Al catalyst. This

means dispersion of nickel oxide phase in Ni/Al catalyst was poor compared to that in NiE/Al catalyst. As shown in TPR profiles (Fig. 3.44(b)), NiE/Al catalyst showed a single reduction band, while Ni/Al catalyst showed broad reduction band. Reduction peaks at 691-728 ^{o}C in both catalysts are related to reduction of surface nickel aluminate phase or nickel oxide strongly bound to Al support. Additional reduction peak at 382 ^{o}C in Ni/Al catalyst is attributed to free nickel oxide, which is hardly interacting with Al support. Thus, it was revealed that metal-support interaction between nickel species and Al support in NiE/Al catalyst was stronger than that in Ni/Al catalyst. Moreover, this implies that nickel species in Ni/Al catalyst would be vulnerable to nickel sintering during the reduction process compared to those in NiE/Al catalyst.

Fig. 3.45(a) shows XRD patterns of NiE/Al and Ni/Al catalysts reduced at 700 ^{o}C for 3 h. Both reduced catalysts retained metallic nickel phase after the reduction process, representing that nickel species in both catalysts were readily reduced under reduction condition employed in this work. It was found that crystallite size of metallic nickel in NiE/Al catalyst was smaller than that in Ni/Al catalyst (Table 3.23). This indicates NiE/Al catalyst showed high resistance toward nickel sintering compared to Ni/Al catalyst. These differences in crystallite size of both reduced catalysts were also observed in TEM images (Figs. 3.45(b) and 3.45(c)). Consequently, methane adsorption was enhanced on the NiE/Al catalyst compared to the Ni/Al catalyst (Table 3.24). From these results, NiE/Al catalyst was expected to be active in the steam reforming of LNG compared to Ni/Al catalyst.

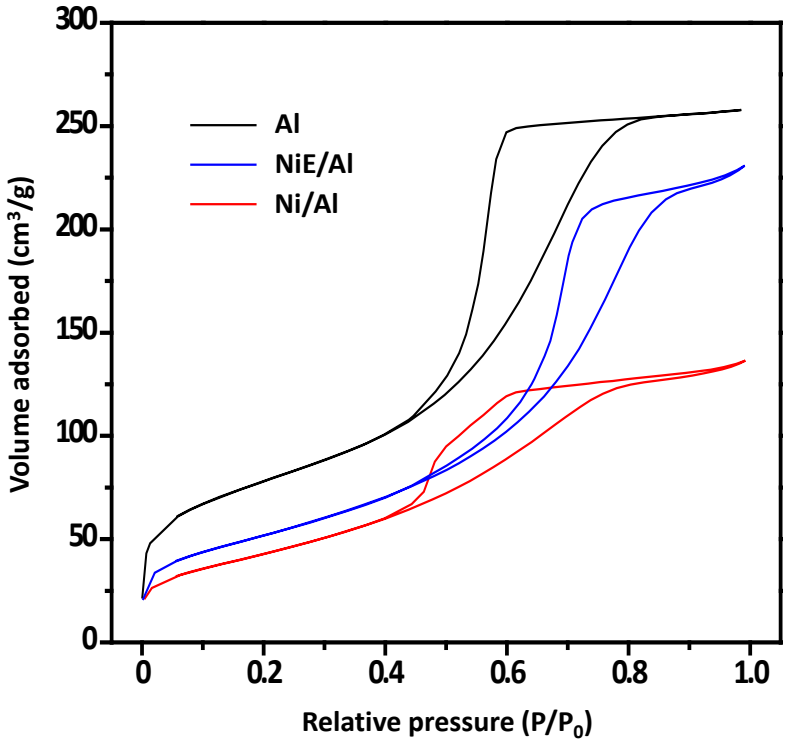

Fig. 3.43. Nitrogen adsorption-desorption isotherms of calcined support (Al) and catalysts (NiE/Al and Ni/Al).

Table 3.22

Textural properties of calcined support (Al) and catalysts (NiE/Al and Ni/Al)

Sample	Al	NiE/Al	Ni/Al
Surface area (m^2/g)[a]	278	188	157
Pore volume (cm^3/g)	0.40	0.36	0.21
Average pore diameter (nm)	5.7	7.6	5.4

[a] Calculated by the BET equation

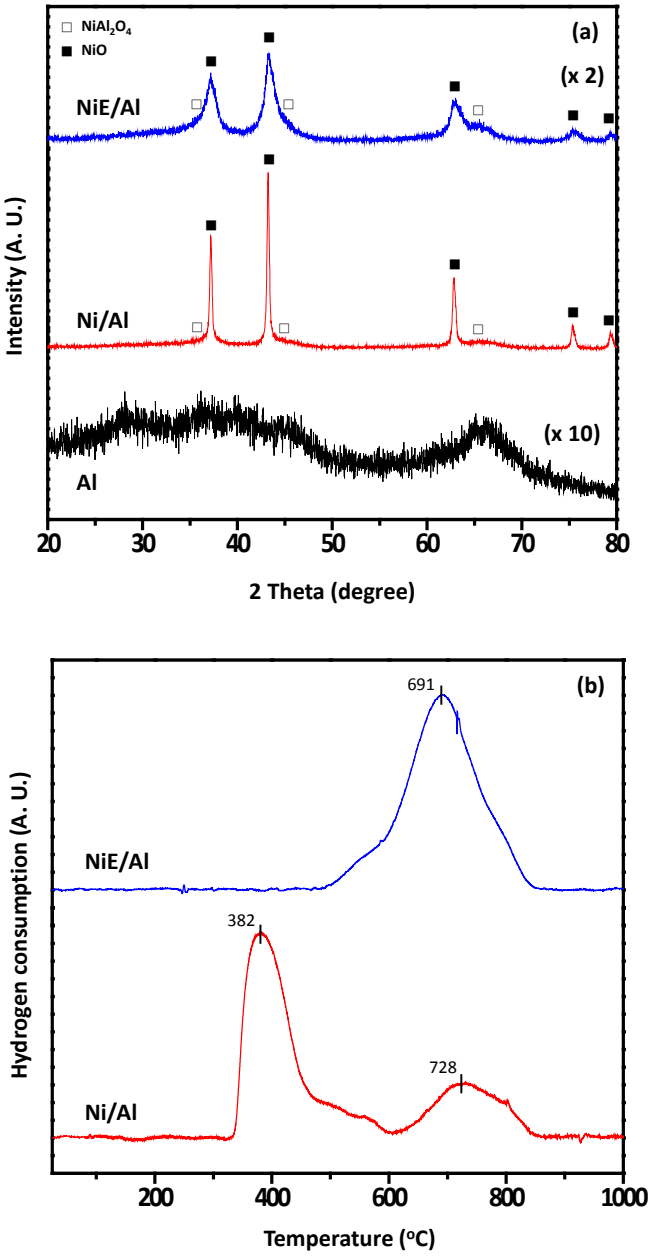

Fig. 3.44. (a) XRD patterns of calcined samples and (b) TPR profiles of calcined catalysts.

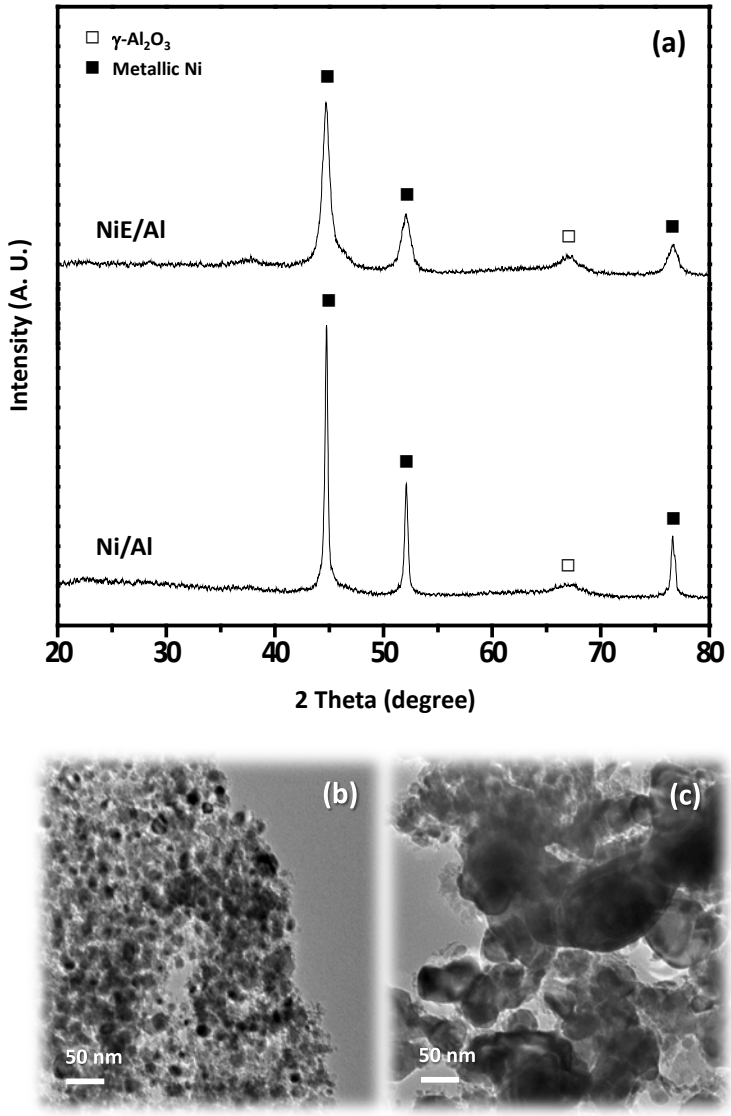

Fig. 3.45. (a) XRD patterns of reduced catalysts and TEM images of reduced (b) NiE/Al and (c) Ni/Al catalysts.

Table 3.23

Crystallite size of metallic nickel in the reduced catalysts

Catalyst	NiE/Al	Ni/Al
Crystallite size of metallic nickel (nm)[a]	10.0	29.8

[a] Calculated by the Scherrer equation from Ni (200) diffraction peak broadening in Fig. 3.45(a)

Table 3.24

Amount of adsorbed CH_4 on the reduced catalysts

Catalyst	Amount of adsorbed CH_4 (μmol-CH_4/g)[a]
NiE/Al	98.7
Ni/Al	50.4

[a] Calculated from peak area of CH_4-TPD profiles

3.6.2. Catalytic performance in the steam reforming of LNG

Catalytic performance in the steam reforming of LNG over NiE/Al and Ni/Al catalysts were represented in Fig. 3.46. Both NiE/Al and Ni/Al catalysts showed stable catalytic performance during the 15 h-reaction without distinct catalyst deactivation. It was also found that NiE/Al catalyst exhibited better catalytic performance than Ni/Al catalyst. This result is due to the fact that NiE/Al catalyst retained smaller nickel crystallite than Ni/Al catalyst after the reduction process. Furthermore, as discussed in CH_4-TPD results (Table 3.24), large methane adsorption capacity of NiE/Al catalyst might be important factor determining high catalytic performance compared to Ni/Al catalyst. Therefore, it is concluded that NiE/Al catalyst prepared by a chemical immobilization method was an efficient catalyst in the hydrogen production by steam reforming of LNG.

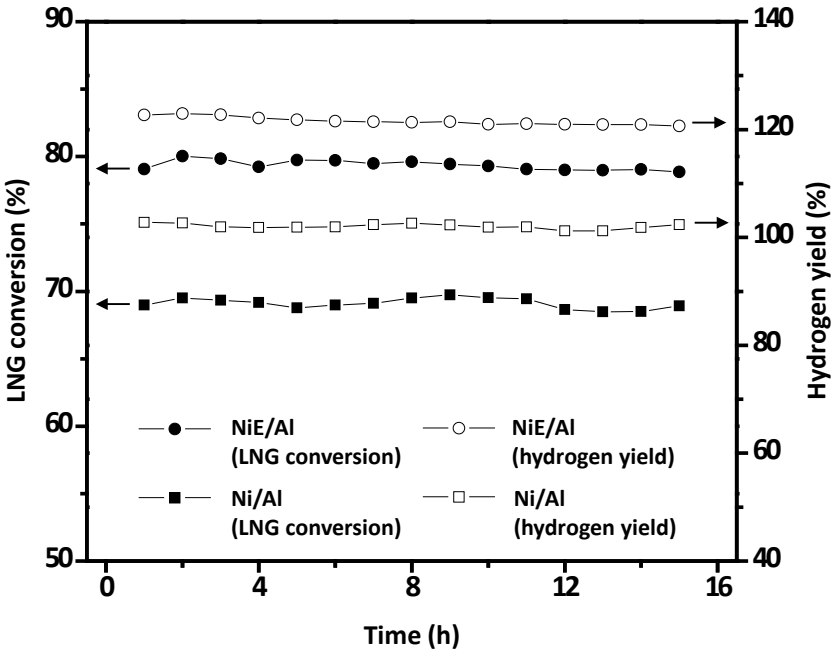

Fig. 3.46. Catalytic performance in the steam reforming of LNG over NiE/Al and Ni/Al catalysts.

Chapter 4. Conclusions

Various nickel-alumina catalysts were prepared and physicochemically modified by several preparation methods including epoxide-driven sol-gel method, carbon-templating method, phosphorus addition, supercritical CO_2 drying, and evaporation-induced self-assembly of triblock copolymer. They were applied to the hydrogen production by steam reforming of LNG, and were characterized by various techniques.

A mesoporous Ni-Al_2O_3 aerogel catalyst was prepared by a single-step epoxide-driven sol-gel method and a subsequent supercritical CO_2 drying method (NA-ES catalyst). For comparison, a mesoporous Ni-Al_2O_3 aerogel catalyst was also prepared by a single-step alkoxide-based sol-gel method and a subsequent supercritical CO_2 drying method (NA-AS catalyst). It was found that epoxide-driven sol-gel method was favorable for fine dispersion of nickel species, because large amount of pentahedral Al atoms served as Lewis acid sites for anchoring nickel species. In the steam reforming of LNG, NA-ES catalyst with small average nickel diameter exhibited higher LNG conversion and hydrogen yield than NA-AS catalyst.

A series of mesoporous nickel-alumina xerogel catalysts (denoted as CNAX) were prepared by a single-step carbon-templating sol-gel method using different amount of carbon template (X). Surface area, pore volume, and average pore diameter of CNAX catalysts increased with increasing the amount of carbon template. It was found that bulk nickel oxide phase was more generated on the surface of CNAX catalysts with increasing the amount

of carbon template, resulting in weak interaction between nickel species and alumina. Crystallite size of metallic nickel in the reduced CNAX catalysts showed a volcano-shaped trend with respect to the amount of carbon template. In the steam reforming of LNG, CNA24 catalyst with the weakest nickel species-alumina interaction experienced a significant deactivation. Initial LNG conversion and initial hydrogen yield over CNAX catalysts in the steam reforming of LNG increased with decreasing crystallite size of metallic nickel of the catalysts.

A series of nickel catalysts supported on mesoporous phosphorus-modified alumina xerogel (Ni/XPA, X = 0, 0.02, 0.05, 0.10, and 0.20) were prepared by an epoxide-driven sol-gel method and a subsequent incipient impregnation method. It was found that the addition of phosphorus affected the metal-support interaction and binding energies of nickel species in the calcined Ni/XPA catalysts. H_2-TPD measurements revealed that the amount of strong hydrogen-binding sites of the reduced Ni/XPA catalysts showed a volcano-shaped trend. Furthermore, the amount of adsorbed methane measured by CH_4-TPD measurements was well correlated with the amount of strong hydrogen-binding sites of the catalysts. In the steam reforming of LNG, Ni/XPA (X = 0, 0.02, and 0.05) catalysts showed a stable catalytic performances while Ni/0.10PA and Ni/0.20PA catalysts experienced a catalyst deactivation due to nickel sintering. Initial catalytic performance of Ni/XPA (X = 0, 0.02, 0.05, 0.10, and 0.20) catalysts in the steam reforming of LNG showed volcano-shaped curves with respect to the P/Al molar ratio. The catalytic performance of Ni/XPA catalysts increased with increasing the amount of adsorbed methane on the catalysts.

A mesoporous nickel-phosphorus-alumina aerogel catalyst (NPAA) was prepared by a single-step epoxide-driven sol-gel method and a subsequent supercritical CO_2 drying method. For comparison, a mesoporous nickel-phosphorus-alumina xerogel catalyst (NPAX) was also prepared. NPAA catalyst showed excellent textural properties compared to NPAX catalyst. H_2-TPD measurements revealed that the reduced NPAA catalyst exhibited large amount of hydrogen uptake and large amount of strong hydrogen-binding sites compared to the reduced NPAX catalyst. This result was well consistent with the CH_4-TPD result in a sense that the reduced NPAA catalyst retained large amount of active nickel sites for methane adsorption. In the steam reforming of LNG, NPAA catalyst with high affinity toward methane showed higher LNG conversion and hydrogen yield than NPAX catalyst.

An ordered mesoporous nickel-alumina catalyst (denoted as OMNA) was prepared by a single-step evaporation-induced self-assembly (EISA) method. For comparison, a nickel catalyst supported on ordered mesoporous alumina support (denoted as Ni/OMA) was prepared by an impregnation method. Textural properties including surface area, pore volume, and average pore diameter of OMNA catalyst were superior to those of Ni/OMA catalyst. Furthermore, crystallite size of metallic nickel in the OMNA catalyst was smaller than that in the Ni/OMA catalyst, due to the high resistance toward aggregation of nickel species of OMNA catalyst during the reduction process. In the steam reforming of LNG, OMNA catalyst with small crystallite size of metallic nickel showed a better catalytic performance than Ni/OMA catalyst in terms of LNG conversion and hydrogen yield. It was also found that Ni/OMA and OMNA catalysts exhibited a better catalytic performance than

nickel-alumina catalysts prepared by common single-step surfactant-templating methods.

A nickel/alumina catalyst (NiE/Al) was prepared by a chemical immobilization method. For comparison, another nickel/alumina catalyst (Ni/Al) was also prepared by a conventional impregnation method. It was revealed that NiE/Al catalyst retained better physicochemical properties in terms of surface area, crystallite size of metallic nickel, and methane adsorption capacity than Ni/Al catalyst. These superior physicochemical properties of NiE/Al catalyst compared to those of Ni/Al catalyst were due to fine impregnation of nickel precursor by Coulombic interaction between alumina support and $Ni(EDTA)^{2-}$ complex anion. Accordingly, NiE/Al catalyst showed better catalytic performance in the steam reforming of LNG than Ni/Al catalyst.

In summary, physicochemical properties of nickel-alumina catalysts were modified by various catalyst preparation methods. Catalytic performance of the catalysts were closely related to several physicochemical properties such as surface area, porosity, crystalline structure, reducibility, nickel dispersion, and methane adsorption affinity. Especially, it was found that nickel dispersion and methane adsorption affinity of reduced catalysts served as an important factor determining overall catalytic activity in the hydrogen production by steam reforming of LNG. Therefore, optimal preparation methods and conditions are required in order to generate highly active nickel species on the surface of nickel-alumina reforming catalyst for efficient hydrogen production.

Bibliography

[1] J. Goldemberg, “Ethanol for a sustainable energy future”, *Science* **315** (2007) 808.

[2] S. Chu, A. Majumdar, “Opportunities and challenges for a sustainable energy future”, *Nature* **488** (2012) 294.

[3] I. Dincer, “Renewable energy and sustainable development: A crucial review”, *Renew. Sustain. Energy Rev.* **4** (2000) 157.

[4] H. Lund, “Renewable energy strategies for sustainable development”, *Energy* **32** (2007) 912.

[5] C. Song, “Global challenges and strategies for control, conversion and utilization of CO_2 for sustainable development involving energy, catalysis, adsorption and chemical processing”, *Catal. Today* **115** (2006) 2.

[6] A. Haryanto, S. Fernando, N. Murali, S. Adhikari, “Current Status of Hydrogen Production Techniques by Steam Reforming of Ethanol: A Review”, *Energy Fuels* **19** (2005) 2098.

[7] M. Ball, M. Wietschel, “The future of hydrogen - Opportunities and challenges”, *Int. J. Hydrogen Energy* **34** (2009) 615.

[8] J.A. Turner, “Sustainable hydrogen production”, *Science* **305** (2004) 972.

[9] A. Kirubakaran, S. Jain, R.K. Nema, “A review on fuel cell technologies and power electronic interface”, *Renew. Sustain. Energy Rev.* **13** (2009) 2430.

[10] S. Mekhilef, R. Saidur, A. Safari, “Comparative study of different fuel cell technologies”, *Renew. Sustain. Energy Rev.* **16** (2012) 981.

[11] C. Song, “Fuel processing for low-temperature and high-temperature fuel cells: Challenges, and opportunities for sustainable development in the 21st century”, *Catal. Today* **77** (2002) 17.

[12] V. Subramani, P. Sharma, L. Zhang, K. Liu, “Catalytic steam reforming technology for the production of hydrogen and syngas”, K. Liu, C. Song, V. Subramani (Eds.), *Hydrogen and syngas production and purification technologies*, Wiley & Sons, Inc., New York (2010) 14.

[13] J.N. Armor, “The multiple roles for catalysis in the production of H_2”, *Appl. Catal. A: Gen.* **176** (1999) 159.

[14] A. Ballarini, P. Benito, G. Fornasari, O. Scelza, A Vaccari, “Role of the composition and preparation method in the activity of hydrotalcite-derived Ru catalysts in the catalytic partial oxidation of methane”, *Int. J. Hydrogen Energy* **38** (2013) 15128.

[15] F. Meng, G. Chen, Y. Wang, Y. Liu, “Metallic Ni monolith-Ni/$MgAl_2O_4$ dual bed catalysts for the autothermal partial oxidation of methane to synthesis gas”, *Int. J. Hydrogen Energy* **35** (2010) 8182.

[16] J.S. Lisboa, L.E. Terra, P.R.J. Silva, H. Saitovitch, F.B. Passos, “Investigation of Ni/Ce-ZrO_2 catalysts in the autothermal reforming of methane”, *Fuel. Process. Technol.* **92** (2011) 2075.

[17] M.H. Youn, J.G. Seo, H. Lee, Y. Bang, J.S. Chung, I.K. Song, “Hydrogen production by auto-thermal reforming of ethanol over nickel catalysts supported on metal oxides: Effect of support acidity”, *Appl. Catal. B: Environ.* **98** (2010) 57.

[18] C.E. Daza, J. Gallego, F. Mondragón, S. Moreno, R. Molina, “High stability of Ce-promoted Ni/Mg-Al catalysts derived from hydrotalcites in dry reforming of methane”, *Fuel* **89** (2010) 592.

[19] S. Damyanova, B. Pawelec, K. Arishtirova, M.V. Martinez Huerta, J.L.G. Fierro, “The effect of CeO_2 on the surface and catalytic properties of Pt/CeO_2-ZrO_2 catalysts for methane dry reforming”, *Appl. Catal. B: Environ.* **89** (2009) 149.

[20] K. Hou, R. Hughes, “The kinetics of methane steam reforming over a Ni/α-Al_2O_3 catalyst”, *Chem. Eng. J.* **82** (2001) 311.

[21] J.P. Van Hook, “Methane-steam reforming”, *Catal. Rev. Sci. Eng.* **21** (1980) 1.

[22] Y. Li, X. Wang, C. Xie, C. Song, “Influence of ceria and nickel addition to alumina-supported Rh catalyst for propane steam reforming at low temperatures”, *Appl. Catal. A: Gen.* **357** (2009) 213.

[23] H. Jeong, M. Kang, “Hydrogen production from butane steam reforming over Ni/Ag loaded $MgAl_2O_4$ catalyst”, *Appl. Catal. B: Environ.* **95** (2010) 446.

[24] D.R. Palo, R.A. Dagle, J.D. Holladay, “Methanol steam reforming for hydrogen production”, *Chem. Rev.* **107** (2007) 3992.

[25] V.V. Galvita, G.L. Semin, V.D. Belyaev, V.A. Semikolenov, P. Tsiakaras, V.A. Sobyanin, “Synthesis gas production by steam reforming of ethanol”, *Appl. Catal. A: Gen.* **220** (2001) 123.

[26] K. Takanabe, K. Aika, K. Inazu, T. Baba, K. Seshan, L. Lefferts, “Steam reforming of acetic acid as a biomass derived oxygenate: Bifunctional pathway for hydrogen formation over Pt/ZrO_2 catalysts”, *J. Catal.* **243** (2006) 263.

[27] B. Zhang, X. Tang, Y. Li, Y. Xu, W. Shen, “Hydrogen production from steam reforming of ethanol and glycerol over ceria-supported metal catalysts”, *Int. J. Hydrogen Energy* **32** (2007) 2367.

[28] Y. Wang, Y.H. Chin, R.T. Rozmiarek, B.R. Johnson, Y. Gao, J. Watson, A.Y.L. Tonkovich, D.P. Vander Wiel, “Highly active and stable $Rh/MgO\text{-}Al_2O_3$ catalysts for methane steam reforming”, *Catal. Today* **98** (2004) 575.

[29] R. Craciun, W. Daniell, H. Knözinger, “The effect of CeO_2 structure on the activity of supported Pd catalysts used for methane steam reforming”, *Appl. Catal. A: Gen.* **230** (2002) 153.

[30] A. Berman, R.K. Karn, M. Epstein, “Kinetics of steam reforming of methane on Ru/Al_2O_3 catalyst promoted with Mn oxides”, *Appl. Catal.*

A: Gen. **282** (2005) 73.

[31] A.F. Lucrédio, E.M. Assaf, "Cobalt catalysts prepared from hydrotalcite precursors and tested in methane steam reforming", *J. Power. Sources* **159** (2006) 667.

[32] M. Zeppieri, P.L. Villa, N. Verdone, M. Scarsella, P.D. Filippis, "Kinetic of methane steam reforming reaction over nickel- and rhodium-based catalysts", *Appl. Catal. A: Gen.* **387** (2010) 147.

[33] J.G. Seo, M.H. Youn, K.M. Cho, S. Park, S.H. Lee, J. Lee, I.K. Song, "Effect of Al_2O_3-ZrO_2 xerogel support on hydrogen production by steam reforming of LNG over Ni/Al_2O_3-ZrO_2 catalyst", *Korean J. Chem. Eng.* **25** (2008) 41.

[34] J.R. Rostrup-Nielsen, "New aspects of syngas production and use", *Catal. Today* **63** (2000) 159.

[35] G. Jones, J.G. Jakobsen, S.S. Shim, J. Kleis, M.P. Andersson, F. Abild-Pedersen, T. Bligaard, S. Helveg, B. Hinnemann, J.R. Rostrup-Nielsen, I. Chorkendorff, J. Sehested, J.K. Nørskov, "First principles calculations and experimental insight into methane steam reforming over transition metal catalysts", *J. Catal.* **259** (2008) 147.

[36] J. Sehested, "Four challenges for nickel steam-reforming catalysts", *Catal. Today* **111** (2006) 103.

[37] D.L. Trimm, "Catalysts for the control of coking during steam reforming", *Catal. Today* **49** (1999) 3.

[38] G. Wu, S. Li, C. Zhang, T. Wang, J. Gong, "Glycerol steam reforming over perovskite-derived nickel-based catalysts", *Appl. Catal. B: Environ.* **144** (2014) 277.

[39] S.Q. Chen, Y. Liu, "$LaFe_yNi_{1-y}O_3$ supported nickel catalysts used for steam reforming of ethanol", *Int. J. Hydrogen Energy* **34** (2009) 4735.

[40] X. Guo, Y. Sun, Y. Yu, X. Zhu, C. Liu, "Carbon formation and steam reforming of methane on silica supported nickel catalysts", *Catal.*

Commun. **19** (2012) 61.

[41] J.G. Seo, M.H. Youn, J.C. Jung, I.K. Song, "Hydrogen production by steam reforming of liquefied natural gas (LNG) over mesoporous nickel-alumina aerogel catalyst", *Int. J. Hydrogen Energy* **35** (2010) 6738.

[42] Y. Choi, N.D. Kim, J. Back, W. Kim, H.J. Lee, J. Yi, "Effect of N_2O-mediated calcination on nickel species and the catalytic activity of nickel catalysts supported on γ-Al_2O_3 in the steam reforming of glycerol", *Int. J. Hydrogen Energy* **36** (2011) 3844.

[43] J.G. Seo, M.H. Youn, K.M. Cho, S. Park, I.K. Song, "Hydrogen production by steam reforming of liquefied natural gas over a nickel catalyst supported on mesoporous alumina xerogel", *J. Power Sources* **173** (2007) 943.

[44] J. Xu, C.M.Y. Yeung, J. Ni, F. Meunier, N. Acerbi, M. Fowles, S.C. Tsang, "Methane steam reforming for hydrogen production using low water-ratios without carbon formation over ceria coated Ni catalysts", *Appl. Catal. A: Gen.* **345** (2008) 119.

[45] Y.-S. Jung, W.-L. Yoon, Y.-W. Rhee, Y.-S. Seo, "The surfactant-assisted Ni-Al_2O_3 catalyst prepared by a homogeneous precipitation method for CH_4 steam reforming", *Int. J. Hydrogen Energy* **37** (2012) 9340.

[46] A.J. Majewski, J. Wood, W. Bujalski, "Nickel-silica core@shell catalyst for methane reforming", *Int. J. Hydrogen Energy* **38** (2013) 14531.

[47] M. Tada, S. Zhang, S. Malwadkar, N. Ishiguro, J. Soga, Y. Nagai, K. Tezuka, H. Imoto, S. Otsuka-Yao-Matsuo, S. Ohkoshi, Y. Iwasawa, "The active phase of nickel/ordered $Ce_2Zr_2O_x$ catalysts with a discontinuity (x=7-8) in methane steam reforming", *Angew. Chem.* **124** (2012) 9495.

[48] J.R. Rostrup-Nielsen, "Coking on nickel catalysts for steam reforming of hydrocarbons", *J. Catal.* **33** (1974) 184.

[49] S.S. Maluf, E.M. Assaf, "Ni catalysts with Mo promoter for methane

steam reforming", *Fuel* **88** (2009) 1547.

[50] J.D.S. Lisboa, D.C.R.M. Santos, F.B. Passos, F.B. Noronha, " Influence of the addition of promoters to steam reforming catalysts", *Catal. Today* **101** (2005) 15.

[51] J.G. Seo, M.H. Youn, Y. Bang, I.K. Song, "Hydrogen production by steam reforming of simulated liquefied natural gas (LNG) over mesoporous nickel-M-alumina (M = Ni, Ce, La, Y, Cs, Fe, Cu, and Mg) aerogel catalysts", *Int. J. Hydrogen Energy* **36** (2011) 3505.

[52] O. Yamazaki, K. Tomishige, K. Fujimoto, "Development of highly stable nickel catalyst for methane-steam reaction under low steam to carbon ratio", *Appl. Catal. A: Gen.* **136** (1996) 49.

[53] F. Bimbela, D. Chen, J. Ruiz, L. García, J. Arauzo, "Ni/Al coprecipitated catalysts modified with magnesium and copper for the catalytic steam reforming of model compounds from biomass pyrolysis liquids", *Appl. Catal. B: Environ.* **119** (2012) 1.

[54] J. Xu, L. Chen, K.F. Tan, A. Borgna, M. Saeys, "Effect of boron on the stability of Ni catalysts during steam methane reforming", *J. Catal.* **261** (2009) 158.

[55] M. Koike, D. Li, Y. Nakagawa, K. Tomishige, "A highly active and coke-resistant steam reforming catalyst comprising uniform nickel-iron alloy nanoparticles", *ChemSusChem* **5** (2012) 2312.

[56] E. Breval, Z. Deng, S. Chiou, C.G. Pantano, "Sol-gel prepared Ni-alumina composite materials", *J. Mater. Sci.* **27** (1992) 1464.

[57] J.-I. Ishiyama, Y. Kurokawa, T. Nakayama, S. Imaizumi, "New preparation technique for a highly dispersed nickel-alumina catalyst and its application to liquid phase hydrogenation", *Appl. Catal.* **40** (1988) 139.

[58] B.E. Yoldas, "A transparent porous alumina", *Am. Ceram. Soc. Bull.* **54** (1975) 286.

[59] A.E. Gash, T.M. Tillotson, J.H. Satcher, J.F. Poco, L.W. Hrubesh, R.L. Simpson, “Use of epoxides in the sol-gel synthesis of porous iron(III) oxide monoliths from Fe(III) salts”, *Chem. Mater.* **13** (2001) 999.

[60] T.F. Baumann, A.E. Gash, S.C. Chinn, A.M. Sawvel, R.S. Maxwell, J.H. Satcher, “Synthesis of high-surface-area alumina aerogels without the use of alkoxide precursor”, *Chem. Mater.* **17** (2005) 395.

[61] L. Chen, J. Zhu, Y.-M. Liu, Y. Cao, H.-X. Li, H.-Y. He, W.-L. Dai, K.-N. Fan, “Photocatalytic activity of epoxide sol-gel derived titania transformed into nanocrystalline aerogel powders by supercritical drying”, *J. Mol. Catal. A: Chem.* **255** (2006) 260.

[62] S.M. Morris, P.F. Fulvio, M. Jaroniec, “Ordered mesoporous alumina-supported metal oxides”, *J. Am. Chem. Soc.* **130** (2008) 15210.

[63] M. Rezaei, S.M. Alavi, S. Sahebdelfar, Z.-F. Yan, “Mesoporous nanocrystalline zirconia powders: A promising support for nickel catalyst in CH_4 reforming with CO_2”, *Mater. Lett.* **61** (2007) 2628.

[64] V.F. Stone, R.J. Davis, “Synthesis, characterization, and photocatalytic activity of titania and niobia mesoporous molecular sieves”, *Chem. Mater.* **10** (1998) 1468.

[65] D.L. Hoang, S.H. Chan, O.L. Ding, “Hydrogen production for fuel cells by autothermal reforming of methane over sulfide nickel catalyst on a gamma alumina support”, *J. Power Sources* **159** (2006) 1248.

[66] L. Pelletier, D.D.S. Liu, “Stable nickel catalysts with alumina-aluminum phosphate supports for partial oxidation and carbon dioxide reforming of methane”, *Appl. Catal. A: Gen.* **317** (2007) 293.

[67] S. Chen, Y. Zhang, M. Wu, W. Fang, Y. Yang, “Study on methanethiol synthesis from H_2S and dimethyl sulfide over Al_2O_3 catalysts promoted with phosphorus”, *Appl. Catal. A: Gen.* **431** (2012) 151.

[68] F. Huang, Y. Zheng, Z. Li, Y. Xiao, Y. Zheng, G. Cai, K. Wei, “Synthesis of highly dispersed ceria-zirconia supported on ordered

mesoporous alumina", *Chem. Commun.* **47** (2011) 5247.

[69] S.M. Morris, J.A. Horton, M. Jaroniec, "Soft-templating synthesis and properties of mesoporous alumina-titania", *Micropor. Mesopor. Mater.* **128** (2010) 180.

[70] G. Li, D. Zhang, J.C. Yu, "Thermally stable ordered mesoporous CeO_2/TiO_2 visible-light photocatalysts", *Phys. Chem. Chem. Phys.* **11** (2009) 3775.

[71] Z.-X. Li, F.-B. Shi, L.-L. Li, T. Zhang, C.-H. Yan, "A facile route to ordered mesoporous-alumina-supported catalysts, and their catalytic activities for CO oxidation", *Phys. Chem. Chem. Phys.* **13** (2011) 2488.

[72] Q. Yuan, H.-H. Duan, Z.-X. Li, W.-T. Duan, L.-S. Zhang, W.-G. Song, C.-H. Yan, "Homogeneously dispersed ceria nanocatalyst stabilized with ordered mesoporous alumina", *Adv. Mater.* **22** (2010) 1475.

[73] Y. Bang, J.G. Seo, M.H. Youn, I.K. Song, "Hydrogen production by steam reforming of liquefied natural gas (LNG) over mesoporous Ni-Al_2O_3 aerogel catalyst prepared by a single-step epoxide-driven sol-gel method", *Int. J. Hydrogen Energy* **37** (2012) 1436.

[74] T.-Y. Wei, C.-H. Chen, H.-C. Chien, S.-Y. Lu, C.-C. Hu, "A cost-effective supercapacitor material of ultrahigh specific capacitances: spinel nickel cobaltite aerogels from an epoxide-driven sol–gel process", *Adv. Mater.* **22** (2010) 347.

[75] W. Cai, J. Yu, C. Anand, A. Vinu, M. Jaroniec, "Facile synthesis of ordered mesoporous alumina and alumina-supported metal oxides with tailored adsorption and framework properties", *Chem. Mater.* **23** (2011) 1147.

[76] Q. Yuan, A.-X. Yin, C. Luo, L.-D. Sun, Y.-W. Zhang, W.-T. Duan, H.-C. Liu, C.-H. Yan, "Facile synthesis for ordered mesoporous γ-aluminas with high thermal stability", *J. Am. Chem. Soc.* **130** (2008) 3465.

[77] V. González-Peña, C. Márquez-Alvarez, I. Díaz, M. Grande, T. Blasco, J. Pérez-Pariente, “Sol-gel synthesis of mesostructured aluminas from chemically modified aluminum *sec*-butoxide using non-ionic surfactant templating”, *Micropor. Mesopor. Mater.* **80** (2005) 173.

[78] K.S.W. Sing, D.H. Everett, R.A.W. Haul, L. Moscou, R.A. Pierotti, J. Rouquérol, T. Siemieniewska, “Reporting physisorption data for gas/solid systems”, *Pure Appl. Chem.* **57** (1985) 603.

[79] P. Kim, Y. Kim, H. Kim, I.K. Song, J. Yi, “Preparation, characterization, and catalytic activity of NiMg catalysts supported on mesoporous alumina for hydrodechlorination of *o*-dichlorobenzene”, *J. Mol. Catal. A: Chem.* **231** (2005) 247.

[80] E.D. Dimotakis, T.J. Pinnavaia, “New route to layered double hydroxides intercalated by organic anions: precursors to polyoxometalate-pillared derivatives”, *Inorg. Chem.* **29** (1990) 2393.

[81] W. Zhang, M. Sun, R. Prins, “A high-resolution of MAS NMR study of the structure of fluorinated NiW/γ-Al_2O_3 hydrotreating catalysts”, *J. Phys. Chem. B* **107** (2003) 10977.

[82] T. Onfroy, W.-C. Li, F. Schüth, H. Knözinger, “Surface chemistry of carbon-templated mesoporous aluminas”, *Phys. Chem. Chem. Phys.* **11** (2009) 3671.

[83] Y. Kim, C. Kim, P. Kim, J. Yi, “Effect of preparation conditions on the phase transformation of mesoporous alumina”, *J. Non-Cryst. Solids* **351** (2005) 550.

[84] X. Krokidis, P. Raybaud, A.-E. Gobichon, B. Rebours, R. Enzen, H. Toulhoat, “Theoretical study of the dehydration process of boehmite to gamma-alumina”, *J. Phys. Chem. B* **105** (2001) 5121.

[85] J.H. Kwak, J.Z. Hu, D.H. Kim, J. Szanyi, C.H.F. Peden, “Penta-coordinated Al^{3+} ions as preferential nucleation sites for BaO on γ-Al_2O_3: An ultra-high-magnetic field ^{27}Al MAS NMR study”, *J. Catal.* **251**

(2007) 189.

[86] M. Wu, D.M. Hercules, “Studies of supported nickel catalysts by X-ray photoelectron and ion scattering spectroscopies”, *J. Phys. Chem.* **83** (1979) 2003.

[87] D.L. Trimm, “The steam reforming of natural gas: Problems and some solutions”, *Stud. Surf. Sci. Catal.* **36** (1987) 39.

[88] J.R. Rostrup-Nielsen, J.K. Nørskov, “Step sites in syngas catalysis”, *Top. Catal.* **40** (2006) 1.

[87] C.H. Bartholomew, R.B. Pannell, “The stoichiometry of hydrogen and carbon monoxide chemisorption on alumina- and silica-supported nickel”, *J. Catal.* **65** (1980) 390.

[88] J.G. Seo, M.H. Youn, J.S. Chung, I.K. Song, “Effect of calcination temperature of mesoporous nickel-alumina catalysts on their catalytic performance in hydrogen production by steam reforming of liquefied natural gas (LNG)”, *J. Ind. Eng. Chem.* **16** (2010) 795.

[89] A.N. Kharat, P. Pendleton, A. Badalyan, M. Abedini, M.M. Amini, “Decomposition of nickel formate on sol-gel alumina and characterization of product by X-ray photoelectron and TOF-SIMS spectroscopies”, *J. Catal.* **205** (2002) 7.

[90] A. Cimino, M.L. Jacono, M. Schiavello, “Structural, magnetic, and optical properties of nickel oxide supported on eta- and gamma-aluminas”, *J. Phys. Chem.* **75** (1971) 1044.

[91] P. Salagre, J.L.G. Fierro, F. Medina, J.E. Sueiras, “Characterization of nickel species on several γ-alumina supported nickel samples”, *J. Mol. Catal. A: Chem.* **106** (1996) 125.

[92] M. Wu, D.M. Herculse, “Studies of supported nickel catalysts by X-ray photoelectron and ion scattering spectroscopies”, *J. Phys. Chem.* **83** (1979) 2003.

[93] A. Cimino, M.L. Jacono, M. Schiavello, “The stoichiometry of hydrogen

and carbon monoxide chemisorption on alumina- and silica-supported nickel", *J. Phys. Chem.* **79** (1975) 243.

[94] J.S. Valente, S. Falcón, E. Lima, M.A. Vera, P. Bosch, E. López-Salinas, "Phosphating alumina: A way to tailor its surface properties", *Micropor. Mesopor. Mater.* **94** (2006) 277.

[95] J. Chen, L. Sun, R. Wang, J. Zhang, "Hydrodechlorination of chlorobenzene over Ni_2P/SiO_2 catalysts: Influence of Ni_2P loading", *Catal. Lett.* **133** (2009) 346.

[96] R. Yang, X. Li, J. Wu, X. Zhang, Z. Zhang, Y. Cheng, "Hydrotreating of crude 2-ethylhexanol over Ni/Al_2O_3 catalysts: Surface Ni species-catalytic activity correlation", *Appl. Catal. A: Gen.* **368** (2009) 105.

[97] S. Natesakhawat, R.B. Watson, X. Wang, U.S. Ozkan, "Deactivation characteristics of lanthanide-promoted sol−gel Ni/Al_2O_3 catalysts in propane steam reforming", *J. Catal.* **234** (2005) 496.

[98] R. López-Fonseca, C. Jiménez-González, B. Rivas, J.I. Gutiérrez-Ortiz, "Partial oxidation of methane to syngas on bulk $NiAl_2O_4$ catalyst. Comparison with alumina supported nickel, platinum and rhodium catalysts", *Appl. Catal. A: Gen.* **437** (2012) 53.

[99] S. Damyanova, B. Pawelec, K. Arishtirova, J.L.G. Fierro, "Biogas reforming over bimetallic PdNi catalysts supported on phosphorus-modified alumina", *Int. J. Hydrogen Energy* **36** (2011) 10635.

[100] S. Velu, S.K. Gangwal, "Synthesis of alumina supported nickel nanoparticle catalysts and evaluation of nickel metal dispersions by temperature programmed desorption", *Solid State Ionics* **177** (2006) 803.

[101] L. Qian, Z. Yan, "Studies on the adsorption and dissociation of methane and carbon dioxide on nickel catalysts", *J. Nat. Gas Chem.* **11** (2002) 151.

[102] S.E. Denmark, G.L. Beutner, "Lewis base catalysis in organic synthesis",

Angew. Chem. Int. Ed. **47** (2008) 1560.

[103] N. Salhi, C. Petit, A. Kiennemann, "Steam reforming of methane on nickel aluminate defined structures with high Al/Ni ratio", *Stud. Surf. Sci. Catal.* **174** (2008) 1335.

[104] Y. Bang, S.J. Han, J. Yoo, J.H. Choi, K.H. Kang, J.H. Song, J.G. Seo, J.C. Jung, I.K. Song, "Hydrogen production by steam reforming of liquefied natural gas (LNG) over trimethylbenzene-assisted ordered mesoporous nickel-alumina catalyst", *Int. J. Hydrogen Energy* **38** (2013) 8751.

[105] P.I. Ravikovitch, A.V. Neimark, "Characterization of micro- and mesoporosity in SBA-15 materials from adsorption data by the NLDFT method", *J. Phys. Chem. B* **105** (2001) 6817.

[106] D. Baute, D. Goldfarb, "Interaction of nitrates with Pluronic micelles and their role in the phase formation of mesoporous materials", *J. Phys. Chem. C* **111** (2007) 10931.

[107] S.M. Grant, M. Jaroniec, "Effect of acid concentration on pore size in polymer-templated mesoporous alumina", *J. Mater. Chem.* **22** (2012) 86.

[108] M.H. Youn, J.G. Seo, K.M. Cho, J.C. Jung, H. Kim, K.W. La, D.R. Park, S. Park, S.H. Lee, I.K. Song, "Effect of support on hydrogen production by auto-thermal reforming of ethanol over supported nickel catalysts", *Korean J. Chem. Eng.* **25** (2008) 236.

[109] J.G. Seo, M.H. Youn, I.K. Song, "Mesoporous nickel-alumina catalysts for hydrogen production by steam reforming of liquefied natural gas (LNG)", *Catal. Surv. Asia* **14** (2010) 1.

초 록

수소는 청정하고 연소 시 질소 및 황 산화물을 방출하지 않기 때문에 전도유망한 에너지 전달 매체로서 큰 관심을 받고 있다. 수소 활용에 있어서 수소의 높은 에너지 함량도 장점이 될 수 있다. 이러한 수소의 특징은 수소 자동차, 엔진 및 연료 전지 등과 같은 수소 활용 제품의 발전을 이끌고 있다. 광촉매 반응 및 전기 분해에 의한 물 분해가 수소 생산의 궁극적인 해법으로 알려지기는 하였으나, 낮은 생산성과 높은 비용으로 인해 상용화가 되기는 어려운 실정이다. 이를 대신하여 탄화수소로부터 상용적으로 수소를 생산하기 위해 수증기 개질, 부분 산화, 자열 개질 및 건식 개질 등의 다양한 촉매적 개질 공정들이 활발히 연구되어 왔다. 이러한 개질 공정 중에서 경제성이 높은 수증기 개질이 수소 생산에 가장 널리 이용되어 왔다. 그리고 메탄이 주성분이며 풍부하게 존재하는 액화천연가스(LNG)는 수증기 개질을 통한 수소 생산의 일차적인 원료로 사용될 수 있다. 따라서, 현대적 도시에 LNG 공급 라인이 확장됨에 따라 LNG는 연료 개질기가 장착된 연료 전지 시스템의 중요한 수소 공급원이 될 것으로 기대된다.

수증기 개질 반응에 가장 적합한 촉매로서 저렴하면서도 높은 활성을 보이는 니켈 기반 촉매가 고려되어 왔다. 상용 수증기 개질 반응은 니켈 기반 촉매 상의 최대한의 반응 활성을 얻기 위하여 고온 (> 800 °C), 고압 (> 20 bar) 및 높은 수증기/탄소 비 (수증기/탄소 > 2) 조건에서 수행된다. 하지만 이러한 반응 조건은 안전성 등의 문제 때문에 사용처 현지에서의 수소 생산에는 적합하지 않다. 이러한 이유로 온건한 반응 조건에서 높은 활성과

내구성을 보이는 효율적인 수증기 개질 촉매를 개발하는 것이 매우 중요하다고 볼 수 있다. 니켈-알루미나 촉매의 발달된 중형기공 구조는 활성 니켈의 분산도를 증진시킬 뿐만 아니라 촉매의 열/물질 전달을 촉진시켜 높은 촉매 활성을 유발한다. 즉, 중형기공성 니켈-알루미나 촉매는 수증기 개질 반응에서의 촉매 활성 및 안정성 향상 등의 측면에서 주목을 받았다.

본 연구에서는, LNG의 촉매적 수증기 개질에서 높은 수소 생산 효율을 얻기 위해 에폭사이드 기반 졸-겔법, 초임계 이산화탄소 건조법, 탄소 주형법, 인 첨가, 증발 유도 자가 조립법 및 니켈의 화학적 고정화 등 다양한 촉매 제조법에 의해 중형기공성 니켈-알루미나 촉매를 물리화학적으로 개선하였다.

먼저, 단일공정 에폭사이드 유도 졸-겔법 및 초임계 이산화탄소 건조에 의해 중형기공성 $Ni-Al_2O_3$ 에어로겔 촉매(NA-ES)를 제조하고, 단일공정 알콕사이드 기반 졸-겔법 및 초임계 이산화탄소 건조에 의해 중형기공성 $Ni-Al_2O_3$ 에어로겔 촉매(NA-AS) 또한 제조하였다. 두 촉매 내에 니켈 종이 니켈-알루미네이트 상을 형성하면서 고르게 분산되었다. 하지만 NA-ES 촉매가 NA-AS 촉매에 비해 높은 환원성과 높은 분산도를 보였다. LNG 수증기 개질 반응에서 NA-ES 촉매가 LNG 전환율 및 수소 수율 측면에서 NA-AS 촉매보다 더 우수한 촉매 활성을 보였다.

단일공정 탄소 주형 졸-겔법을 이용하여 탄소 주형 물질의 양(X)을 변화시켜 가면서 중형기공성 니켈-알루미나 제로겔 촉매(CNAX)군을 제조하였다. 탄소 주형 물질의 양이 증가함에 따라 CNAX 촉매의 조직 특성은 개선되었으며, 니켈과 알루미나의 상호 작용은 점차 약해지는 것으로 나타났다. 환원된 CNAX 촉매의

금속 니켈 결정 크기는 탄소 주형 물질의 양에 대해 화산형 추세를 보였다. LNG 수증기 개질 반응에서 CNAX (X = 0, 6, 12 및 18) 촉매들은 안정적인 활성을 보인데 반해, CNA24 촉매는 심한 비활성화 양상을 보였다. 그리고 촉매의 금속 니켈 결정 크기가 감소함에 따라 초기 LNG 전환율과 수소 수율은 증가하였다.

에폭사이드 유도 졸-겔법 및 초기 습윤 함침법에 의해 중형기공성 인-알루미나 제로젤에 담지된 니켈 촉매군(Ni/XPA, X = P/Al 몰 비)을 제조하였다. 소성된 Ni/XPA 촉매들은 산화니켈과 니켈-알루미네이트 상을 보였으나, 이 두 상의 상대적인 분포는 P/Al 몰 비에 따라 변화하였다. 환원된 Ni/XPA 촉매의 P/Al 몰 비가 증가함에 따라 금속 니켈 결정 크기는 증가하였다. 그러나 H_2-TPD 및 CH_4-TPD 실험에서 Ni/0.05PA 촉매가 가장 많은 양의 강한 수소 흡착점과 메탄 흡착량을 보이는 것으로 나타났다. LNG 수증기 개질 반응에서의 촉매 활성은 Ni/XPA 촉매의 P/Al 몰 비에 대해 화산형 추세를 나타내었으며, 이 결과는 CH_4-TPD 실험에서 얻어진 메탄 흡착량과 상관관계를 보였다.

단일공정 에폭사이드 유도 졸-겔법 및 초임계 이산화탄소 건조법에 의해 중형기공성 니켈-인-알루미나 에어로젤 촉매(NPAA)를 제조하였고, 비교를 위해 증발 건조법에 의해 중형기공성 니켈-인-알루미나 제로젤 촉매(NPAX) 또한 제조하였다. 초임계 이산화탄소 건조법은 NPAA 촉매의 조직 특성을 향상시키는데 효과적이었다. 또한, NPAA 촉매는 NPAX 촉매에 비해 높은 니켈 분산도와 메탄 흡착량을 보이는 것으로 나타났다. LNG 수증기 개질 반응에서는 메탄에 대한 친화도가 높은 NPAA 촉매가 NPAX 촉매보다 우수한 반응 활성을 보였다.

단일공정 증발 유도 자가조립법에 의해 정렬된 중형기공을 갖는 니켈-알루미나 촉매(OMNA)와 정렬된 중형기공을 갖는 알루미나 담체 상에 담지된 니켈 촉매(Ni/OMA)가 제조되었다. Ni/OMA 및 OMNA 촉매 모두 한 방향으로 정렬된 중형기공성 구조를 보였으나, 촉매의 조직 특성은 촉매 제조 방법에 따라 큰 차이를 보였다. Ni/OMA 촉매에 비해 OMNA 촉매의 니켈 종은 높은 환원성을 보일 뿐만 아니라 환원 과정에서 소결 현상에 대한 높은 저항성을 보이는 것으로 확인되었다. 촉매 반응 실험에서는, 작은 금속 니켈 결정 크기를 보인 OMNA 촉매가 Ni/OMA 촉매에 비해 높은 LNG 전환율과 수소 수율을 나타냈다. 또한, 양이온성/음이온성/비이온성 계면활성제를 이용한 일반 계면활성제 주형법에 의해 제조된 정렬되지 않은 중형기공성 니켈-알루미나 촉매에 비해 OMNA 촉매가 LNG 수증기 개질 반응에서 더 높은 활성을 보인다는 점도 확인되었다.

알루미나 담체 상의 니켈 분산도를 증가시키기 위해 니켈의 화학적 고정화가 시도되었다. 상용 함침법에서는 알루미나 담체 상에 니켈이 심하게 뭉치게 된다. 하지만, 양전하를 띠는 알루미나 표면과 $Ni(EDTA)^{2-}$ 복합 음이온의 쿨롱 상호작용을 통한 화학적 고정화에 의해 니켈은 알루미나 담체 상에 고르게 분산될 수 있다. 화학적 고정화 법에 의해 제조된 촉매(NiE/Al)는 상용 함침법에 의해 제조된 촉매(Ni/Al)에 비해 큰 니켈 분산도와 메탄 흡착량을 보였다. 이에 따라 NiE/Al 촉매는 LNG 수증기 개질 반응에서 Ni/Al 촉매보다 좋은 촉매 활성을 나타내었다.

요약하자면, 본 연구에서는 물리화학적으로 개선된 다양한 니켈-알루미나 촉매를 제조하고 이를 LNG 수증기 개질 반응을

통한 수소 생산 반응에 적용하였다. 준비된 촉매의 LNG 수증기 개질 반응에서의 활성도를 설명하기 위해 질소 흡탈착 분석, XRD, TPR, TEM, H_2-TPD 및 CH_4-TPD 등의 다양한 특성 분석 기법이 수행되었다. 결과적으로, 니켈의 분산도와 반응물에 대한 친화도가 LNG 수증기 개질 반응을 통한 수소 생산에서의 촉매 활성을 결정짓는 주요 인자라는 것이 밝혀졌다.

주요어: 수소 생산, 액화천연가스의 수증기 개질, 니켈 촉매, 에폭사이드 유도 졸-겔법, 탄소 주형, 인, 제로젤, 에어로젤, 증발 유도 자가조립, 화학적 고정화

학 번: 2010-20994

List of publications

Papers

International papers published (First author)

1. **Y. Bang**, S. Park, S.J. Han, J. Yoo, J.H. Choi, T.H. Kang, J. Lee, I.K, Song, "Hydrogen Production by Steam Reforming of Liquefied Natural Gas (LNG) over Nickel-phosphorus-alumina Xerogel Catalyst Prepared by a Carbon-templating Epoxide-driven Sol-gel Method", *Journal of Nanoscience and Nanotechnology* (In Press).

2. **Y. Bang**, S.J. Han, S. Kwon, V. Hiremath, I.K. Song, J.G. Seo, "High Temperature Carbon Dioxide Capture on Nano-structured MgO-Al_2O_3 and CaO-Al_2O_3 Adsorbents: An Experimental and Theoretical Study", *Journal of Nanoscience and Nanotechnology,* 14(11), pp.8531-8538 (2014).

3. **Y. Bang**, S.J. Han, J. Yoo, S. Park, J.H. Choi, Y.J. Lee, J.H. Song, I.K. Song, "Hydrogen Production by Steam Reforming of Liquefied Natural Gas (LNG) over Mesoporous Nickel-phosphorus-alumina Aerogel Catalyst", *International Journal of Hydrogen Energy*, 39(10), pp.4909-4916 (2014).

4. **Y. Bang**, S.J. Han, J. Yoo, J.H. Choi, J.K. Lee, J.H. Song, J. Lee, I.K. Song, "Hydrogen Production by Steam Reforming of Simulated Liquefied Natural Gas (LNG) over Nickel Catalyst Supported on Mesoporous Phosphorus-modified Alumina Xerogel", *Applied Catalysis B: Environmental*, 148-149, pp.269-280 (2014).

5. **Y. Bang**, S.J. Han, J. Yoo, J.H. Choi, K.H. Kang, J.H. Song, J.G. Seo, J.C. Jung, I.K. Song, "Hydrogen Production by Steam Reforming of Liquefied Natural Gas (LNG) over Trimethylbenzene-assisted Ordered Mesoporous

Nickel-alumina Catalyst", *International Journal of Hydrogen Energy*, 38(21), pp.8751-8758 (2013).

6. **Y. Bang**, S.J. Han, J.G. Seo, M.H. Youn, J.H. Song, I.K. Song, "Hydrogen Production by Steam Reforming of Liquefied Natural Gas (LNG) over Ordered Mesoporous Nickel-alumina Catalyst", *International Journal of Hydrogen Energy*, 37(22), pp.17967-17977 (2012).

7. **Y. Bang**, J. Lee, S.J. Han, J.G. Seo, M.H. Youn, J.H. Song, I.K. Song, "Hydrogen Production by Steam Reforming of Liquefied Natural Gas (LNG) over Mesoporous Nickel-alumina Xerogel Catalysts Prepared by a Single-step Carbon-templating Sol-gel Method", *International Journal of Hydrogen Energy*, 37(15), pp.11208-11217 (2012).

8. **Y. Bang**, J.G. Seo, M.H. Youn, I.K. Song, "Hydrogen Production by Steam Reforming of Liquefied Natural Gas (LNG) over Mesoporous Ni-Al_2O_3 Aerogel Catalyst Prepared by a Single-step Epoxide-driven Sol-gel Method", *International Journal of Hydrogen Energy*, 37(2), pp.1436-1443 (2012).

9. **Y. Bang**, J.G. Seo, I.K. Song, "Hydrogen Production by Steam Reforming of Liquefied Natural Gas (LNG) over Mesoporous Ni-La-Al_2O_3 Aerogel Catalysts: Effect of La Content", *International Journal of Hydrogen Energy*, 36(14), pp.8307-8315 (2011).

10. **Y. Bang**, D.R. Park, Y.J. Lee, J.C. Jung, I.K. Song, "Preparation, Characterization, and Oxidation Catalysis of $H_3PMo_{12}O_{40}$ Heteropolyacid Catalyst Immobilized on Carbon Aerogel", *Korean Journal of Chemical Engineering*, 28(1), pp.79-83 (2011).

International papers published (Co-author)

1. K.H. Kang, U.G. Hong, **Y. Bang**, J.H. Choi, J.K. Kim, J.K. Lee, S.J. Han, I.K. Song, "Hydrogenation of Succinic Acid to 1,4-Butanediol over Re-Ru Bimetallic Catalysts Supported on Mesoporous Carbon", *Applied Catalysis A: General*, 490, pp.153-162 (2015).

2. T.H. Kang, J.H. Choi, **Y. Bang**, J. Yoo, J.H. Song, W. Joe, J.S. Choi, I.K. Song, "Dehydration of Glycerin to Acrolein over $H_3PW_{12}O_{40}$ Heteropolyacid Catalyst Supported on Silica-alumina", *Journal of Molecular Catalysis A: Chemical*, 396, pp.282-289 (2015).

3. K.H. Kang, U.G. Hong, J.O. Jun, J.H. Song, **Y. Bang**, J.H. Choi, S.J. Han, I.K. Song, "Hydrogenation of Succinic Acid to γ-Butyrolactone and 1,4-Butanediol over Mesoporous Rhenium-copper-carbon Composite Catalyst", *Journal of Molecular Catalysis A: Chemical*, 395, pp.234-242 (2014).

4. J.H. Choi, T.H. Kang, **Y. Bang**, J.H. Song, I.K. Song, "Electrochemical and UV-visible Spectroscopy Studies of $K_6As_2W_{18-x}Mo_xO_{62}$ (x=0-3) Wells-Dawson Heteropolyacid Catalysts for Oxidative Dehydrogenation of Benzyl Alcohol", *Catalysis Communications*, 50, pp.29-33 (2014).

5. S.J. Han, **Y. Bang**, J. Yoo, S. Park, K.H. Kang, J.H. Choi, J.H. Song, I.K. Song, "Hydrogen Production by Steam Reforming of Ethanol over P123-assisted Mesoporous Ni-Al_2O_3-ZrO_2 Xerogel Catalysts", *International Journal of Hydrogen Energy*, 39(20), pp.10445-10453 (2014).

6. S.J. Han, **Y. Bang**, H.J. Kwon, H.C. Lee, V. Hiremath, I.K. Song, J.G. Seo, "Elevated Temperature CO_2 Capture on Nano-Structured MgO-Al_2O_3 Aerogel: Effect of Mg/Al Molar Ratio", *Chemical Engineering Journal*, 242, pp.357-363 (2014).

7. J.H. Choi, T.H. Kang, **Y. Bang**, J. Yoo, J.O. Jun, I.K. Song, "STM Investigation of Nano-structured α-$K_5PW_{11}O_{39}(M{\cdot}OH_2)$ (M = Mn^{II}, Co^{II}, Ni^{II}, and Zn^{II}) Heteropolyacid Catalyst Monolayers", *Journal of Nanoscience and Nanotechnology* (In Press).

8. Y.J. Lee, G.-P. Kim, **Y. Bang**, J. Yi, J.G. Seo, I.K. Song, "Activated Carbon Aerogel Containing Graphene as Electrode Material for Supercapacitor", *Materials Research Bulletin*, 50, pp.240-245 (2014).

9. J.H. Choi, T.H. Kang, J.H. Song, **Y. Bang**, I.K. Song, "Redox Behavior and Oxidation Catalysis of $H_nXW_{12}O_{40}$ (X=Co^{2+}, B^{3+}, Si^{4+}, and P^{5+}) Keggin Heteropolyacid Catalysts", *Catalysis Communications*, 43, pp.155-158 (2014).

10. S.J. Han, **Y. Bang**, J. Yoo, K.H. Kang, J.H. Song, J.G. Seo, I.K. Song, "Hydrogen Production by Steam Reforming of Ethanol over Mesoporous Ni-Al_2O_3-ZrO_2 Aerogel Catalysts", *International Journal of Hydrogen Energy*, 38(35), pp.15119-15127 (2013).

11. J. Yoo, **Y. Bang**, S.J. Han, T.H. Kang, J. Lee, I.K. Song, "Hydrogen Production by Steam Reforming of Liquefied Natural Gas (LNG) over Mesoporous Alkaline Earth Metal-promoted Nickel-alumina Xerogel Catalysts", *Journal of Molecular Catalysis A: Chemical*, 380, pp.28-33 (2013).

12. J.H. Choi, Y.J. Lee, T.H. Kang, **Y. Bang**, J.H. Song, J.C. Jung, I.K. Song, "Redox Properties of Transition Metal-substituted α_2-$K_8P_2W_{17}(M{\cdot}OH_2)O_{61}$ (M=Mn^{II}, Zn^{II}, Fe^{II}, Co^{II}, and Ni^{II}) Wells-Dawson Heteropolyacids Probed by Scanning Tunneling Microscopy and Tunneling Spectroscopy", *Catalysis Communications*, 39, pp.60-64 (2013).

13. S.J. Han, **Y. Bang**, J. Yoo, J.G. Seo, I.K. Song, "Hydrogen Production by Steam Reforming of Ethanol over Mesoporous Ni-Al_2O_3-ZrO_2 Xerogel Catalysts: Effect of Nickel Content", *International Journal of Hydrogen Energy*, 38(20), pp.8285-8292 (2013).

14. H.W. Park, J.K. Kim, U.G. Hong, Y.J. Lee, J.H. Choi, **Y. Bang**, I.K. Song, "Catalytic Decomposition of 1,3-Diphenoxybenzene to Monomeric Cyclic Compounds over Palladium Catalysts Supported on Acidic Activated Carbon Aerogels", *Applied Catalysis A: General*, 456, pp.59-66 (2013).

15. S.J. Han, **Y. Bang**, J.G. Seo, J. Yoo, I.K. Song, "Hydrogen Production by Steam Reforming of Ethanol over Mesoporous Ni-Al_2O_3-ZrO_2 Xerogel Catalysts: Effect of Zr/Al Molar Ratio", *International Journal of Hydrogen Energy*, 38(3), pp.1376-1383 (2013).

16. J.G. Seo, M.H. Youn, **Y. Bang**, I.K. Song, "Hydrogen Production by Steam Reforming of Simulated Liquefied Natural Gas (LNG) over Mesoporous Nickel-M-Alumina (M=Ni, Ce, La, Y, Cs, Fe, Co, and Mg) Aerogel Catalysts", *International Journal of Hydrogen Energy*, 36(5), pp.3505-3514 (2011).

17. J.G. Seo, M.H. Youn, **Y. Bang**, I.K. Song, "Effect of Ni/Al Atomic Ratio of Mesoporous Ni-Al_2O_3 Aerogel Catalysts on Their Catalytic Activity for Hydrogen Production by Steam Reforming of Liquefied Natural Gas (LNG)", *International Journal of Hydrogen Energy*, 35(22), pp.12174-12181 (2010).

18. M.H. Youn, J.G. Seo, H. Lee, **Y. Bang**, J.S. Chung, I.K. Song, "Hydrogen Production by Auto-thermal Reforming of Ethanol over Nickel Catalysts Supported on Metal Oxides: Effect of Support Acidity", *Applied Catalysis B: Environmental*, 98(1-2), pp.57-64 (2010).

19. D.R. Park, S. Park, **Y. Bang**, I.K. Song, "Redox Property and Oxidation Catalysis of Group 5 Metal (V, Nb, Ta)-containing Keggin and Wells-Dawson Heteropolyacid (HPA) Catalysts", *Applied Catalysis A: General*, 373(1-2), pp.201-207 (2010).

20. U.G. Hong, D.R. Park, S. Park, J.G. Seo, **Y. Bang**, S. Hwang, M.H. Youn, I.K. Song, "Preparation and Oxidation Catalysis of $H_5PMo_{10}V_2O_{40}$ Catalyst

Immobilized on Nitrogen-containing Spherical Carbon (N-SC)", *Catalysis Letters*, 132(3-4), pp.377-382 (2009).

Domestic papers published (First author)

1. **Y. Bang**, J.G. Seo, G. Lee, C.J. Park, H.T. Kim, I.K. Song, "Low-temperature Oxidation of Odor Compounds over La-based Perovskite Catalyst", *Korean Chemical Engineering Researches*, 49(2), pp.168-174 (2011).

Patents

Registered patents

1. 송인규, 한승주, **방용주**, 이현주, “중형기공성 니켈-알루미나-지르코니아 제어로젤 촉매 및 상기 촉매를 이용한 에탄올의 수증기 개질 반응에 의한 수소가스 제조 방법”, 대한민국 특허출원 10-2012-0097393, 대한민국특허 제1,392,996호 (2014).

2. 이현주, 송인규, 최준환, **방용주**, 한승주, “나노 탄소 입자를 주형 물질로 사용하여 제조된 중형기공성 니켈-알루미나 제어로젤 촉매, 그 제조 방법 및 상기 촉매를 이용한 액화천연가스(LNG)의 수증기 개질 반응에 의한 수소가스 제조 방법”, 대한민국 특허출원 10-2012-0003937, 대한민국특허 제 1,405,306호 (2014).

3. 이관영, 송인규, 서정길, **방용주**, “중형기공성 니켈-M-알루미나 에어로젤(Aerogel) 촉매 및 그의 제조방법”, 대한민국 특허출원 10-2010-0100718, 대한민국특허 제 1,269,621호 (2013).

4. 송인규, **방용주**, 서정길, 이기춘, 박찬정, 김형태, “란탄, 백금 및 전이금속 기반의 담지 페롭스카이트 촉매, 그 제조방법 및 상기 촉매를 이용하여 음식물 처리 과정에서 발생하는 악취 성분을 저온 산화 반응에 의해 제거하는 방법”, 대한민국 특허출원 10-2010-0086207, 대한민국특허 제 1,192,575호 (2012).

Applied patents

1. 송인규, 박승원, **방용주**, 한승주, 유재경, 이현주, “중형기공성 니켈-철-알루미나 제로젤 촉매, 그 제조 방법 및 상기 촉매를 이용한 액화천연가스의 수증기 개질 반응에 의한 수소 가스 제조 방법”, 대한민국 특허출원 10-2014-0157965 (2014).

2. 송인규, 강기혁, 홍웅기, **방용주**, “규칙적인 중형기공구조를 갖는 레늄-구리-탄소 복합체 촉매, 그 제조방법 및 상기 촉매를 이용한 1,4-부탄디올의 생산 방법”, 대한민국 특허출원 10-2014-0032557 (2014).

3. 송인규, **방용주**, 한승주, 유재경, 이현주, “중형기공성 니켈-인-알루미나 에어로젤 촉매, 그 제조 방법 및 상기 촉매를 이용한 액화천연가스의 수증기 개질 반응에 의한 수소 가스 제조 방법”, 대한민국 특허출원 10-2013-0117889 (2013).

4. 송인규, **방용주**, 한승주, 유재경, 이현주, “인을 포함한 중형기공성 알루미나 제어로젤 담체에 담지된 니켈 촉매, 그 제조 방법 및 상기 촉매를 이용한 액화천연가스의 수증기 개질 반응에 의한 수소가스 제조 방법”, 대한민국 특허출원 10-2013-0108834 (2013).

5. 송인규, 박동률, **방용주**, 최정호, 이윤재, “카본 에어로젤에 고정화된 헤테로폴리산 담지 촉매, 그 제조방법 및 상기 촉매를 이용한 이소프로판올의 산화반응에 의한 아세톤 제조방법”, 대한민국 특허출원 10-2010-0021178 (2010).

Conferences

International conferences (First author)

1. **Y. Bang**, S.J. Han, J. Yoo, J.H. Choi, J.K. Lee, I.K. Song, “Hydrogen Production by Steam Reforming of Liquefied Natural Gas (LNG) over Nickel Catalyst Supported on Mesoporous Phosphorus-modified Alumina Xerogel”, *20th WHEC(World Hydrogen Energy Conference) 2014*, 58, Kwangju, Korea (2014/6/15-20).

2. **Y. Bang**, S.J. Han, J. Yoo, S. Park, J.H. Choi, J. Lee, I.K. Song, “Hydrogen Production by Steam Reforming of LNG over Nickel-phosphorus-alumina Catalyst Prepared by a Templating Sol-gel Method”, *NANO KOREA 2014*, P1406_001, COEX, Seoul, Korea (2014/7/2-4).

3. **Y. Bang**, S.J. Han, J. Yoo, J.H. Choi, K.H. Kang, I.K. Song, “Preparation of Structure-modified Ordered Mesoporous Nickel-alumina Catalyst for Hydrogen Production by Steam Reforming of Liquefied Natural Gas (LNG)”, *International Conference on Hydrogen Production - 2014*, P-45, Fukuoka, Japan (2014/2/2-5).

4. **Y. Bang**, J. Lee, S.J. Han, J.G. Seo, I.K. Song, “Hydrogen Production by Steam Reforming of LNG over Mesoporous Nickel-alumina Xerogel Catalysts Prepared by a Carbon-templating Method”, *The 9th World Congress of Chemical Engineering (The 15th Asian Pacific Confederation Chemical Engineering Congress)*, MoP-T1-039, COEX, Korea (2013/8/18-23).

5. **Y. Bang**, S.J. Han, H.J. Kwon, S. Kwon, H.C. Lee, I.K. Song, J.G. Seo, “High Temperature Carbon Dioxide Capture on Nano-structured Alkaline-earth Metal Oxide Adsorbent”, *NANO Korea 2013 Symposium*, P1303_034, COEX, Seoul, Korea (2013/7/10-12).

6. **Y. Bang**, S.J. Han, J. Yoo, J.G. Seo, I.K. Song, “Hydrogen Production by Steam Reforming of Liquefied Natural Gas (LNG) over Mesoporous Nickel-alumina Catalysts”, *The 6th WCU International Symposium on Chemical Convergence for Energy and Environment*, Incheon, Korea (2013/6/17-18).

7. **Y. Bang**, S.J. Han, J.G. Seo, J. Yoo, I.K. Song, “Hydrogen Production by Steam Reforming of Liquefied Natural Gas (LNG) over Ordered Mesoporous Nickel-alumina Catalyst”, *The 4th International Conference on New & Renewable Energy 2013*, P2-9, Daegu, Korea (2013/3/28-30).

8. **Y. Bang**, J.G. Seo, M.H. Youn, S.J. Han, I.K. Song, “Hydrogen Production by Steam Reforming of Liquefied Natural Gas (LNG) over Mesoporous Ni-Al_2O_3 Aerogel Catalyst”, *The 15th International Congress on Catalysis*, 6607, Munich, Germany (2012/07/1-7).

9. **Y. Bang**, D.R. Park, Y.J. Lee, I.K. Song, "Preparation of $H_3PMo_{12}O_{40}$ Catalyst Immobilized on Carbon Aerogel and Its Application to Vapor-phase Cyclohexanol Dehydrogenation", *10th International Symposium on Nanocomposites and Nanoporous Materials*, P084, Duksan, Korea (2009/12/3-5).

International conferences (Co-author)

1. S.J. Han, **Y. Bang**, J. Yoo, I.K. Song, “Hydrogen Production by Steam Reforming of Ethanol over Mesoporous Ni-Al_2O_3-ZrO_2 Aerogel Catalyst”, *20th WHEC (World Hydrogen Energy Conference) 2014*, 56, Kwangju, Korea (2014/6/15-20).

2. J. Yoo, **Y. Bang**, S.J. Han, T.H. Kang, I.K. Song, “Hydrogen Production by Steam Reforming of Liquefied Natural Gas (LNG) over Mesoporous Alkaline

Earth Metal-promoted Nickel-alumina Xerogel Catalysts", *20th WHEC(World Hydrogen Energy Conference) 2014*, 52, Kwangju, Korea (2014/6/15-20).

3. S.J. Han, **Y. Bang**, V. Hiremath, I.K. Song, J.G. Seo, "Synthesis of Mesoporous MgO-Al_2O_3 Adsorbents for CO_2 Capture Using Block Copolymers and Ionic Liquids", *NANO KOREA 2014*, P1403_008, COEX, Seoul, Korea (2014/7/2-4).

4. J.H. Choi, T.H. Kang, **Y. Bang**, I.K. Song, "Scanning Tunneling Microscopy and Tunneling Spectroscopy Investigations of Nano-structured α_2-$K_6As_2W_{18-x}Mo_xO_{62}$ (x=0-3) Wells-Dawson Heteropolyacid Catalyst Monolayers", *NANO KOREA 2014*, P1404_002, COEX, Seoul, Korea (2014/7/2-4).

5. S.J. Han, **Y. Bang**, J. Yoo, K.H. Kang, J.H. Song, J.G. Seo, I.K. Song, "Ethanol Steam Reforming over a Mesoporous Ni-Al_2O_3-ZrO_2 Aerogel Catalyst", *7th Tokyo Conference on Advance Catalytic Science and Technology*, GP2035, Kyoto, Japan (2014/6/1-6).

6. S.J. Han, **Y. Bang**, J. Yoo, I.K. Song, "Ethanol Steam Reforming over a Mesoporous Ni-Al_2O_3-ZrO_2 Xerogel Catalysts", *International Conference on Hydrogen Production - 2014*, P-44, Fukuoka, Japan (2014/2/2-5).

7. J. Yoo, **Y. Bang**, S.J. Han, T.H. Kang, I.K. Song, "Effect of Promoter on Nickel-alumina Xerogel Catalyst for Hydrogen Production by Steam Reforming of Liquefied Natural Gas (LNG)", *International Conference on Hydrogen Production - 2014*, P-43, Fukuoka, Japan (2014/2/2-5).

8. S.J. Han, **Y. Bang**, H. Kang, I.K. Song, J.G. Seo, "CO_2 Physicochemical Adsorption on the Hierarchically Mesoporous MgO-Al_2O_3 Adsorbents with Bimodal Pore System", *NANO Korea 2013 Symposium*, P1303_035, COEX, Seoul, Korea (2013/7/10-12).

9. J.H. Choi, T.H. Kang, **Y. Bang**, J. Yoo, J.O. Jun, I.K. Song, "STM Investigation of Nano-structured α-$K_5PW_{11}O_{39}(M{\cdot}OH_2)$ (M = Mn^{II}, Co^{II}, Ni^{II}, and Zn^{II}) Heteropolyacid Catalyst Monolayers", *NANO Korea 2013 Symposium*, P1303_006, COEX, Seoul, Korea (2013/7/10-12).

10. S.J. Han, **Y. Bang**, J.G. Seo, J. Yoo, I.K. Song, "Hydrogen Production by Steam Reforming of Ethanol over Mesoporous Ni-Al_2O_3-ZrO_2 Xerogel Catalysts: Effect of Zr/Al Molar Ratio", *The 4th International Conference on New & Renewable Energy 2013*, P2-11, Daegu, Korea (2013/3/28-30).

Domestic conferences (First author)

1. **방용주**, 박승원, 한승주, 유재경, 최정호, 송인규, "킬레이트화된 니켈 전구체의 함침을 통한 니켈/알루미나 촉매의 제조 및 액화천연가스의 수증기 개질 반응으로의 적용", 2014 년 한국화학공학회 추계학술회의, P 촉매금-11, 대전 DCC (2014/10/22-24).

2. **방용주**, 한승주, 유재경, 박승원, 최정호, 송인규, "탄소 입자를 주형 물질로 하는 중형기공성 니켈-인-알루미나 촉매의 제조 및 액화천연가스의 수증기 개질 반응으로의 적용", 2014 년 한국공업화학회 춘계학술회의, 1P-256, 제주 ICC (2014/4/30-5/2).

3. **방용주**, 한승주, 유재경, 박승원, 최정호, 송인규, "인이 도입된 중형기공성 니켈-알루미나 촉매 상의 액화천연가스의 수증기 개질 반응", 2014 년 한국화학공학회 춘계학술회의, O 촉매목-10, 창원 컨벤션센터 (2014/4/23-25).

4. **방용주**, 한승주, 유재경, 최정호, 송인규, "인이 도입된 중형기공성 니켈-인-알루미나 에어로젤 촉매의 제조 및 액화천연가스의 수증기

개질 반응으로의 적용", 2013 년 한국공업화학회 추계학술회의, 2P-253, 대전 컨벤션센터 (2013/10/30-11/1).

5. **방용주**, 한승주, 유재경, 최정호, 송인규, "인이 도입된 중형기공성 니켈/알루미나 제어로젤 촉매 상의 액화천연가스의 수증기 개질 반응을 통한 수소 가스 생산", 2013 년 한국화학공학회 추계학술회의, P 촉매목-2, 대구 EXCO (2013/10/23-25).

6. **방용주**, 한승주, 유재경, 서정길, 송인규, "인이 도입된 중형기공성 Ni-P_2O_5-Al_2O_3 제어로젤 촉매의 제조 및 액화천연가스의 수증기 개질 반응으로의 적용", 2013 년 한국공업화학회 춘계학술회의, 1P-459, 제주 국제컨벤션센터 (2013/5/1-3).

7. **방용주**, 한승주, 유재경, 서정길, 송인규, "기공팽창제가 도입된 중형기공성 니켈-알루미나 촉매 상의 액화천연가스의 수증기 개질 반응을 통한 수소 가스 생산", 2013 년 한국화학공학회 춘계학술회의, O 촉매 I 목-23, 광주 김대중컨벤션센터 (2013/4/24-26).

8. **방용주**, 한승주, 유재경, 서정길, 윤민혜, 송인규, "기공팽창제의 도입을 통한 정렬된 중형기공을 갖는 니켈-알루미나 촉매의 제조 및 액화천연가스의 수증기 개질 반응으로의 적용", 2012 년 한국공업화학회 추계학술회의, 2P-179, 대전컨벤션센터 (2012/10/31-11/2).

9. **방용주**, 한승주, 유재경, 서정길, 윤민혜, 송인규, "정렬된 중형기공을 갖는 니켈-알루미나 촉매 상의 액화천연가스의 수증기 개질 반응을 통한 수소 가스 생산", 2012 년 한국화학공학회 추계학술회의, P 촉매수-15, 부산 BEXCO (2012/10/24-26).

10. **방용주**, 한승주, 서정길, 윤민혜, 송인규, “정렬된 기공 구조를 갖는 중형기공성 니켈-알루미나 촉매의 제조 및 액화천연가스의 수증기 개질 반응으로의 적용”, 2012 년 한국공업화학회 춘계학술회의, 2P-175, 김대중컨벤션센터 (2012/5/9-11).

11. **방용주**, 이중원, 한승주, 서정길, 윤민혜, 송인규, “탄소 입자를 주형 물질로 하여 제조된 중형기공성 니켈-알루미나 제어로젤 촉매 상의 액화천연가스의 수증기 개질 반응을 통한 수소 가스 생산”, 2012 년 한국화학공학회 춘계학술회의, P 촉매금-24, 제주 ICC (2012/4/25-27).

12. **방용주**, 서정길, 윤민혜, 송인규, “비알콕사이드 졸-겔 법을 기반으로 하는 니켈-알루미나 에어로젤 촉매의 제조 및 액화천연가스의 수증기 개질 반응으로의 적용”, 2011 년 한국공업화학회 추계학술회의, 1P-260, 경원대학교 (2011/11/2-4).

13. **방용주**, 서정길, 윤민혜, 송인규, “에폭사이드 기반 졸-겔 법에 의해 제조된 중형기공성 니켈-알루미나 에어로젤 촉매 상의 액화천연가스의 수증기 개질 반응 활성”, 2011 년 한국화학공학회 추계학술회의, P 촉매목-11, 송도컨벤시아 (2011/10/26-28).

14. **방용주**, 서정길, 송인규, “란탄이 첨가된 중형기공성 니켈-알루미나 에어로젤 촉매 상의 액화천연가스(LNG)의 수증기 개질 반응에서 니켈 및 란탄의 담지량 변화가 활성에 미치는 영향”, 2011 년 한국공업화학회 춘계학술회의, 2P-297, 제주국제컨벤션센터 (2011/5/11-13).

15. **방용주**, 서정길, 송인규, “니켈 및 란탄의 담지량이 다른 중형기공성 니켈-란탄-알루미나 에어로젤 촉매의 제조 및 액화천연가스(LNG)의

수증기 개질 반응으로의 적용", 2011 년 한국화학공학회 춘계학술회의, P 촉매목-7, 창원컨벤션센터 (2011/4/27-29).

16. **방용주**, 서정길, 송인규, "백금이 치환된 란탄 기반 페롭스카이트 담지 촉매의 제조 및 저온 산화 탈취 반응으로의 적용", 2010 년 한국공업화학회 추계학술회의, 2P-174, 대전컨벤션센터 (2010/10/27-29).

17. **방용주**, 서정길, 송인규, "악취 유발 물질의 저온 탈취 반응을 위한 $LaNi_{1-x}Pt_xO_3$ 형 페롭스카이트 촉매 연구", 2010 년 한국화학공학회 추계학술회의, P 촉매금-7, 대전컨벤션센터 (2010/10/20-22).

18. **방용주**, 송인규, "$LaBO_3$ 형 페롭스카이트 촉매를 이용한 악취 유발 물질의 산화 탈취 반응 연구", 2010 년 한국공업화학회 춘계학술회의, 2P-244, 부산 BEXCO (2010/5/13-14).

19. **방용주**, 송인규, "악취 유발 물질의 산화 탈취 반응을 위한 란탄 기반 페롭스카이트 촉매 연구", 2010 년 한국화학공학회 춘계학술회의, P 촉매목-7, 대구 EXCO (2010/4/21-23).

20. **방용주**, 박동률, 홍웅기, 송인규, "탄소 에어로젤의 표면 개질을 통한 헤테로폴리산 촉매의 화학적 고정화 및 기상 산화 반응으로의 적용", 2009 년 한국화학공학회 추계학술회의, P 촉매금-3, 일산 KINTEX (2009/10/21-23).

21. **방용주**, 박동률, 홍웅기, 송인규, "탄소 에어로젤 상의 헤테로폴리산의 화학적 고정화 및 기상 산화 반응에의 적용", 2009 년 한국공업화학회 추계학술회의, 1P-106, 서울산업대학교 (2009/10/15-16).

Domestic conferences (Co-author)

1. 최정호, 강태훈, **방용주**, 송인규, "몰리브덴이 선택적으로 치환된 Wells-Dawson 형 Tungstoarsenate 의 산화환원 특성에 관한 연구", 2014 년 한국화학공학회 추계학술회의, P 촉매금-1, 대전 DCC (2014/10/22-24).

2. 강기혁, 홍웅기, 전진오, **방용주**, 최정호, 한승주, 송인규, "레늄-구리-카본 복합체 촉매 상에서 숙신산의 수소화를 통한 감마부티로락톤과 1,4-부탄디올의 제조", 2014 년 한국화학공학회 추계학술회의, P 촉매금-2, 대전 DCC (2014/10/22-24).

3. 한승주, **방용주**, 유재경, 박승원, 송인규, "P123 과 이온성 액체가 주형물질로 도입된 중형기공성 니켈-알루미나 촉매 제조 및 에탄올 수증기 개질 반응으로의 적용", 2014 년 한국화학공학회 추계학술회의, P 촉매금-4, 대전 DCC (2014/10/22-24).

4. 유재경, **방용주**, 한승주, 박승원, 송인규, "세리아를 담체로 이용한 니켈 촉매 상에서의 메탄의 삼중 개질 반응", 2014 년 한국화학공학회 추계학술회의, P 촉매금-6, 대전 DCC (2014/10/22-24).

5. 박승원, **방용주**, 한승주, 유재경, 송인규, "중형기공성 니켈-철-알루미나 제로젤 촉매 상의 액화천연가스 수증기 개질반응을 통한 수소가스 생산", 2014 년 한국화학공학회 추계학술회의, P 촉매금-8, 대전 DCC (2014/10/22-24).

6. 한승주, **방용주**, 유재경, 서정길, 송인규, "P123 이 도입된 졸겔법을 통한 니켈-알루미나-지르코니아 제로젤 촉매 제조 및 에탄올 수증기

개질 반응으로의 적용", 2014 년 한국공업화학회 춘계학술회의, 1P-254, 제주 ICC (2014/4/30-5/2).

7. 최정호, 강태훈, **방용주**, 송인규, "서로 다른 중심원소를 가지는 Keggin 형 헤테로폴리산의 산화환원 특성에 관한 연구", 2014 년 한국공업화학회 춘계학술회의, 1P-259, 제주 ICC (2014/4/30-5/2).

8. 박승원, **방용주**, 한승주, 유재경, 송인규, "에폭사이드 기반 졸-겔법을 통해 제조된 니켈-철-알루미나 제로젤 촉매의 액화천연가스 수증기 개질 반응으로의 적용", 2014 년 한국공업화학회 춘계학술회의, 1P-262, 제주 ICC (2014/4/30-5/2).

9. 유재경, **방용주**, 한승주, 송인규, "세리아가 포함된 중형기공성 니켈 촉매 상에서 메탄의 삼중 개질 반응을 통한 수소 가스 생산", 2014 년 한국공업화학회 춘계학술회의, 1P-265, 제주 ICC (2014/4/30-5/2).

10. 최정호, 강태훈, **방용주**, 송인규, "Keggin 형 α-$H_nXW_{12}O_{40}$($X=Co^{2+}$, B^{3+}, Si^{4+}, and P^{5+}) 헤테로폴리산 촉매의 산화환원 및 반응활성에 관한 연구", 2014 년 한국화학공학회 춘계학술회의, P 촉매금-3, 창원 컨벤션센터 (2014/4/23-25).

11. 한승주, **방용주**, 유재경, 서정길, 송인규, "P123 이 도입된 중형기공성 니켈-알루미나-지르코니아 제로젤 촉매 상에서 에탄올 수증기 개질 반응을 통한 수소 가스 생산", 2014 년 한국화학공학회 춘계학술회의, P 촉매금-67, 창원 컨벤션센터 (2014/4/23-25).

12. 박승원, **방용주**, 한승주, 유재경, 송인규, "중형기공성 니켈-철-알루미나 제로젤 촉매 상의 액화천연가스의 수증기 개질 반응을

통한 수소 가스 생산", 2014 년 한국화학공학회 춘계학술회의, P 촉매금-68, 창원 컨벤션센터 (2014/4/23-25).

13. 유재경, **방용주**, 한승주, 송인규, "세리아의 도입이 니켈계 촉매 상에서의 메탄의 삼중 개질 반응에 미치는 영향", 2014 년 한국화학공학회 춘계학술회의, P 촉매금-69, 창원 컨벤션센터 (2014/4/23-25).

14. 한승주, **방용주**, 유재경, 서정길, 송인규, "에탄올 수증기 개질 반응에서 니켈-알루미나-지르코니아 촉매에 도입된 계면활성제가 반응 활성에 미치는 영향", 2013 년 한국공업화학회 추계학술회의, 2P-174, 대전 컨벤션센터 (2013/10/30-11/1).

15. 이윤재, 송인규, **방용주**, 이종협, 윤중락, "K_2CO_3 를 사용하여 활성화된 슈퍼커패시터 전극용 활성 카본 에어로젤-그래핀 화합물의 전기화학적 특성", 2013 년 한국공업화학회 추계학술회의, 2P-175, 대전 컨벤션센터 (2013/10/30-11/1).

16. 유재경, **방용주**, 한승주, 송인규, "중형기공성 니켈-알루미나 촉매 상의 액화천연가스의 수증기 개질 반응에 마그네슘 조촉매의 도입이 미치는 영향", 2013 년 한국공업화학회 추계학술회의, 2P-179, 대전 컨벤션센터 (2013/10/30-11/1).

17. 최정호, 강태훈, **방용주**, 강기혁, 송인규, "4 주기 전이금속이 배위된 Keggin 형 헤테로폴리산 촉매의 산화환원 특성에 관한 연구", 2013 년 한국공업화학회 추계학술회의, 2P-181, 대전 컨벤션센터 (2013/10/30-11/1).

18. 한승주, **방용주**, 유재경, 서정길, 송인규. "계면활성제가 도입된 중형기공성 니켈-알루미나-지르코니아 제로젤 촉매 상에서 에탄올

수증기 개질 반응을 통한 수소 가스 생산", 2013 년 한국화학공학회 추계학술회의, P 촉매목-3, 대구 EXCO (2013/10/23-25).

19. 유재경, **방용주**, 한승주, 송인규, "마그네슘을 조촉매로 첨가한 중형기공성 니켈-알루미나 촉매의 제조 및 액화천연가스(LNG)의 수증기 개질 반응으로의 적용", 2013 년 한국화학공학회 추계학술회의, P 촉매목-9, 대구 EXCO (2013/10/23-25).

20. 최정호, 강태훈, **방용주**, 강기혁, 송인규, "Keggin 형 α-$K_5PW_{11}O_{39}(M{\cdot}OH_2)$ ($M=Mn^{2+}$, Co^{2+}, Ni^{2+}, Zn^{2+}) 헤테로폴리산 촉매의 산화환원 및 반응활성에 관한 연구", 2013 년 한국화학공학회 추계학술회의, P 촉매목-10, 대구 EXCO (2013/10/23-25).

21. 한승주, **방용주**, 유재경, 서정길, 송인규, "초임계 건조를 통해 제조한 니켈-알루미나-지르코니아 에어로젤 촉매의 에탄올 수증기 개질 반응으로의 적용", 2013 년 한국공업화학회 춘계학술회의, 1P-401, 제주 국제컨벤션센터 (2013/5/1-3).

22. 유재경, **방용주**, 한승주, 서정길, 송인규, "중형기공성 M/니켈-알루미나(M=Mg, Ca, Sr 및 Ba) 촉매 상의 액화천연가스의 수증기 개질 반응을 통한 수소 가스 생산", 2013 년 한국공업화학회 춘계학술회의, 1P-398, 제주 국제컨벤션센터 (2013/5/1-3).

23. 한승주, **방용주**, 유재경, 서정길, 송인규, "중형기공성 니켈-알루미나-지르코니아 에어로젤 촉매 상에서 에탄올 수증기 개질 반응을 통한 수소 가스 생산", 2013 년 한국화학공학회 춘계학술회의, P 촉매금-6, 광주 김대중컨벤션센터 (2013/4/24-26).

24. 유재경, **방용주**, 한승주, 서정길, 송인규, “알칼리 토금속을 첨가한 중형기공성 니켈-알루미나 촉매의 제조 및 액화천연가스(LNG)의 수증기 개질 반응으로의 적용”, 2013 년 한국화학공학회 춘계학술회의, P 촉매금-10, 광주 김대중컨벤션센터 (2013/4/24-26).

25. 한승주, **방용주**, 유재경, 서정길, 윤민혜, 송인규, “에탄올 수증기 개질반응에서 중형기공성 니켈-알루미나-지르코니아 촉매의 니켈 담지량이 반응 활성에 미치는 영향”, 2012 년 한국공업화학회 추계학술회의, 2P-176, 대전컨벤션센터 (2012/10/31-11/2).

26. 한승주, **방용주**, 유재경, 서정길, 윤민혜, 송인규, “단일공정 에폭사이드 기반 졸-겔법을 통해 제조된 니켈-알루미나-지르코니아 제어로젤 촉매를 이용한 에탄올 수증기 개질반응에 대한 연구”, 2012 년 한국화학공학회 추계학술회의, P 촉매수-12, 부산 BEXCO (2012/10/24-26).

27. 한승주, **방용주**, 서정길, 윤민혜, 송인규, “에폭사이드 기반 졸-겔 법을 통한 중형기공성 알루미나-지르코니아에 담지된 니켈 촉매의 제조 및 에탄올 수증기 개질 반응으로의 적용”, 2012 년 한국공업화학회 춘계학술회의, 2P-203, 김대중컨벤션센터 (2012/5/9-11).

28. 한승주, **방용주**, 서정길, 윤민혜, 송인규, “중형기공성 알루미나-지르코니아 복합 제어로젤 담체에 담지 니켈 촉매 상의 에탄올 수증기 개질 반응을 통한 수소 가스 생산”, 2012 년 한국화학공학회 춘계학술회의, P 촉매금-33, 제주 ICC (2012/4/25-27).

29. 서정길, 윤민혜, **방용주**, 송인규, “중형기공성 니켈-M-알루미나(M=Ni, Co, La, Ce, Y, Cu, Fe 및 Mg) 에어로젤 촉매의 제조 및 이를 활용한 액화천연가스(LNG)의 수증기 개질반응을 통한 수소 가스 생산”,

2010 년 한국공업화학회 추계학술회의, 2P-172, 대전컨벤션센터 (2010/10/27-29).

30. 서정길, 윤민혜, **방용주**, 송인규, “다양한 Ni/Al 원자비를 갖는 중형기공성 니켈-알루미나 에어로젤 상에서의 액화천연가스(LNG)의 수증기 개질반응에 의한 수소 생산에 관한 연구”, 2010 년 한국화학공학회 추계학술회의, P 촉매금-5, 대전컨벤션센터 (2010/10/20-22).

31. 박동률, 홍웅기, **방용주**, 송선호, 송인규, “배위원소가 치환된 Keggin 및 Wells-Dawson 형 헤테로폴리산(HPA)의 촉매특성 및 반응활성”, 2009 년 한국화학공학회 추계학술회의, O 촉매 E 금-5, 일산 KINTEX (2009/10/21-23).

32. 박동률, 홍웅기, **방용주**, 송선호, 송인규, “5 족 금속을 포함하는 $H_4PW_{11}M_1O_{40}$ (M=V, Nb, Ta) Keggin 형 헤테로폴리산(HPA) 촉매의 산화환원특성 및 산화반응활성에 대한 연구”, 2009 년 한국화학공학회 추계학술회의, P 촉매금-1, 일산 KINTEX (2009/10/21-23).

33. 박동률, 홍웅기, **방용주**, 송선호, 송인규, “5 족금속이 배위된 Wells-Dawson 형 헤테로폴리산(HPA) 촉매의 산화환원력 및 반응활성”, 2009 년 한국공업화학회 추계학술회의, 1P-104, 서울산업대학교 (2009/10/15-16).